5-2018

Design, Fabrication, and Characterization of All-Inorganic Quantum Dot Light Emitting Diodes

Ramesh Vasan
University of Arkansas, Fayetteville

Follow this and additional works at: http://scholarworks.uark.edu/etd

Part of the Electronic Devices and Semiconductor Manufacturing Commons, Nanoscience and Nanotechnology Commons, and the Semiconductor and Optical Materials Commons

Design, Fabrication, and Characterization of All-Inorganic Quantum Dot Light Emitting Diodes

A dissertation submitted in partial fulfillment
of the requirements for the degree of
Doctor of Philosophy in Engineering

by

Ramesh Vasan
Anna University, India
Bachelor of Engineering in Electronics and Instrumentation, 2010
University of Arkansas
Master of Science in Electrical Engineering, 2013

May 2018
University of Arkansas

This dissertation is approved for recommendation to the Graduate Council

_____

Omar Manasreh, Ph.D.
Dissertation Director

_____   _____

Simon Ang, Ph.D.   Jingxian Wu, Ph.D.
Committee Member   Committee Member

_____

Surendra Singh, Ph.D.
Committee Member

ABSTRACT

Quantum dot light emitting diodes are investigated as a replacement to the existing organic light emitting diodes that are commonly used for thin film lighting and display applications. In this, all-inorganic quantum dot light emitting diodes with inorganic quantum dot emissive layer and inorganic charge transport layers are designed, fabricated, and characterized. Inorganic materials are more environmentally stable and can handle higher current densities than organic materials. The device consists of CdSe/ZnS alloyed core/shell quantum dots as the emissive layer and metal oxide charge transport layer. The charge transport in these devices is found to occur through resonant energy transfer and direct charge injection.

Nickel oxide thin film is engineered with defect states within the bandgap by changing the stoichiometry of film. These defect states take part in the charge transport via resonant energy transfer mechanism. The energy transfer mechanism is modeled by measuring the lifetime of quantum dots in the presence of nickel oxide thin film. Energy transfer between nickel oxide defect states and quantum dots occurs at time scales as low as 0.26 ns. This mechanism is exploited to fabricate high efficiency light emitting diodes. Efficient green, yellow, and red emitting devices are fabricated and characterized. The peak external quantum efficiencies of 11.4%, 1.6% and 6.04% are obtained for green, yellow, and red emitting devices, respectively. The performance of green LED is much better than that of the other two colors as the photoluminescence quantum yield of green quantum dots are much higher than the other two quantum dot samples.

Nickel oxide is also synthesized as nanoparticles for potential application in hole transport. Charge transport in devices with nickel oxide nanoparticles occurs via direct charge injection mechanism. The nanoparticles are near-stoichiometric with very low defect densities.

The quantum dots exhibit shorter average lifetimes when mixed with nickel oxide nanoparticle powder indicating a favorable band alignment for direct charge injection. Quantum dot LED is fabricated with nickel oxide nanoparticle hole transport layer and red emitting quantum dots. The light output characteristics are evaluated and a peak external quantum efficiency of 2.36% is obtained.

ACKNOWLEDGEMENTS

TABLE OF CONTENTS

LIST OF FIGURES

LIST OF TABLES

1. INTRODUCTION

Throughout human history artificial lighting technologies were used and developed. Artificial electric lighting developed rapidly over the last century and currently consumes around 20% of the total energy consumption [1]. So, energy efficient lighting technologies are needed to reduce the global energy consumption and in turn the impact on the environment. According to Energy Independence and Security Act of 2007 by 2020 all artificial lighting must have a minimum luminous efficacy of 45 lm/W [2]. Luminous efficacy is defined as the ratio of output light in lumens per input electric power. Earliest forms of electric lighting in the form of incandescent or general lighting service (GLS) lamps were developed in late 19th century. These lamps had a luminous efficacy of 1.4 lm/W. The basic working of an incandescent lamp is that current is passed through a tungsten filament encased in an evacuated tube filled with an inert gas like Ar or N. These lamps have a very short lifetime of ~1000 hrs, low luminous efficacy of 15 – 20 lm/W, and very low conversion efficiency [1]. The low efficiency of these lamps is attributed to the heat loss. A variant of incandescent lamps is the halogen where the inert gas is replaced with a halogen. The next generation of electric lamps were fluorescent lamps. It consists of a discharge tube filled with mercury gas and the inner part of the tube is coated with a phosphor. The arc excites the mercury gas and produces UV light. The UV light strikes the phosphor, which in-turn emits visible light. These lamps are cheap, efficient, and easy to install when compared to the incandescent lamps. A better variant of fluorescent lamps are the compact fluorescent lamps and as the name suggests, it is a compact variant of a regular fluorescent lamp. They are much expensive than regular fluorescent lamps and exhibits good luminous efficacy. Other types of electric lighting include mercury vapor lamps, low and high pressure sodium vapor lamps, induction lamp and metal halide lamps. Application of these lamps is based on

1

their working, efficiency and color quality. The properties of different lamp types are listed in the table 1.1 [1].

Table 1.1. Properties of different types of lighting technologies that are used for general purpose lighting [1].

Lamp Type	Characteristics				
	Luminous Efficacy	Lifetime	Cost of Installation	Cost of Operation	Applications
GLS	5-15	1000	Low	Very high	General lighting
Halogen	12-35	2000-4000	Low	High	General lighting
Fluorescent	50-100	10000-16000	Low	Low	General lighting
Compact fluorescent	40-65	6000-12000	Low	Low	General lighting
Sodium vapor	80-100	12000-16000	High	Low	Outdoor lighting
Mercury vapor	40-60	12000	Moderate	Moderate	Outdoor lighting
Metal halide	50-100	6000-12000	High	Low	Commercial building
Induction	60-80	60000-100000	High	Low	Inaccessible locations for maintenance

1.1. Solid-State Lighting

Most recent lighting technology that has entered general purpose lighting market is the solid-state lighting (SSL). Solid state lighting refers to the use of semiconductors or polymers as opposed to the gas, plasma or some form of heating element.   The most basic type of SSL is the semiconductor based light emitting diodes (LED). First LED was developed by Nick Holonyak Jr. at GE in 1962 [3]. Ever since its first development, the technology has undergone extensive

research for past three decades and has entered commercial lighting market recently. LEDs are one of the most efficient and long-lasting lighting technologies. The LED operation temperature are very low compared to other lighting devices. This allows maximum energy conversion from electric input into light output and hence has high efficiency. Compared to other lighting technologies like incandescent or fluorescent lamps, color rendering index of LEDs is low. Moreover, the operating power is low and lifetime ranges between 25,000-60,000 hours [1]. Initially, red and yellow emitting LEDs were developed and in mid 90s first blue, bright green, and white emitting LEDs were developed [2].

An LED consists of a p-n junction diode, which is placed on a reflective cavity and encased inside an epoxy lens. Anode and cathode leads are brought out of the casing for electrical connections. Figure 1.1 shows the schematic of a LED. The reflective cavity reflects most of the light emitted from the p-n junction diode and the epoxy lens focuses the emitted light outward from the top of the LED as shown in figure 1.1
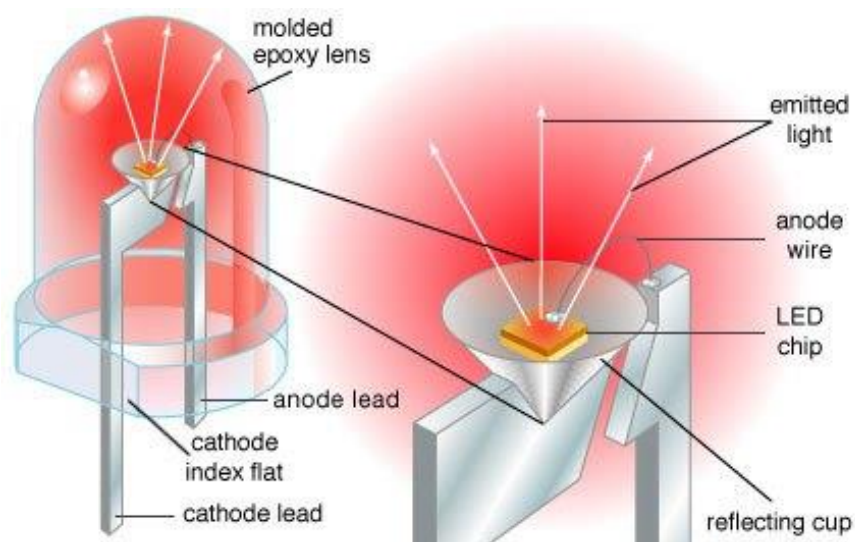
Figure 1.1. Schematic of a solid-state LED chip that is packaged inside a plastic casing. [4]

The emissive part of the device is a p-n junction diode. A p-n junction diode is a semiconductor device that is formed by combining a p-type semiconductor and n-type semiconductor forming a junction. Semiconductor consists of current carriers namely negatively charged electrons and positively charged holes. The electrical properties of the semiconductor directly depend on the free carrier concentration usually expressed per cm^3. In an intrinsic semiconductor the concentration of free electrons is equal to the concentration of holes and is called the intrinsic carrier concentration. For a given semiconductor intrinsic concentration is a constant at room temperature. Intrinsic carrier concentration of Si, GaAs and Ge are ~10^{10}, ~10^6 and ~10^{13} [5].

For a semiconductor, the valence band [6] and conduction band [6] are separated by a band gap or forbidden energy gap. The electrons in the valence band are bound and occupy the lowest energy levels at 0K. Even at higher energies these electrons cannot move within the valence band as the energy levels are occupied. Instead, these electrons jump into the lowest levels of conduction band leaving a hole behind when the energy is higher than the band gap energy. Since the higher levels of the conduction band have kinetic energy, the electrons in the conduction are free to move. In short, electrons in the valence band can be excited into conduction band with sufficient energy in form of light, heat, and electric field. The free electrons in the conduction band and holes in the valence band contribute to the current flow in a semiconductor device. A p-type semiconductor has excess holes while an n-type semiconductor has excess electrons when compared to the intrinsic carrier concentration of the semiconductor. In order to form p-type semiconductor, intrinsic semiconductors are doped with impurity atoms. The concentration of acceptor dopant atoms (Na) is usually equal to the free hole concentration. For example, if Si is doped with B, Al or Ga as impurities excess holes are generated turning it

4

into a p-type material [5]. In order to form n-type semiconductor, intrinsic semiconductors are doped with impurity atoms, which are called donor atoms. The concentration of donor dopant atoms (Nd) is usually equal to the free electron concentration. Like p-type, if Si is doped with P, As or N as impurities excess electrons are generated turning it into an n-type material [5]. The number of dopant atoms introduced per cm^3 of the host material determines the doping concentration. Fermi level (E_f) [7] in an intrinsic semiconductor lies exactly at the middle of the band gap. For n-type semiconductor free electrons in the conduction band is much higher than the intrinsic carrier concentration and consequently the fermi level is closer to the conduction band minimum (E_c). Similarly, in a p-type semiconductor the fermi level is closer to the valence band maximum (E_v). The position of E_f in a material is critical in determining the electrical properties of the material. Equations 1.1 and 1.2 are used to calculate the position of E_f in an n-type and p-type semiconductor, respectively.

$$E_F = E_C - K_B T \log \frac{N_C}{N_D} \tag{1.1}$$

$$E_F = E_V + K_B T \log \frac{N_A}{N_V} \tag{1.2}$$

where, E_F is the fermi level, E_C is the conduction band, E_V is the valence band, K_B is the Boltzmann constant, T is the absolute temperature, N_C is the effective density of states in the conduction band, N_D is the concentration of donor atoms, N_V is the effective density of states in the valence band, N_A is the concentration of acceptor atoms.

The band diagram of a p-type and n-type semiconductors are shown in figure 1.2 (a) and (b). When a junction is formed with these materials, the E_f is continuous as shown in figure 1.2 (c). An energy band diagram with aligned E_f corresponds to the p-n junction in equilibrium or

under zero bias. As soon as the junction is formed majority start to diffuse across the junction and start to recombine leaving a region on either side of the junction called depletion region. This region consists of uncompensated and immobile donor and acceptor ions. These uncompensated, separated charges in the junction create an internally built-in electric field, which in turn results in built-in voltage (V_b) across the junction. This can be seen in figure 1.2(c) as the difference between the E_c or E_v positions of the energy band diagram, which is in the form of energy barrier (qV_b). The region outside the depletion region is called the charge neutral region. A simple p-n junction is called a p-n junction diode.
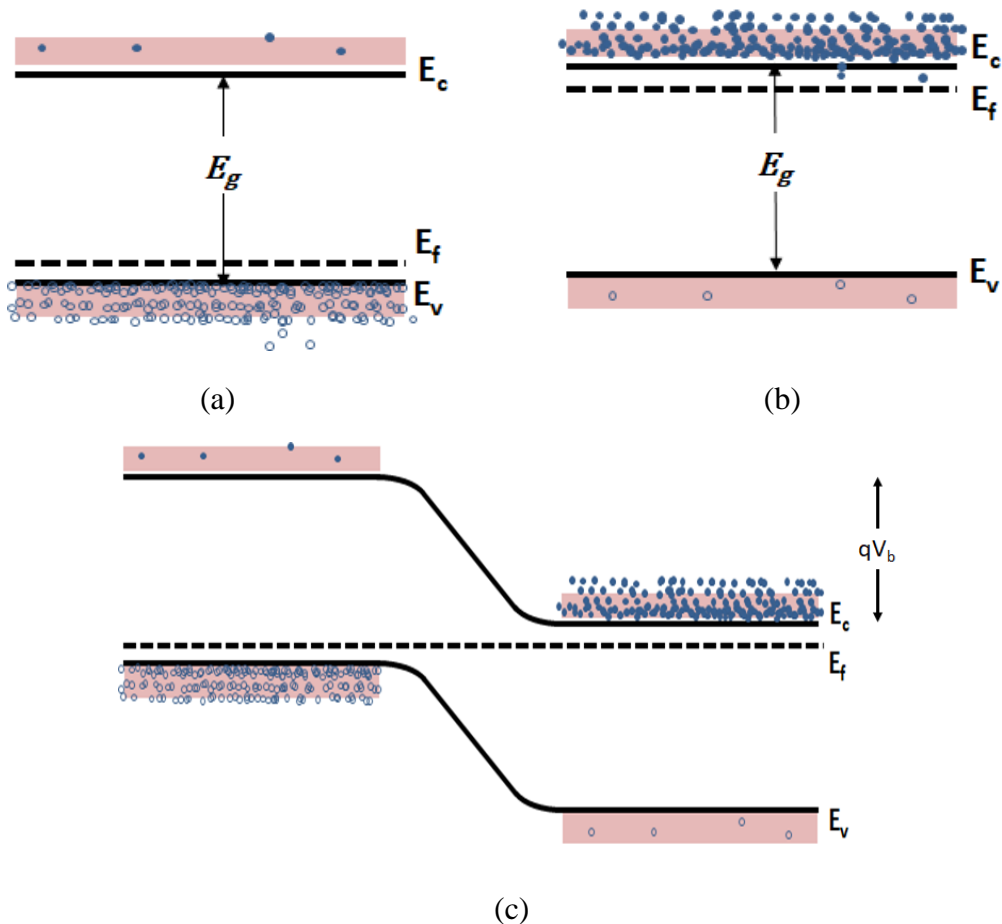
Figure 1.2. The band diagram schematics of (a) p-type, (b) n-type and (c) p-n junction are shown with the E_F

6

In the case of a LED, p-n junction diode is forward biased, and charges are injected towards the junction. The current conduction is minimum initially as there are energy barriers for holes and electrons as seen in figure 1.2(c). With further increase in forward voltage, the barrier gradually reduces, and carriers are injected across the junctions. At the same time the equilibrium position of E_f is split into quasi fermi levels E_{fp} and E_{fn}. During this process electron-hole pairs are formed that recombine and emit the photon. This is shown in figure 1.3. The energy of the emitted photon depends on the band gap of the semiconductor and is approximately equal to the band gap energy value. The voltage at which the LED turns ON is called the turn-on voltage. This voltage is usually a little over to the V_b of the p-n junction. In case of Si p-n junction V_b is ~0.7 V and this can vary depending on the semiconductor material. Usually, LEDs in the visible region are made with compound semiconductors and have higher V_b than Si p-n junction. Table 1.2 shows the commonly used semiconductors for different visible light emission.
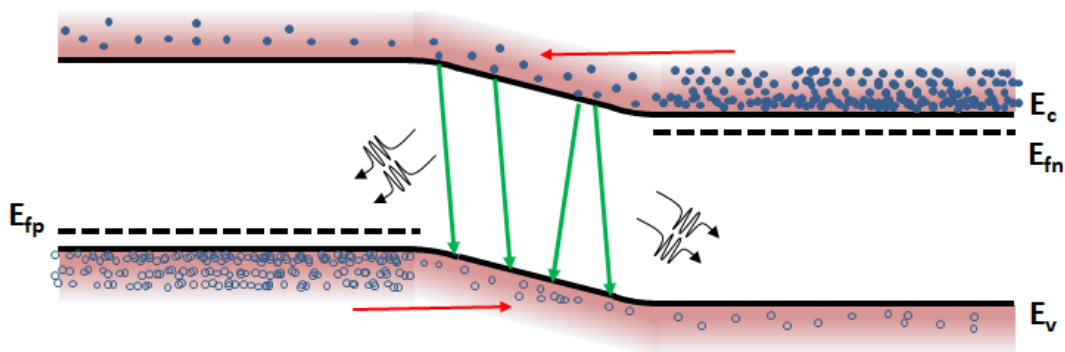
Figure 1.3. The band bending of the p-n junction energy band under forward bias voltage is depicted with quasi fermi levels. The process of charge injection across the junction and recombination are shown.

Table 1.2. Commercially available LED colors and corresponding semiconductors used to produce these colors are listed [8-15].

COLOR	AVAILABLE LED MATERIAL
	Gallium arsenide (GaAs), or Aluminium gallium arsenide (AlGaAs)
	Aluminium gallium arsenide (AlGaAs) Gallium arsenide phosphide (GaAsP), Aluminium gallium indium phosphide (AlGaInP), or Gallium(III) phosphide (GaP)
	Gallium arsenide phosphide (GaAsP), Aluminium gallium indium phosphide (AlGaInP), or Gallium(III) phosphide (GaP)
	Gallium arsenide phosphide (GaAsP), Aluminium gallium indium phosphide (AlGaInP), or Gallium(III) phosphide(GaP)
	Indium gallium nitride (InGaN) / Gallium(III) nitride (GaN), Gallium(III) phosphide (GaP), Aluminium gallium indium phosphide(AlGaInP) or Aluminium gallium phosphide (AlGaP)
	Zinc selenide (ZnSe), Indium gallium nitride (InGaN), Silicon carbide (SiC) as substrate, or Silicon (Si) as substrate
	Indium gallium nitride (InGaN), Dual blue/red LEDs, blue with red phosphor or white with purple plastic
	Diamond (235 nm), Boron nitride (215 nm), Aluminium nitride (AlN) (210 nm), Aluminium gallium nitride (AlGaN), or Aluminium gallium indium nitride (AlGaInN) – (down to 210 nm)
	Blue/UV LED diode with different colored phosphors.

For general lighting applications lamps that emit natural white light is needed. Humans perceive white light when all visible wavelengths are combined. Of the visible wavelengths pure red, green, and blue wavelengths are combined to form the natural white light. Most accurate white light is rendered by the sunlight and is used as a standard for comparing artificial lights.

The relative intensities of these wavelengths must be balanced to by some form of technology to obtain natural white light. Any imbalance would form a warmer white light, more towards the red end or cooler white light, more towards the blue end of the visible spectrum. Several modifications are made to existing LED chips that emit single color to form white light. Discrete red, green and blue LED chips are encapsulated in a single package and made to emit trichromatic white light. Dichromatic white light is produced by using blue and yellow emitting chips. Phosphors are also used to produce white light by acting as color convertors or filters. A blue or UV LED is used as the emissive part and red, green, yellow and orange phosphors are encapsulated with it [16]. These phosphors of different colors absorb the high energy blue or UV light and re-emit lower energy light. This is perceived as the white light. Some of the schematics of the existing LED white lighting technologies are shown in figure 1.4. Several advancements were made in LED technology by incorporating nanostructures. As shown in the figure 1.5, compared to incandescent and fluorescent lamps, white LEDs renders white light more effectively. The spectrum of commercial white LED is closer to the sun's spectrum in the visible region.

(a)

9
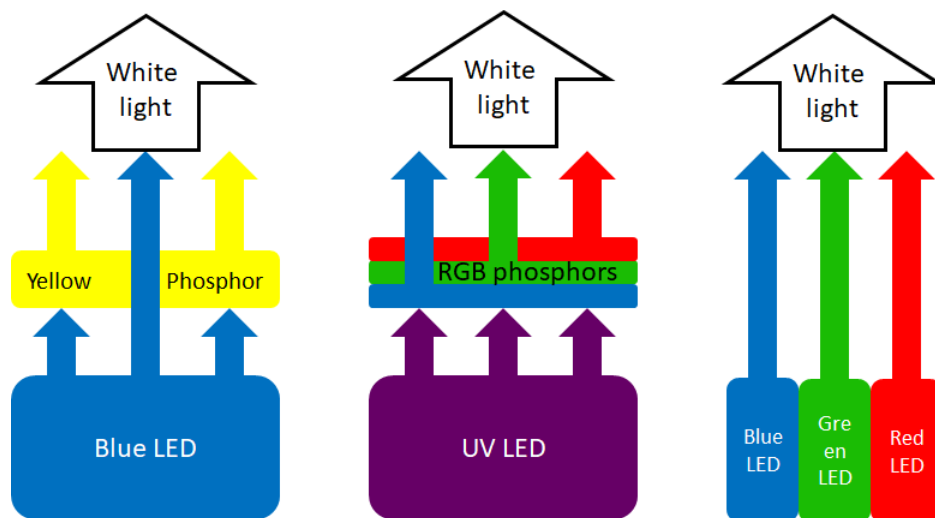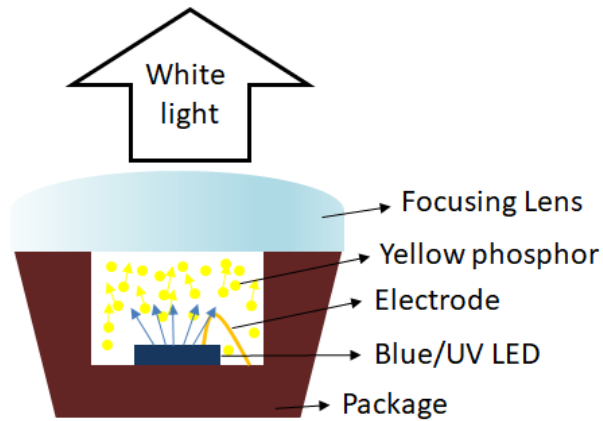
(b)

Figure 1.4. (a) White light is generated using blue/UV LED and RGB phosphors or combining the emission discrete red, green, and blue LEDs in the same package. (b) Cutaway schematic of phosphor based white LED with yellow phosphor and blue LED.
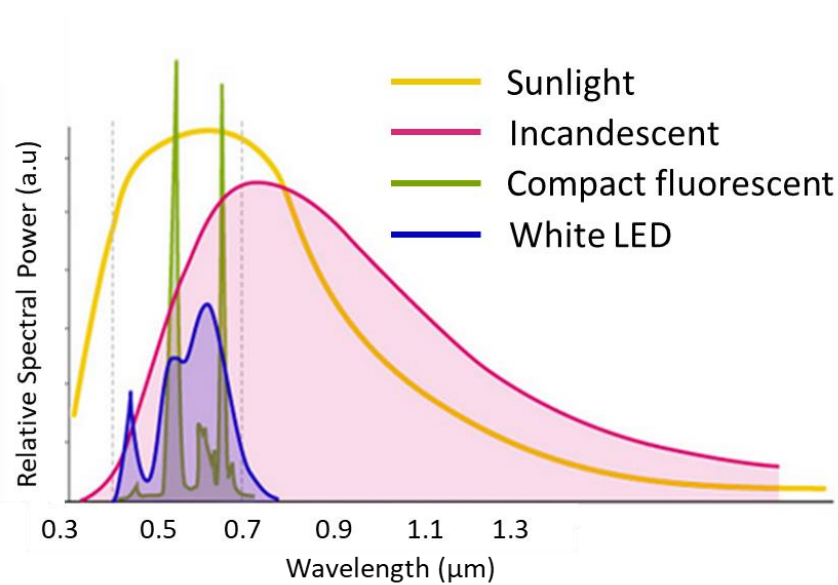
Figure 1.5. The white light quality of LEDs is compared to sunlight, incandescent and compact fluorescent lamps [17].

1.1.1 LED parameters

The device characterized by power conversion efficiency, external quantum efficiency and luminous efficacy. Luminous efficacy of these devices is high around 150 lm/W and it depends on the type of semiconductor and device architecture [18]. The power conversion

efficiency is the ratio of radiant power output to input electric power. The overall conversion efficiency depends on mechanisms that control carrier injection, carrier recombination, and LED package. These mechanisms can be combined into an efficiency parameter called external quantum efficiency given by equation 1.3 [18].

$$\eta_{ext} = \eta_{inj}\eta_{int}\eta_{out} \tag{1.3}$$

where, η_{ext} is the external quantum efficiency, η_{inj} is the carrier injection efficiency, η_{int} is the internal quantum efficiency, and η_{out} is the out-coupling efficiency. Some of the best red emitting AlInGaP and blue emitting InGaN LEDs can have radiative or internal quantum efficiencies of 100% and 50%, respectively [19]. In order to achieve such high external quantum efficiencies, light extraction from the package must be improved.

1.2. Thin film LED technologies

1.2.1. Organic LED

This film lighting devices for general lighting and display applications were initially developed using organic small molecules and polymers [20]. These are called as organic light emitting diodes (OLED). The technology is so advanced these days that most displays for devices like televisions, smart phones and other smart devices consist of OLEDs as basic lighting elements [21]. Some of the major advantages of OLEDs over regular LEDs are that the manufacturing process is simpler, can be made flexible and large area, and wide variety of organic emissive materials are available to cover the entire visible spectrum. An OLED consists of thin films of organic small molecules or polymers that are fabricated in a layer-by-layer architecture. The device is formed sandwiching a layer of organic emissive material between the

11

anode and cathode. Additionally, charge transport layers (CTL) are introduced between the

emissive layer and electrodes for efficient charge transport [20]. The substrate is glass or other

flexible materials that are coated with transparent conductive oxide (CTO) like indium thin oxide

(ITO) or fluorine tin oxide (FTO). The CTO acts as the anode. Organic small molecule or

polymer based hole transport layer (HTL) is grown on top of the anode. The HTL is followed by

the emissive layer, the electron transport layer (ETL) and the reflective metal cathode. The

schematic of an OLED is shown in figure 1.6. The layers are either spin coated from a solution

or thermally evaporated from a solid source using vacuum deposition [22].
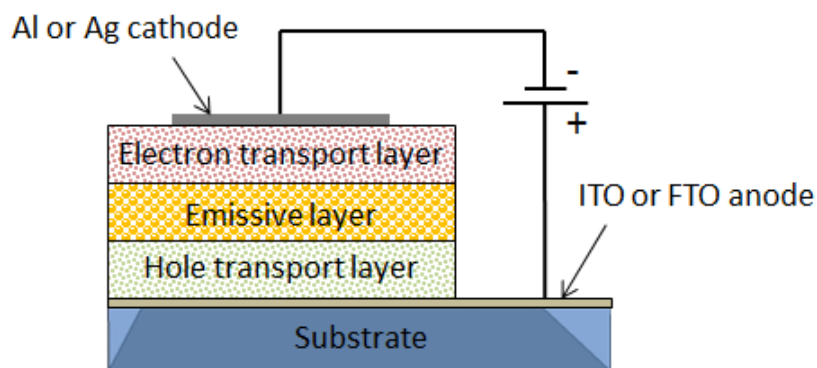
Figure 1.6. The schematic of OLED device that is fabricated on glass substrate by layer-by-layer
deposition.

The emissive material is a π-conjugated organic insulator and carriers must be injected

into it from the electrodes [23]. The injected carriers recombine in the emissive layer and emit

the photon. Unlike semiconductors, the organic layers do not have valence and conduction

bands. They have molecular orbitals and the energy of the emitted photon is approximately

equal to energy separation between highest occupied molecular orbital (HOMO) and lowest

unoccupied molecular orbital (LUMO). These molecular orbitals are analogous to valence and

conduction bands in an inorganic semiconductor. Usually, the barrier to injection of carriers

from the electrodes into the LUMO and HOMO of the emissive layer is high and so injection

efficiency is very low. This is overcome by introducing the CTLs, which act as steps for carrier injection into the emissive layer [20]. For a given emissive layer the ETL is chosen to have its LUMO level aligned with that of the LUMO of the emissive layer. For efficient hole transport the HOMO level of the HTL must align with the HOMO of the emissive layer. The barrier to electron and hole injection must be approximately equal to achieve a balanced charge injection [24]. If one of the barriers is lower than the other, then an imbalance occurs that leads to reduction in efficiency [24]. Several organic and inorganic CTLs were investigated to optimize the performance of OLEDs. Other than the LUMO and HOMO alignment, carrier mobility, environmental stability, compatibility with the emissive layer, and ease of processing were considered while choosing the CTLs. Progress in luminous efficacy of different white light technologies is shown in figure 1.7 [25].
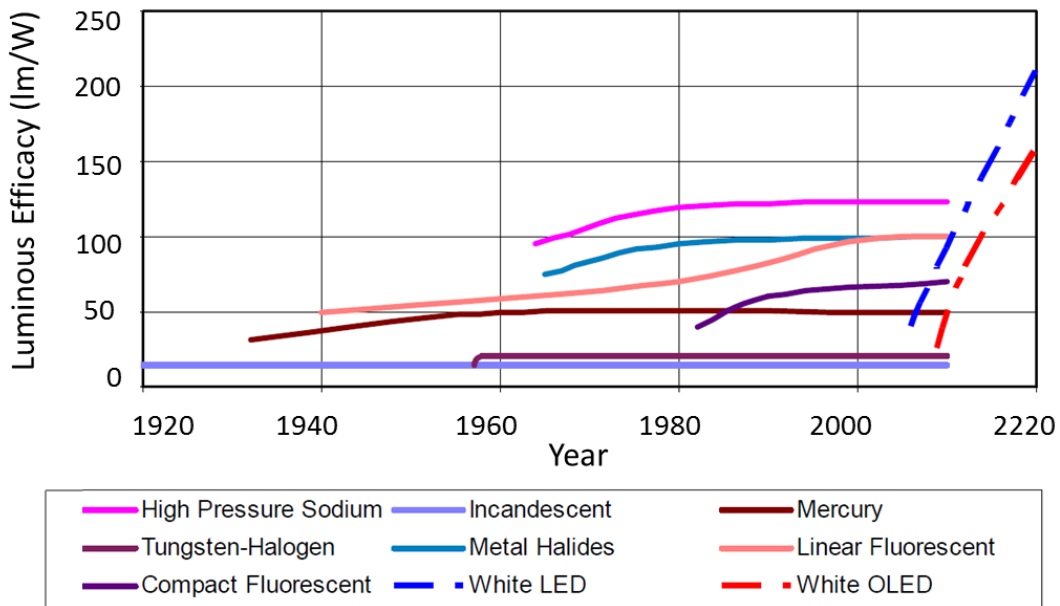
Figure 1.7. Progress in white light technologies with prediction that white OLED reaching a maximum luminous efficacy of 150 lm/W by 2020 [25].

1.2.2. Quantum dot LED

Colloidal quantum dot light emitting diodes (QLED) were recently investigated as a replacement for the existing OLEDs. The advantages of QLED include high color purity, size tunable and saturated emission, environmentally stable and low power operation over OLED [26, 27]. In the case of QLED, the organic emissive layer is replaced with inorganic quantum dots commonly Cd, Se, S and Zn based quantum dots. Quantum dots used for LED devices are nanostructures of II-VI chalcogenide semiconductors. The size of these quantum dots is between 2-20 nm in diameter [28]. These quantum dots have unique properties when compared to the bulk properties of the same material due to high surface to volume ratio of these quantum dots. The band gap of the quantum dots increases with decrease in the size. In the case of CdSe, the bulk material band gap is ~1.7 eV and increases when it is made into a nanostructure. A quantum dot provides 3D confinement of excitons as opposed to a bulk material where the excitons are not confined. An exciton is a bound electron-hole pair and the size of the exciton is called the exciton Bohr radius [29]. When the exciton Bohr radius is comparable to the size of the material the confinement is very low. The confinement is strong when the size of the quantum dot is much smaller than the exciton Bohr radius. In this strong confinement regime, the energy levels are not continuous instead are quantized. These quantized energy levels relate quantum dots more closely to atoms than bulk materials. This is a very important property of quantum dots that make them suitable for use in QLED as efficient emissive materials. The confinement increases the radiative lifetime of excitons in quantum dots, which increases the probability of radiative recombination. Additionally, since the emission wavelength of the QLED is approximately equal to band gap of the quantum dots, it can be controlled by

14

controlling the size of the quantum dots. In other words, same material with different sizes can by synthesized to emit different wavelengths in the visible spectrum.

Like OLEDs, carriers are injected into the quantum dots from the cathode and anode through the CTLs. Based on the type of transport materials used, QLEDs are classified into organic, hybrid organic/inorganic and inorganic. These architectures are schematically represented in the figure 1.8. Organic QLEDs consists of organic polymers or small molecules

| (a) | (b) | (c) |
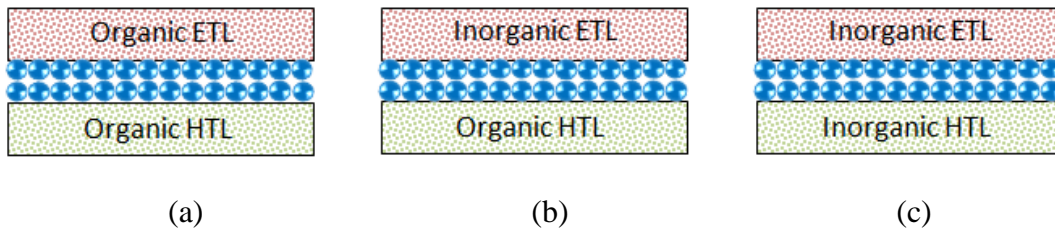
Figure 1.8. Schematics of (a) organic (b) hybrid and (c) all-inorganic QLED showing the transport layer and emissive layer are shown

as the CTLs with inorganic quantum dot emissive layer. Some of the commonly used organic HTLs are poly(3,4-ethylenedioxythiophene) polystyrene sulfonate (PEDOT:PSS), Poly[N,N'-bis(4-butylphenyl)-N,N'-bisphenylbenzidine] (poly-TPD), poly(N-vinylcarbazole) (PVK), Tris(4-carbazoyl-9-ylphenyl)amine (TCTA) and N,N′-Di(1-naphthyl)-N,N′-diphenyl-(1,1′-biphenyl)-4,4′-diamine (α-NPD), 4,4′-Bis(N-carbazolyl)-1,1′-biphenyl (CBP) [22,23]. Of these the polymers are mostly solution processable, while the small molecules are both solution processable and can be deposited thermally. Commonly used organic ETLs are 2, 2′,2"-(1,3,5-Benzinetriyl)-tris(1-phenyl-1-H-benzimidazole) (TPBi), and Tris-(8-hydroxyquinoline)aluminum (Alq$_3$) [22]. These devices were reported to be operating under direct charge injection, resonant energy transfer or both [24]. These proposed models are schematically illustrated in figure 1.9.
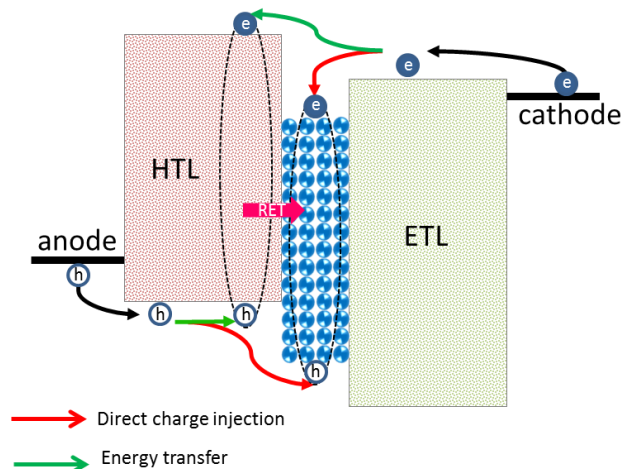
Figure 1.9. Charge transport in QLED is explained using a schematic. The red arrows depict direct charge injection and green arrows depict the energy transfer mechanism.

In the direct charge injection model, holes are injected into the valence band of the quantum dot through the HTL and electrons are injected into the conduction band through the ETL. In this model the transport layers facilitate the injection of carriers by reducing the barrier to carrier injection, in other words they act as steps to the carriers injected from the electrodes. In the energy transfer model, excitons are created in the charge transport layers that transfer the energy non-radiatively to the adjacent quantum dots forming excitons in the quantum dots. First form of organic QLEDs consisted of CdSe cores-polymer bilayer composites sandwiched between metal electrodes [30, 31]. These devices exhibited very low external quantum efficiency of <0.5% with a luminance of 600 cd/m^2 [32]. With further research, it was established that a closed pack monolayer of quantum dot film is required, which will decouple the emission process from the charge transport process through organic CTLs [33]. Quantum dot dispersions were mixed with polymer transport layer solution and spun together to form a self-assembled monolayer of quantum dots on the transport layer. This process is called phase separation, which enhanced the quantum efficiency of organic QLEDs [27, 33]. Micro contact printing technology was employed to fabricate organic QLED with external quantum efficiency >2.5% [34].

16

The hybrid QLEDs are the most widely studied and reported, which consists of quantum dot emissive layer, organic HTL and inorganic ETL. The inorganic ETLs are mostly n-type metal oxide semiconductors like zinc oxide, titanium dioxide, and tin oxide [35]. The efficiency of the hybrid devices is reported to be as high as 20% [36-38]. Like organic QLEDs, hybrid devices are reported to work under both direct charge injection and resonant energy transfer mechanisms [39]. Qian *et al.* demonstrated all solution processed hybrid RGB QLEDs with external quantum efficiencies reaching 0.22%, 1.8% and 1.7% for blue, green and orange-red, respectively [40]. The quantum efficiencies were further enhanced by using an inverted structure with a maximum luminance reaching 218,000 cd/m^2 for the green QLED [41]. Over 20% efficient hybrid QLEDs were reported recently [36-38].

In inorganic QLED, all the materials used are inorganic except for the organic ligands that surround the quantum dots. Commonly used inorganic HTLs are nickel oxide, tungsten trioxide, vanadium pentoxide, and graphene oxide [26, 42-52]. These inorganic devices are environmentally more stable and can support higher current densities than similar hybrid devices with CdSe quantum dots, but these devices are not well developed and quantum efficiency of the devices are ~1% [42-51]. In general, the external quantum efficiency of QLED is given by equation 1.4 [53]:

$$EQE = \eta_t \eta_{oc} \eta_{PL} \chi \tag{1.4}$$

where, η_{PL} is the quantum yield of the CdSe quantum dots, η_t is the charge transport efficiency of the device, η_{oc} is the light out-coupling efficiency and χ is the fraction of excitons that have allowed transitions in the quantum dot. The CdSe quantum dots are well developed and studied so the χ of these quantum dots are reported to be ~1 [53, 54]. Similarly, the quantum yield of

CdSe, specifically alloyed CdSeZnS system is as high as 70% [55-57]. Out-coupling efficiency,η_{oc}, is dependent on the device packaging and independent on the device operation. So, in a QLED device with alloyed CdSe/ZnS quantum dots, the external quantum efficiency is limited by the charge transport efficiency. In order to improve the efficiency of inorganic QLEDs, it is necessary to understand the charge transport mechanism and improve the charge transport efficiency. Most of the reports suggest the that charge transport occurs through direct charge injection mechanism, while some other report suggest that efficiency of the device is independent of the charge transport [39, 58, 59]. More specifically, hole (valence band) states in the quantum dots are between 1.5 – 2 eV higher than they are in the HTL, [42-53] leading to the accumulation of holes at the interface without the holes ever reaching the quantum dot valence band. This results in the charging of the quantum dots due to excess electrons reaching the quantum dot from the cathode, which ultimately reduces the quantum efficiency of the device due to non-radiative Auger recombination. On the other hand, it is reported that in a QLED device working with energy transfer mechanism Auger recombination can be suppressed significantly [39, 53, 60, 61]. For energy transfer to occur, the donor and the acceptor states need to be in resonance. Commonly used inorganic CTLs have bandgaps greater than 3.0 eV, well above the band gap of quantum dots emitting in the visible region, so any form of resonant energy transfer from the valence and conduction band of these CTLs is ruled out. In other words, there is no spectral overlap between the CTLs' band edge emission and the quantum dot absorption. So, new materials, material structures or modifications to existing inorganic HTLs are required to fabricate an efficient all-inorganic QLED. The progress in the different QLED architectures is shown in figure 1.10.

18
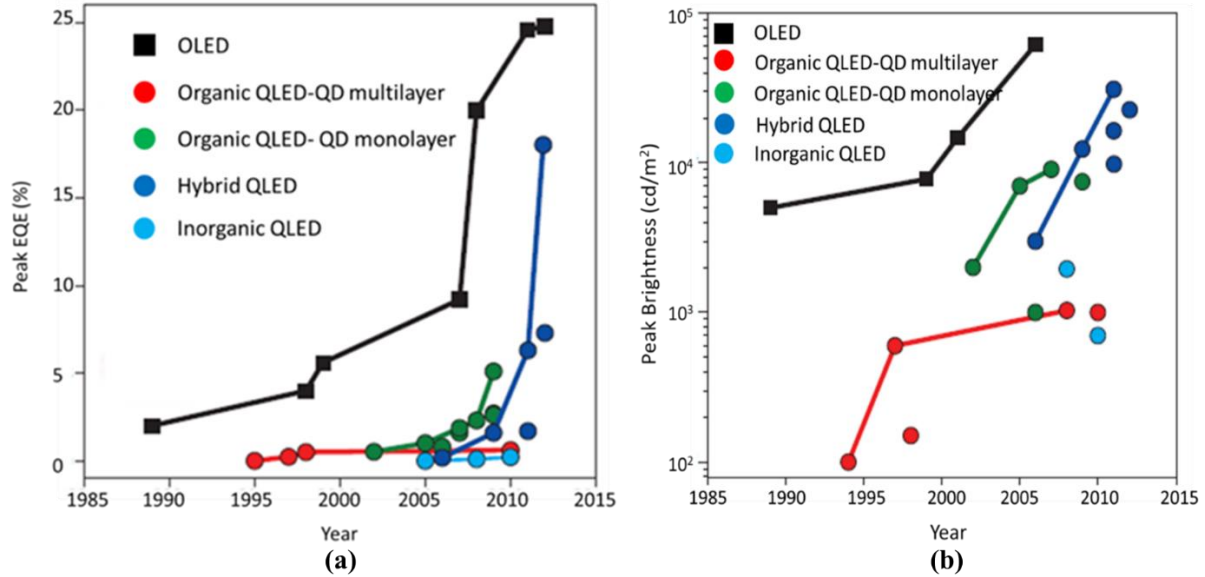
Figure 1.10. Progress in the performance of QLED architectures over a period of 30 years that are commonly reported in literature.

1.3. Research Objectives

The goal of this project is to understand the charge transport mechanism, improve the charge transport efficiency and ultimately increase the quantum efficiency of all-inorganic quantum dot light emitting devices. The most important efficiency limiting factor is the non-availability of inorganic HTL that can either support direct charge injection or energy transfer mechanism. Nickel oxide can be made in the form of thin film and nanoparticles that can support energy transfer and direct charge injection, respectively. For energy transfer to occur, the donor (HTL) and the acceptor (quantum dots) states must be in resonance. Commonly used HTLs have bandgaps greater than 3.0 eV, well above the band gap of quantum dots emitting in the visible region. Any form of resonant energy transfer from these HTLs is ruled out due to the non-availability adjacent resonant states in the quantum dots. So, if resonant states are located within the band gap of the HTLs formed due to defects, energy transfer is possible. It is well established that nickel oxide is p-type owing to defects in the lattice and that the properties of the

19

thin film can be tuned by varying the growth conditions and post-growth treatments [62-65].

More specifically, the stoichiometry of the film can be controlled by growing nickel oxide in an

oxygen controlled environment [66]. Higher % oxygen leads to the formation non-

stoichiometric nickel oxide with Ni vacancies. This makes nickel oxide an ideal HTL to

investigate the energy transfer mechanism over other HTLs namely V_2O_5, WO_3, and MoO_3.

Similarly, nickel oxide nanoparticles can be synthesized that can inject hole more efficiently. By

preparing nickel oxide in the form of nanoparticles, the bandgap and the stoichiometry can be

controlled. This directly affects the position of the valence band and thus enabling direct charge

injection into the quantum dots. This project investigates these two forms of nickel oxide to

improve the efficiency of all-inorganic QLED.

2. EXPERIMENTAL PROCEDURES

In this chapter, all material synthesis procedures and characterization tools used in this project are discussed. In section 1 material synthesis, sample fabrication and device fabrication procedures are discussed. Under this section, the syntheses of alloyed CdSe/ZnS core /shell quantum dot, nickel oxide HTL and ZnO nanoparticle ETL are discussed. The bilayer sample, nickel oxide thin film Schottky diode, ZnO thin film transistor and QLED devices fabrication are discussed in the second part of section 1. In section 2 the material and device characterization techniques/tools are discussed.

2.1. Material Synthesis, sample and device fabrication

2.1.1. CdSe/ZnS core shell alloyed quantum dots

The nanocrystals used as the emissive layer in the QLED are CdSe/ZnS alloyed core/shell nanocrystals. The main advantage of using alloyed core/shell over conventional core/shell structure is the reduced lattice mismatch between the core and shell [28, 57, 67]. Also, this structure enables the single step synthesis of the nanocrystals. The synthesis utilizes the chemical reactivity difference between the cations and anions. The Cd and Se are more reactive than the Zn and S, which enables the formation of CdSe core first. Once the Cd and Se precursors are used up in the reactor, the Zn and S starts forming the shell. There is no defined interface between the core and shell, but the interface is an alloy of CdSeZnS. This is schematically shown in the figure 2.1(a) and (b). The alloyed core/shell nanocrystals are synthesized by modifying the procedure reported by Bae, *et al.* [57, 67]. The synthesis apparatus, shown in figure 2.1(c) consists of a three-neck flask connected to a Schlenk line through a condenser tube. The Schlenk line is used to connect the reactor to N_2 and vacuum

during the reaction. The condenser tube is used to reflux the solvent into the reactor as the

reaction is carried out at over 300 °C. The reactor temperature is controlled by a closed loop

temperature controller setup using a thermocouple sensor and a heating mantle. The heating

mantle is placed on a magnetic spinner to stir the reaction mixture using a magnetic stirrer bar.

The whole setup is placed under a fume hood to remove any volatile and toxic fumes. The main

N_2 line of the fume hood and a 20 mTorr vacuum pump are connected to the Schlenk line.

(a)

(b)

(c)
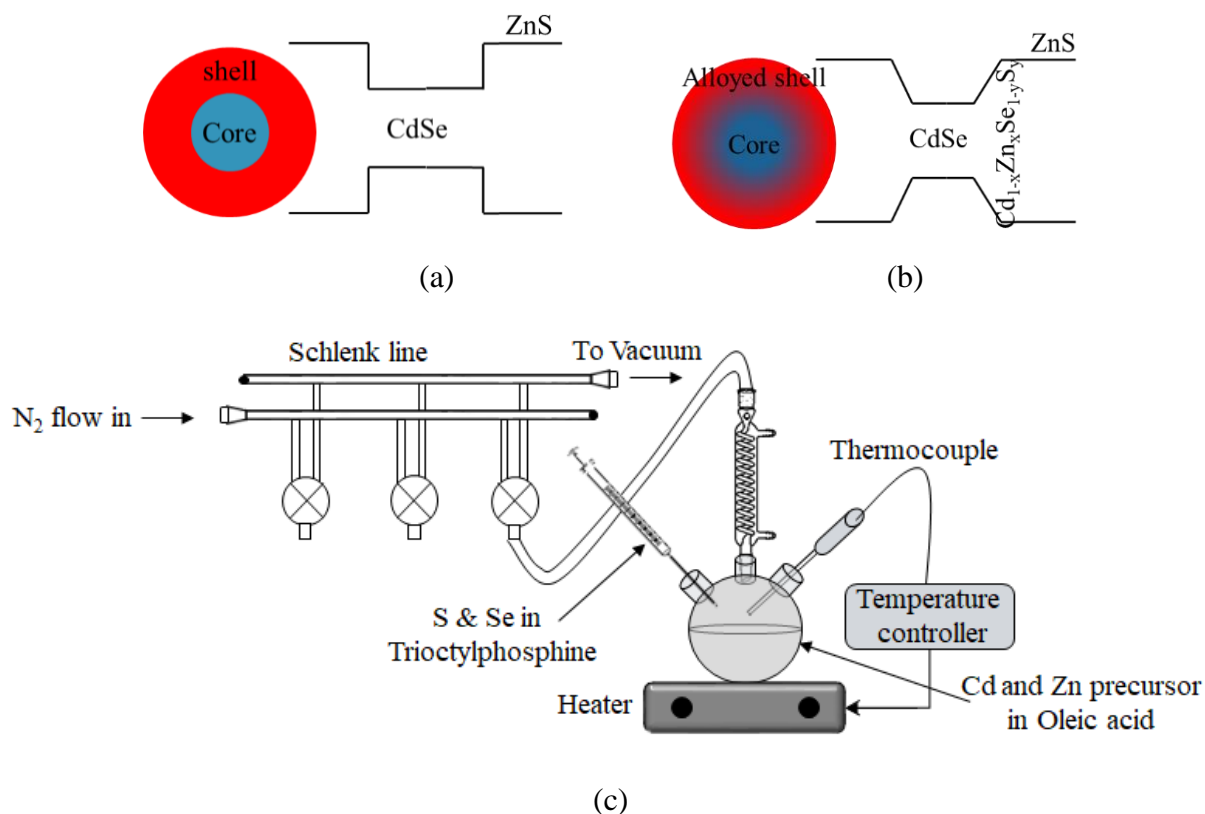
Figure 2.1. Schematics of a (a) conventional core/shell quantum dot and (b) alloyed core/shell quantum dot are depicting the core/shell interface. (c) The core/shell quantum dots are synthesized using a Schlenk line and three neck flask setups.

To synthesize quantum dots of different sizes two different synthesis approaches were

investigated. In the first approach the precursor concentrations, reaction temperature, time are

kept constant and the ligand concentration is modified. The ligands play the role of controlling

the size of the quantum dot and after synthesis ligands prevent the aggregation of the quantum

dots [68]. The cyan emitting (510 nm) quantum dots were synthesized by following the

procedure reported in literature [67]. The growth temperature was 300 °C and the growth time

was 10 min. Other larger quantum dots (green 550nm, yellow 570nm, and red 620nm) were

formed by reducing the ligand concentration. The resulting quantum dots showed a wide size

distribution with a FWHM of more than 50 nm. Moreover, the quantum dot dispersions were

cloudy with precipitates, which would potentially affect the film quality during device

fabrication. For QLED device application, better quality quantum dots with more uniform size

distribution and clear quantum dot dispersions are needed.

In the second approach the ligand concentration, growth temperature, and growth time

were kept constant. Instead, the starting precursor concentration ratios (Cd:Zn:Se:S) were

modified. In a typical single step synthesis, 0.1 mmol of Cadmium oxide and 4 mmol of Zinc

acetate were heated with 17.7 mmol of Oleic acid in a three neck round bottom flask. The

mixture was degassed with a 20 mTorr vacuum at 150 °C for 30 min to remove any volatile

impurities. After 30 min, clear solution mixtures of cadmium and zinc oleate were formed.

After degassing, 15 ml of octadecene was injected into the flask and the temperature was

increased. At 300 °C, 2ml of trioctylphosphine dissolving 0.2 mmol of Se and 3 mmol of S was

injected rapidly into the reactor. The reaction was allowed to continue for 10 min before the

reactor was rapidly cooled down to room temperature. The starting precursor ratio yielded cyan

emitting (533 nm) nanocrystals with a FWHM of 29 nm. By changing the precursor

concentration ratios blue, green, yellow, and orange quantum dots were synthesized. To

synthesize the red quantum dots, Se and S were injected separately [38]. Initially, 0.4 mmol of

Cadmium oxide and 4 mmol of Zinc acetate were heated with 5 ml of Oleic acid in a three neck

round bottom flask. The mixture was degassed at 150 °C for 30 min to remove any volatile

impurities. After 30 min, clear solution mixtures of cadmium and zinc oleate were formed. After degassing, 15 ml of octadecene was injected into the flask and the temperature was increased. At 300 ºC, 2ml of trioctylphosphine dissolving 0.85 mmol of Se was injected swiftly. The reaction was allowed to continue for 10 min. After 10 min, 1ml of trioctylphosphine dissolving 1 mmol of S was injected into the reactor. The reactor was cooled to room temperature after 10 min. The resulting nanocrystals were purified by precipitating with excessive methanol and hexane. The purification process was repeated at least 3 times before the nanocrystals were dried and dispersed in hexane at 25 mg/ml concentration for further experiments.   The second approach produced more uniform sized, well dispersed and clear quantum dot dispersions, which were used in the fabrication of the QLED

2.1.2. Nickel oxide synthesis

Nickel oxide thin films were used as one of the CTLs investigated for hole transport in all-inorganic QLED. Nickel oxide exists in two forms with Ni having two different oxidation states Ni^{2+} and Ni^{3+}. In a stoichiometric nickel oxide (NiO), Ni is present in the form of Ni^{2+} and it is a green colored powder. In its non-stoichiometric form (Ni_2O_3) it appears as a black powder. Stoichiometric nickel oxide is an insulator and non-stoichiometric form is a p-type semiconductor with excess holes formed due to Ni vacancies [69]. For hole transport, p-type semiconductor is required and so non-stoichiometric nickel oxide was synthesized. Two forms of nickel oxide were investigated namely thin film and nanoparticles.

2.1.2.1. Thin film

Non-stoichiometric nickel oxide thin film was formed by annealing a spin coated layer of nickel hydroxide at high temperature under ambient atmosphere [50, 62, 63]. First step of the

process involved the sol-gel synthesis of nickel hydroxide. Nickel hydroxide was formed by the

hydrolysis of nickel precursor with a weak base. In a typical synthesis, 0.5 M nickel acetate tetra

hydrate solution in ethanol was prepared at room temperature. Once the salt is completely

dissolved, equimolar diethanolamine was added under constant stirring and the reaction was

allowed to continue for 2 hrs at 60 ^{o}C on a hot plate. The initial turbid, light green colored

solution turned into a clear, dark green solution indicating the completion of the reaction. Here,

the diethanolamine not only acted as a weak base for hydrolysis, but also made the final solution

more viscous. This enabled the formation of uniform film when spin coated. The bright dark

green colored, clear nickel hydroxide solution is shown in figure 2.2(a). To form the nickel

oxide thin film, the nickel hydroxide sol-gel was spin coated at an optimized speed and annealed

in a box furnace at high temperature under ambient atmosphere. The resulting film exhibited a

pale brownish grey color indicating the non-stoichiometry of the final film. This is shown in

figure 2.2(b).

(a)   (b)
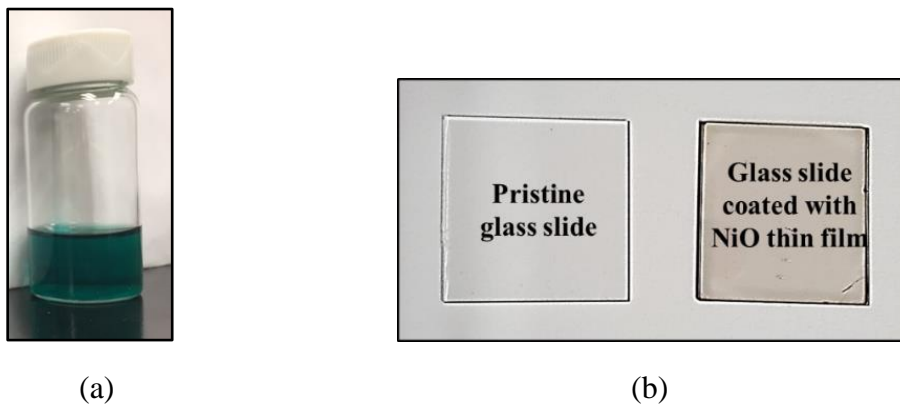
Figure 2.2. (a) The dark green and clear nickel hydroxide sol-gel is used as the precursor to the
formation of nickel oxide thin film. (b) Transparency of nickel oxide thin film on glass is
compared to that of a pristine glass slide. "Photo by Ramesh Vasan"

2.1.2.2. Nanoparticles

The second form of nickel oxide was the nickel oxide nanoparticle. This was synthesized by hydrolysis of nickel precursor by a strong inorganic base like sodium hydroxide followed by high temperature annealing [70]. Initially, 0.5M solution of nickel acetate tetra hydrate in DI water was prepared at room temperature. To this, freshly prepared 1M solution of sodium hydroxide in DI water was added dropwise over a 10 min period. The clear green solution turns into pale green precipitate. The precipitate was collected by centrifugation and the supernatant solution was discarded. The precipitate was washed 2 to 3 times with DI water and collected by centrifugation. The purified precipitate was then dried in a box furnace at 80 $^{\circ}$C for 2 hrs. The dried crystals were then ground into a fine powder and annealed at 360 $^{\circ}$C for 2 hrs. The resulting dark brown powder was the nickel oxide nanoparticle. The nanoparticles were then dispersed in 1-butanol at 20 mg/ml concentration, as shown in figure 2.3, using the ultrasonicator for further experiments.

Figure 2.3. Nickel oxide nanoparticles are dispersed in butanol for spin coating application. "Photo by Ramesh Vasan"

2.1.3. Zinc oxide nanoparticles

Zinc oxide nanoparticles were used as the ETL in the QLED devices. Zinc oxide is an n-type semiconductor with its conduction band position aligning well with the conduction band CdSe/ZnS alloyed core/shell quantum dots for electron transport [42-52]. Zinc nanoparticles

were synthesized by the hydrolysis of zinc acetate dihydrate solution with a strong base [41, 52]. Initially, 0.1M solution of zinc acetate di hydrate in methanol was prepared under room temperature. To this 0.48 gm of potassium hydroxide dissolved in 25 ml of methanol was added dropwise inside a N_2 filled glove box at 60 ^{o}C. The reaction was allowed to continue for 2 hrs to obtain a white precipitate. The zinc oxide nanoparticles were then washed with excess methanol and collected. The purification steps were repeated for at least 3 times and the final nanoparticle precipitate was dried under vacuum to form a white powder. The dried nanoparticles were dispersed in 1-butanol at 20mg/ml concentration for further experiments.

Figure 2.4. Zinc oxide nanoparticles are dispersed in 1-butanol for spin coating application. "Photo by Ramesh Vasan"

2.1.4. Quantum dots/nickel oxide thin film bilayer sample

Single layer and quantum dots on glass substrates and quantum dots/nickel oxide thin film bilayer sample on glass substrates were used to investigate the hole transport mechanism. Quantum dots dispersed in hexane were spin coated on ultrasonically cleaned glass substrates and annealed at 80 ^{o}C in a N_2 glove box to form the single layer sample. For bilayer samples, quantum dots were spin coated on 60 nm nickel oxide thin film grown on ultrasonically cleaned glass substrates. The quantum dots/nickel oxide thin film bilayer samples were then annealed at 80 ^{o}C in a N_2 glove box. The schematics of single layer quantum dot and quantum dot/nickel oxide bilayer samples are shown in figure 2.5 (a) and (b).

(a)   (b)
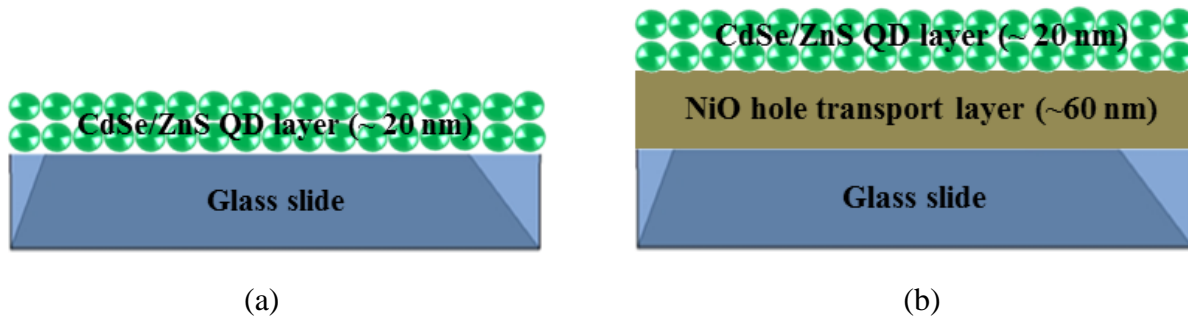
Figure 2.5. Quantum dots are spin coated on (a) pristine glass slide and (b) nickel oxide to measure the fluorescence lifetime.

2.1.5. Nickel oxide Schottky diode

The electrical properties of the nickel oxide thin film were extracted by analyzing the electrical characteristics of a Schottky diode. It was fabricated on a 2.5x1.25 cm^2 rigid glass substrate coated with 250 nm of FTO. The sheet resistance of the FTO was measured to be 7–10 $\Omega/\square$. It consists of an FTO forming an Ohmic contact and Al forming a Schottky contact with the nickel oxide. The FTO coated glass slide was patterned using adhesive plastic film, zinc powder, and HCl. The FTO under the plastic film was protected from the HCL, while the FTO parts exposed to zinc powder were etched away by the HCl. Patterned FTO glass samples were cleaned successively using DI water, acetone and isopropanol for 30 min each in an ultrasonic bath. The nickel hydroxide sol-gel was spin coated on cleaned FTO sample and annealed at 400 ºC on a hot plate for 10 min to form one layer of nickel oxide. The thickness of the nickel oxide film was ~100 nm. Two more layers of nickel oxide were formed using the same procedure. Final annealing was performed in a box furnace at 500 ºC for 30 mins to form a ~300 nm nickel oxide film. On top of the nickel oxide, 100nm Al metal was evaporated using an electron beam evaporator through a shadow mask forming an active area of 0.1cm^2. The evaporator chamber was maintained at a vacuum of 2e-6 Torr while deposition. The schematic of the FTO/NiO/Al Schottky diode is shown in figure 2.6.
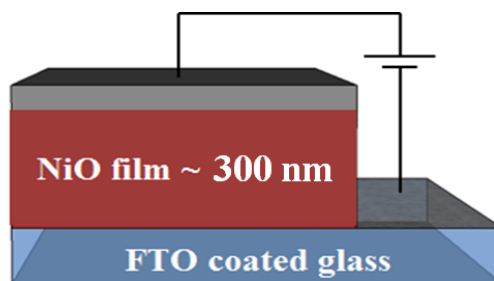
Figure 2.6. A Schottky diode using nickel oxide is fabricated to extract the electrical properties of the nickel oxide.

2.1.6. Thin film transistor

The mobility of the zinc oxide nanoparticles was calculated from the electrical characteristics of a thin film transistor with the nanoparticles in the channel [41, 52, 71, 72]. The transistor consists of a p-type Si sample with a 100 nm SiO_2 thermal oxide, which acted as the gate oxide. A bottom gate thin film transistor was used with source and drain electrodes formed on the gate oxide using standard photolithography procedure. The channel was formed by the interdigital electrodes with pads that formed the source and drain. The channel length and width were 50 µm and 1000 µm, respectively. The top source, drain and bottom gate electrodes were formed by depositing 100 nm Ag using an electron beam evaporator. The schematic of the thin film transistor is shown in figure 2.7. Zinc oxide nanoparticles dispersion in 1-butanol was spin coated on to the channel that was formed by the interdigital electrodes. The pads were cleaned gently to make contacts by using wedge wire bonding technique. To make contact to the bottom gate electrode, the sample was made to contact an Au coated substrate using molten In. Gold wire was wedge bonded to the Au substrate to make contact with the gate electrode.
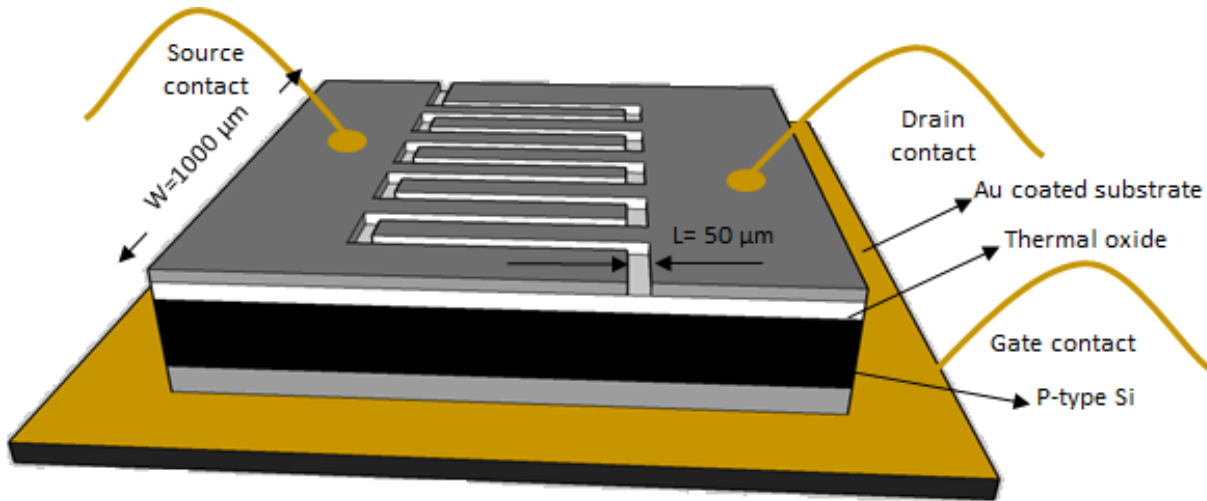
Figure 2.7. A thin film transistor with a bottom gate architecture and zinc oxide nanoparticle channel is fabricated to calculate the electron mobility in zinc oxide ETL.

2.1.7. QLED devices fabrication

The QLED devices were fabricated on a 2.5x1.25 cm^2 rigid glass substrate coated with 250 nm of FTO. The sheet resistance of the FTO was measured to be 7–10 $\Omega/\square$. The FTO coating was partly etched using zinc powder and concentrated HCl.   The FTO was partly covered with adhesive plastic tape and the parts exposed to zinc powder were etched away by HCl. Patterned FTO slides were cleaned in an ultrasonic bath successively using DI water, acetone, and isopropanol for 30 min each. For the all-inorganic QLED, the nickel hydroxide precursor sol-gel was spin coated on the cleaned, patterned slides and annealed in a box furnace at an optimized temperature to form the nickel oxide HTL. For the hybrid QLED device, the nickel oxide thin film is replaced with PEDOT: PSS hole injection layer (HIL)/nickel oxide nanoparticle HTL. The HIL/HTL layers were spin coated on cleaned FTO at 5000 rpm for 30 s and annealed under ambient atmosphere. For both device structures quantum dots dispersed in hexane was spin coated on the HTL at 2000 rpm and annealed inside a N$_2$ glove box at 80 $^\circ$C for 30 min. The zinc oxide nanoparticle ETLs was spin coated at 2000 rpm and annealed on a hot

30

plate inside a N$_2$ glove box. The optimized coating speed and annealing temperature enabled the formation of uniform films. Finally, 80 nm Al cathode was deposited using an electron beam evaporator through a shadow mask at a vacuum of 1e-6 Torr. The shadow mask was designed such that the active emissive area of the device formed was 0.15cm^2. The schematics of the all-inorganic and hybrid QLEDs are shown in figure 2.8 (a) and (b) [50].

(a)   (b)
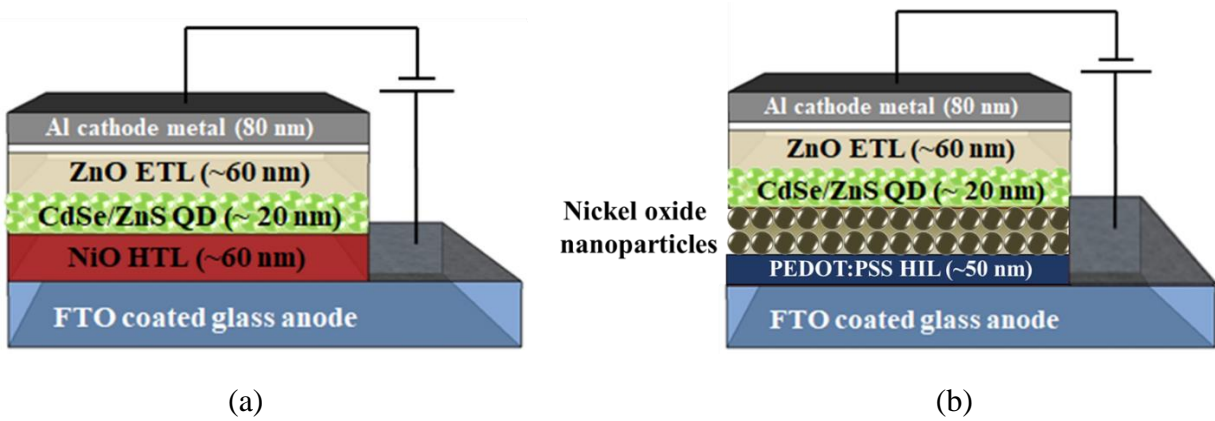
Figure 2.8. Schematics of (a) all-inorganic and (b) hybrid QLEDs that are fabricated using a layer-by-layer deposition technique. Reprinted with permission from Vasan *et. al.* [50].

2.2. Characterization tools

2.2.1. UV-Vis spectroscopy

UV-Vis spectrophotometry was utilized to measure the absorbance and transmittance of different materials in this project. A Cary 500 UV-Vis-NIR spectrophotometer was used to acquire the absorbance and transmission measurements. The range of wavelengths that can be measured is 175-3300 nm. It consists of a photomultiplier tube detector for UV-Vis region and a PbS detector for the infrared region. For liquid samples, a Spectrosil® Far UV Quartz cuvette with a range of 170 to 2700 nm and 1 cm path length was used. For measuring thin films, a sample holder with double sided adhesive tape was used. The bandgaps of the alloyed CdSe/ZnS quantum dots, nickel oxide thin film, and zinc oxide nanoparticles were calculated from the

absorbance spectrum. The position of the excitonic peak in eV observed in the absorbance spectra of these materials is approximately equal to the band gap of the material. Absorbance is calculated by using the Beer-Lambert law, which is given by equation 2.1.

$$I = I_0 \, e^{-\alpha d} \tag{2.1}$$

where, I the intensity of the light transmitted through the material, I_0 is the incident light intensity, α is the absorption coefficient, and d is the path length optical density of the material. Absorption coefficient is a material characteristic and is usually expressed with units of cm^{-1} and $\alpha d = \ln(I_0/I)$ is the absorbance with arbitrary units.

Transmittance of the nickel oxide HTL is an important parameter as the light emitted from the quantum dot active layer must be transmitted out without absorption. Transmittance is usually expressed as % of incident light. If none of the incident light is absorbed, it means the transmittance is 100% and if all the light is absorbed then the transmittance is 0%. Transmittance is given by equation 2.2.

$$\%T = \left(\frac{I}{I_0}\right) \times 100 \tag{2.2}$$

Nickel oxide thin film was grown on a rigid glass substrate and hence glass transmittance was used as a baseline.

2.2.2. Luminescence

Luminescence is defined as the radiative recombination of excitons formed due to excited carriers. The radiative recombination competes with the non-radiative recombination processes and must dominate to produce considerable luminescence. In this project photoluminescence and electroluminescence measurements were used to characterize materials and devices,

respectively. For luminescence to occur, non-equilibrium carrier concentration is required in the electronic bands. If this non-equilibrium is produced by optical excitation then the luminescence is called photoluminescence and if it is produce electronically be injecting carriers across a p-n junction, then it is electroluminescence. Other types like sonoluminescence, bioluminescence, chemiluminescence, cathodoluminescence, thermoluminescence, radio luminescence, triboluminescence are also possible.

In this project photoluminescence of all the materials used were measured to know the quality of the materials prior to device fabrication. The spectrum peak is approximately equal to the band gap of the material. Additionally, photoluminescence spectra of quantum dots can be used to determine the size distribution of the synthesized quantum dots. A narrow full width at half max (FWHM) indicates a narrow size distribution, which leads to pure color emission when in a device. In the case of electroluminescence, the increase in device emission intensity with bias voltage or injection is recorded as a function of wavelength. Like photoluminescence, the FWHM of spectrum is used to determine the color purity of the emission. The Photoluminescence and electroluminescence measurements at room temperature were performed using a Horiba LabRAM spectrophotometer equipped with Synapse CCD detector. The detector is a 1024x256 front illuminated Si CCD with a gain setting of 2.55 e$^-$/count. The CCD chip is electronically cooled to -70°C during measurement. For photoluminescence the excitation was achieved by a 473 nm continuous laser. The incident laser power is controlled by five neutral density filters selectable using the spectrometer software. The laser is focused on to the sample by 50x objective lens and 40 μm slit. The emitted photons from the sample is directed towards the detector through a vis-IR band pass filter and a 500 nm laser cut-off filter. For electroluminescence, the QLED device was biased using a 2400 Keithley source meter with a

current compliance of 1 A and the emission intensity was measured using the same spectrometer setup as the photoluminescence. A 10x objective lens and 500 μm slit width were used for the electroluminescence measurements.

2.2.3. Time resolved photoluminescence

Time resolved photoluminescence is a contactless technique to characterize the carrier recombination rates and transport properties of semiconductor materials for device applications. The measurement involves exciting the sample with short pulse laser usually on the ps or fs scale and subsequently measuring the photoluminescence decay as a function of time. The exciting source is picosecond or femtosecond pulsed laser and the detector is a photodiode with streak camera for time correlated single photon counting. Other filters, monochromator, optics, pin holes are used within the system. Time resolved photoluminescence using time-correlated single photon counting is used for II-VI quantum dot carrier dynamics as the time scales are in the nanosecond scales.

In this project lifetimes were measured using a MicroTime 200 scanning confocal fluorescence microscope (PicoQuant GmbH, Berlin, Germany), which is based on Olympus IX71 equipped with PicoHarp 300 TCSPC controller [73, 74]. It utilizes a 485 nm laser (PDL 485, Picoquant) operating in pulsed wave mode at a power of ~0.05 μW and a repetition rate of 4 MHz for excitation. A dichroic mirror (500dcxr, Chroma, McHenry, IL) sends the light through a water immersion objective (Olympus, Apochromat 60x, NA 1.3) to a diffraction-limited laser focus. The same objective collects the fluorescence and sends it through the same dichroic mirror and a 50 μm pinhole. To reject background fluorescence and scattered laser light, a fluorescence filter that best matches the emission wavelength of the quantum dots (HQ520/35M for blue

quantum dots with emission peak at 495 nm, HQ520/35M for cyan quantum dots with emission

peak at 530 nm, HQ560/40M for green quantum dots with emission peak at 550 nm,

HQ585/40M for yellow quantum dots with emission peak at 580 nm, HQ605/55M for orange

quantum dots with emission peak at 600 nm) was placed in front of the Single Photon Avalanche

Diode Detector (SPAD, MPI, Microphotonic devices, Bolano, Italy). The photons are binned

using the TCSPC card into 64 ps channels for fluorescence lifetime analysis and the fluorescence

lifetime curves were then analyzed using the freely downloadable program DecayFit

(Fluorescence Decay Analysis Software 1.3, FluorTools, www.fluortools.com) using the

instrument IRF for iterative reconvolution fitting.

2.2.4. Current-Voltage Characteristics

Current-Voltage characteristics were measured using a Keithley 4200 semiconductor

characterization system equipped with two source measure units (SMU) with 4200-PA pre-

amplifiers. The preamplifiers extend the resolution of the SMUs to 0.1 fA. The two SMUs were

used simultaneously to force and sense. Also, the Keithley Model 8101-TrX PIV test fixture was

used to perform four probe measurements with just two SMUs. In this project the current-

voltage characteristics of FTO/NiO/Al Schottky diode, the QLED, and zinc oxide thin film

transistor were measured using this system. The Schottky diode and QLED measurements were

performed using a built-in 2-wire forward bias diode test module. Source measure unit 1 was

connected to the device anode and was programmed to force and measure. The anode voltage

was swept from 0 to 10V and current was measured simultaneously. Source measure unit 2

connect to the cathode of the device was programmed to be the common. The characteristics of

thin film transistor were measured by setting up a user 3-wire test module. In this, the gate

voltage was swept with SMU 1 and the gate current was not measured. The drain voltage was

forced at a constant bias voltage using SMU 2 and the drain current was measured. The source was connected to the instrument ground. The Keithley interactive test environment modules setup to perform 2-wire and 3-wire measurements are shown in figure 2.9 (a) and (b).
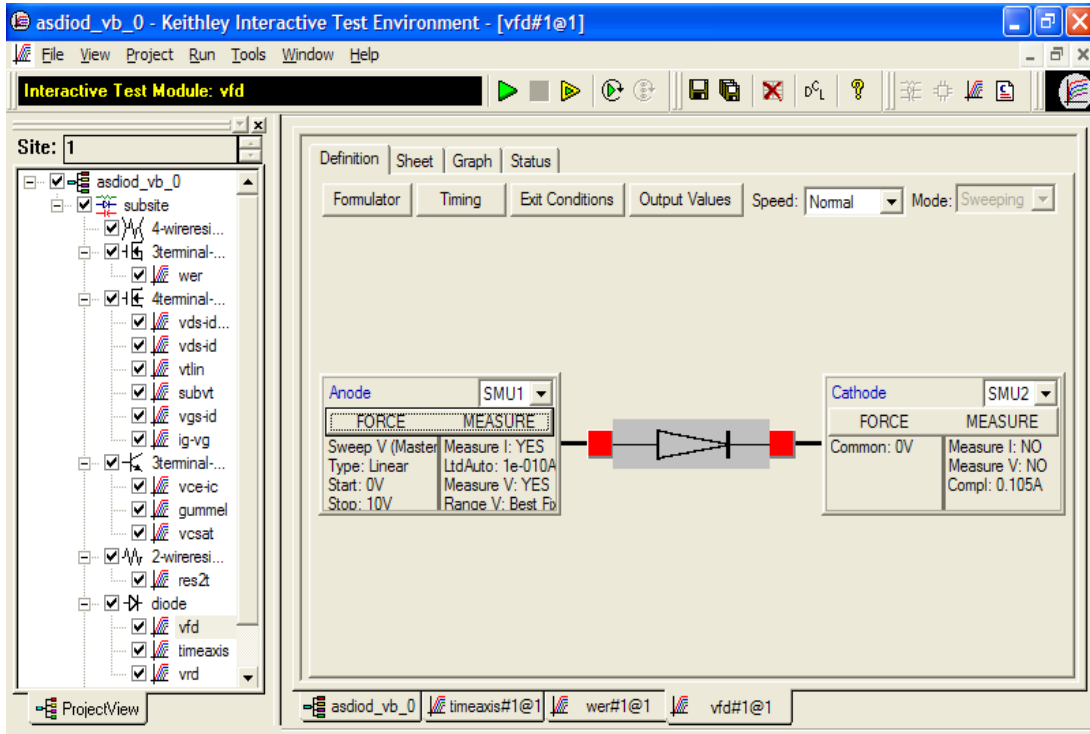
(a)
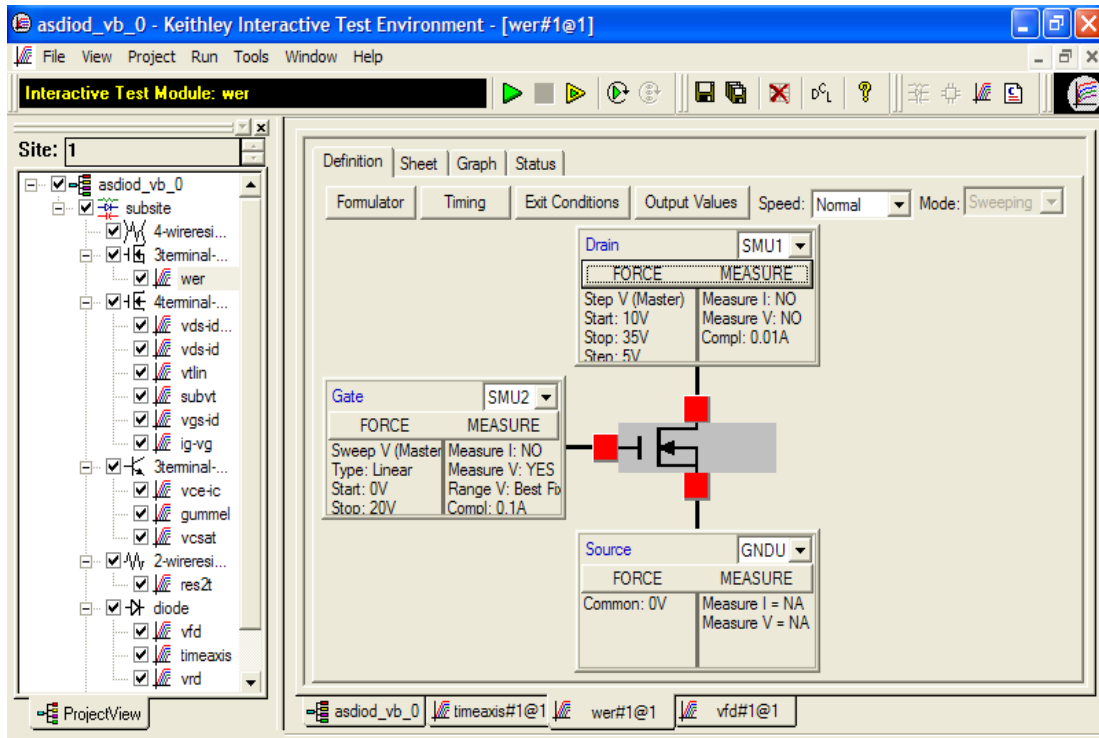
(b)

Figure 2.9. Screenshots of the Keithley test modules used for (a) 2 wire and (b) 3 wire device measurements.

2.2.5. Raman spectroscopy

The basic principle of Raman spectroscopy is that when a laser light is incident on the sample, the light is scattered inelastically by the optical phonons. The spectral distribution of the scattered light is compared with respect to the incident light. The intensity of inelastically scattered light is few orders of magnitude smaller than the elastically scattered light. So it is important that the elastically scattered light is filtered using an appropriate notch filter to detect the inelastically scattered light accurately. Other than optical phonons, incident light can also be scattered by quasi particles like optical magnons, plasmons and even electronic excitations [75]. The light can be shifted to higher energy as in anti-Stokes shift or lower energy as in Stokes shift. A schematic of Raman scattering mechanism is shown in figure 2.10.

37

Electronic
energy level

$\omega_s =$
$\omega_i - \omega_{phonon}$

$\omega_s =$
$\omega_i + \omega_{phonon}$

Incident
photon
ω_i

Scattered
photon
$\omega_s = \omega_i$

ω_i

ω_i

ω_{phonon}

ω_{phonon}

ω_{phonon}

Rayliegh Scattering
(elastic)

Stokes shift

Anti-Stokes shift

Raman Scattering
(inelastic)
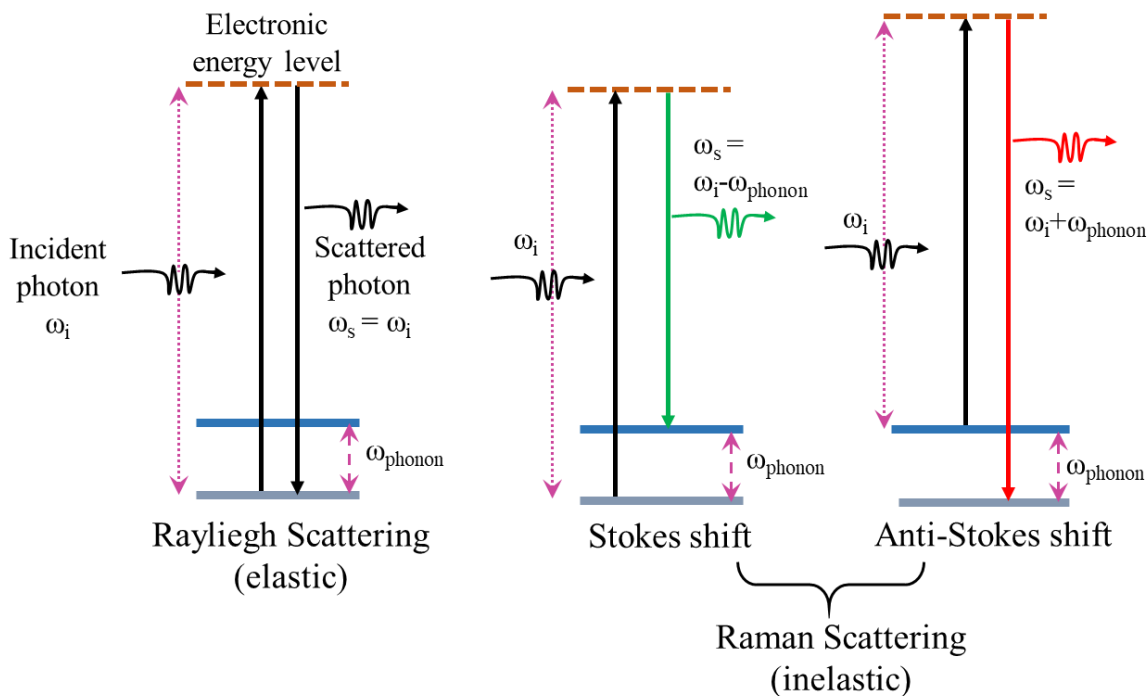
Figure 2.10. Energy band schematics of Rayleigh and Raman scattering mechanisms. Raman scattering can be of two types namely Stokes and anti-Stokes shifts.

In this project Raman spectroscopy was used to find the non-stoichiometry of grown nickel oxide thin film and nanoparticles qualitatively. Additionally, Raman spectroscopy was used to confirm the presence of different materials investigated by comparing the position of the phonon modes with existing literature. A Horiba LabRam micro Raman spectrometer equipped with a Synapse CCD detector was used in this project. The detector is a 1024x256 front illuminated Si CCD that is electronically cooled to -70°C during measurement. A 472.9 nm continuous laser was used as the excitation source. The notch filter used to remove the elastically scattered light cut-off the shifted light by around 150 cm^{-1}. So, technically with this instrument any shift less than this cannot be detected. For the materials that were used in this project, the shift was more than 400 cm^{-1} and so they can be detected accurately. Micro Raman measurements were performed using a 40 μm slit width and a 50x objective lens.

2.2.6. X-ray Diffraction

X-ray Diffraction (XRD) is a contact less material characterization technique used to identify elements, lattice spacing, crystal structures, and crystal orientation. In a crystalline structure, atoms are arranged in a periodic three-dimensional lattice. The space between two adjacent lattice point is called the lattice constant of the crystal. When a beam of high energy x-ray is incident on a crystal, they are scattered elastically from different planes of the crystal. This is called Thomson scattering. In this process the electrons oscillate at the same frequency of the incoming x-ray beam. The scattered x-ray beams from different lattice planes undergo interference, which are recorded as diffraction pattern. The spacing and intensity of the diffraction pattern are analyzed to determine crystal structure and identify elements. The patterns are analyzed using Bragg's law according to equation 2.3.

$$2d \sin \theta = n\lambda \tag{2.3}$$

where, n is a positive integer and λ is the wavelength of the incident wave, d is the distance between the diffracting lattice planes, and θ is the scattering angle.

In this project XRD measurements were performed to optimize the annealing temperature, time, and environment to obtain nickel oxide thin film with large gain size. Additionally, XRD measurements were utilized to check for non-stoichiometry and crystallinity of charge transport layers used in this project. The samples were measured using Philips PW 3040 X'PERT MRD High Resolution XRD.

2.2.7. X-ray Photoelectron Spectroscopy

X-ray photoelectron spectroscopy (XPS) is a non-destructive material characterization

technique used to determine the elemental composition, chemical and electronic states in a

material. In this, high energy x-rays are used as an excitation source and inner shell electrons are

ejected out of the sample by Auger process or by photoemission process. The kinetic energy of

the ejected electron is detected, and properties of the material are determined. The electron

energy is raised to the detector level and need not be raised to vacuum level. In Auger process,

an excited electron recombines with a hole and the energy is transferred to another electron,

which gets ejected out of the material. The energy of the released electron is approximately

equal to the recombination energy. In photoelectron spectroscopy, a hole is left releasing the

electron form the core or valence levels. In this case the kinetic energy of the released electron is

measured instead of the Auger process or the recombination energy. The Auger and

photoemission processes are schematically represented in figure 2.11. In XPS, high energy
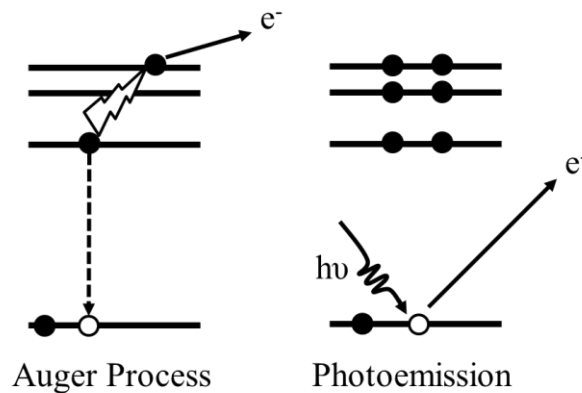
Figure 2.11. Auger and photoemission are the processes associated with X-ray photoelectron spectroscopy.

x-rays strike the surface of the material and penetrate the surface to about 10-20 nm. The kinetic

energy of the emitted electrons is used to calculate the binding energy of the electrons to the core

shells. The binding energy is a characteristic of the element being examined. The binding

energy is calculated using equation 2.4.

$$E_{BE} = E_{X-ray} + (E_{KE} - \varphi) \qquad (2.4)$$

where, E_{BE} is the binding energy of the emitted electron, E_{X-ray} is the energy of the incident x-

ray, E_{KE} is kinetic energy of the emitted electron as seen by the detector and φ is the work

function dependent on the spectrometer and the material. This is schematically represented in

figure 2.12.
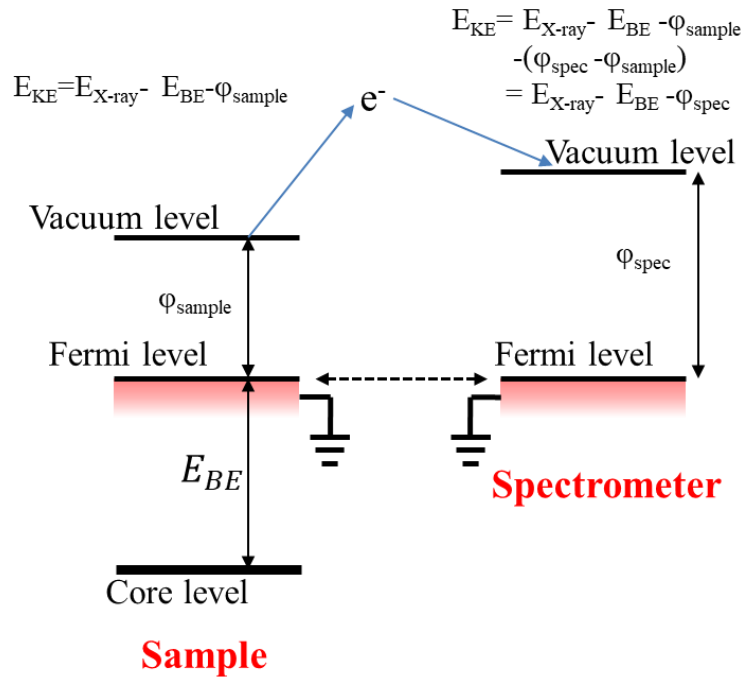
Figure 2.12. The principle of X-ray photoelectron spectroscopy is shown in the schematic.

A typical spectrum consists of number of electrons or intensity (y-axis) plotted as a

function of the binding energy (x-axis) of the emitted electrons. The peaks observed at certain

binding energies in the XPS spectrum are characteristic of the element. The number of electrons

in each of the characteristic peaks is directly related to the amount of element within the material. In a typical system, a monochromatic Al kα X-rays are produced by focusing a beam of electrons on to an Al disk. The resulting Al kα X-rays have an energy of 1486.7 eV [76]. The X-rays are focused on the sample loaded on to an ultra-high vacuum chamber ($<10^{-9}$ mb). The emitted core electrons are then directed toward the electron analyzer and electron detector to record the binding the energy and intensity, respectively.

2.2.8. Atomic Force Microscope

Atomic Force Microscope (AFM) is a scanning probe microscopic technique used to image the topographical features of samples that can be conductive or insulating. It is more advantageous to use AFM over electron microscopes for topographical imaging as the sample need not be electrically conductive. It consists of a pyramid shaped probe that is 3-6 µm in length with a tip diameter 0f ~25 nm, and AFM measures the force between the force and the sample surface. The probe is mounted at the end of a cantilever that is made of silicon or silicon nitride. To measure the surface features of the sample the cantilever tip is rastered across the sample continuously or intermittently and the deflection of the cantilever from the surface feature is monitored. Most common to measure the deflection is to reflect a laser from the cantilever on to a four-segment photo sensitive photodiode [77]. A simple schematic of an AFM is shown in figure. AFM operate in three different modes namely, contact mode, tapping mode and non-contact mode. In contact mode, the probe tip is contacted to the sample surface and dragged across forming the topographical image of the surface. The main disadvantage of this is the artifacts created due to damage of the probe or the surface caused by attractive forces. To overcome this tapping mode is widely used for high resolution images without the limitations of the contact mode. The cantilever is made to oscillate at a frequency close to the resonant

frequency (50-500 kHz) of the cantilever with a piezoelectric crystal. The oscillation amplitude produced when the tapping probe passes through a depression or bump changes and is recorded to map the topology of the sample surface. In non-contact mode, the much weaker Vander Waal's forces compared to contact forces between the probe tip and surface is measured. This is rarely used as the resolution is much lower than contact or tapping mode measurement. In this project, a Veeco Dimension 3100 AFM was used to measure the surface topology and roughness of the nickel oxide thin film. It is critical to have a very low surface roughness as this can affect the uniformity of the spin coated quantum dot active layer.
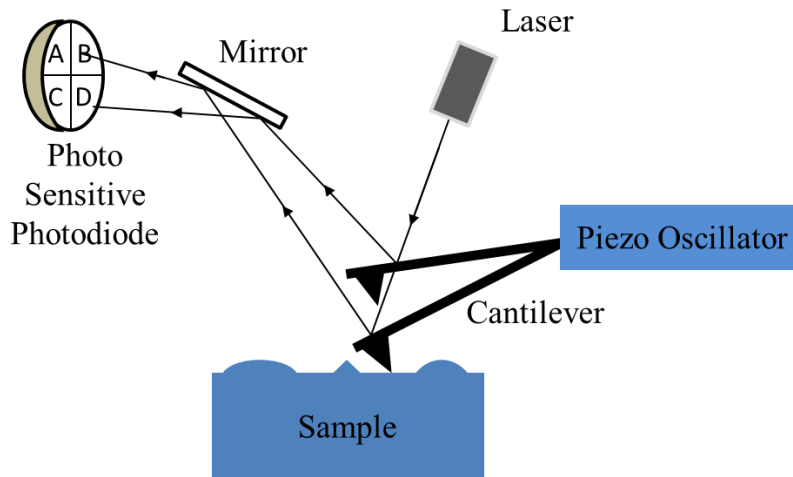
Figure 2.13. Schematic of an atomic force microscopy used to measure the morphology of the sample surface is shown.

3. RESULTS AND DISCUSSION

In this chapter, the first section discusses the material characterization results of CdSe/ZnS alloyed core/shell quantum dots, nickel oxide thin, nickel oxide nanoparticles and zinc oxide nanoparticles. Second section explains the results of the quantum dot-nickel oxide bilayer samples and the proposed charge transport models. In the final section, the device characterization results of QLED fabricated using nickel oxide thin film and nickel oxide nanoparticle as HTLs are discussed in detail.

3.1. Material Characterization

3.1.1. CdSe/ZnS alloyed core/shell quantum dots

3.1.1.1. Optical Properties

The CdSe/ZnS alloyed core/shell quantum dots were synthesized using two different procedures. In the first procedure, the ligand concentration is changed keeping the precursor concentration, reaction time, and reaction temperature constant. As soon as the Se and S are injected into the reactor, the Cd and Se start to react first and starts to nucleate. By changing the ligand concentration, the initial core growth can be controlled, which controls the bandgap of the final quantum dots. For the cyan quantum dots the initial ligand concentration is 17.7 mmol. In order to synthesize larger quantum dots with lower gaps the starting ligand concentration is reduced there by allowing the cores to grow larger. The photoluminescence spectra of different sized quantum dots synthesized by changing ligand concentration are shown in figure 3.1 (a) and (b). The FWHM of the cyan, green, yellow, orange and red quantum dots are 40, 50, 48, 52 and 46 nm, respectively. This indicates that quantum dots have a slightly wider size distribution, when compared to some reported results [57]. The absorbance spectra of the quantum dots are

shown in figure. Similar to photoluminescence spectra, the wide excitonic peak indicates a wider size distribution. The final quantum dot dispersions formed using this method are cloudy, which affects the uniformity and quality of the spin coated emissive layer.

The optical properties of the CdSe/ZnS alloyed core/shell quantum dots that were synthesized by changing the precursor concentration ratios are plotted in figure 3.1 (c) and (d). The FWHM of the photoluminescence spectra of blue, cyan, green, yellow, orange and red quantum dots are 29, 29, 30, 40, 45 and 34 nm, respectively. The narrow size distribution is advantageous in a device as the emission color will be pure and saturated. The band gap and size of the quantum dots are calculated using the excitonic peak seen in the absorbance spectra shown in figure. Compared to the previous procedure, this procedure produced quantum dots that are completely dispersible in hexane and form clear solutions. The quantum dot dispersions under the UV illumination is shown in figure 3.1 (e) and (f). The precursor concentration, PL peak, bandgap and size of the quantum dots are tabulated in table.

(a)   (b)
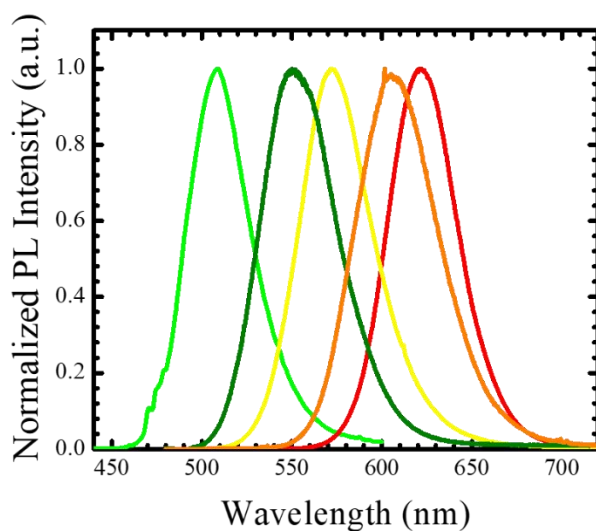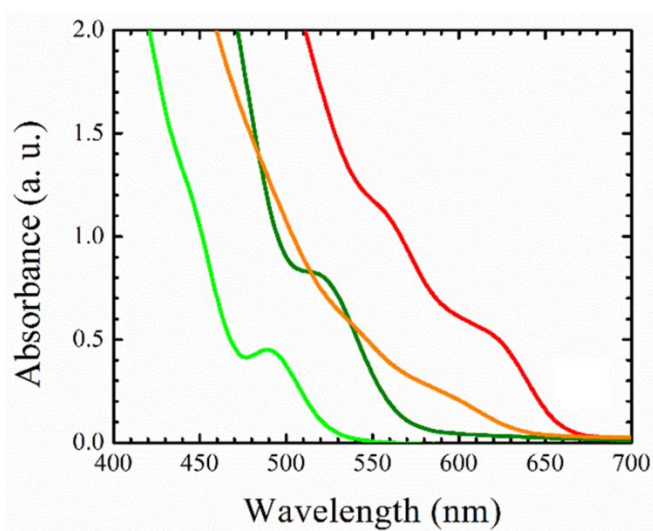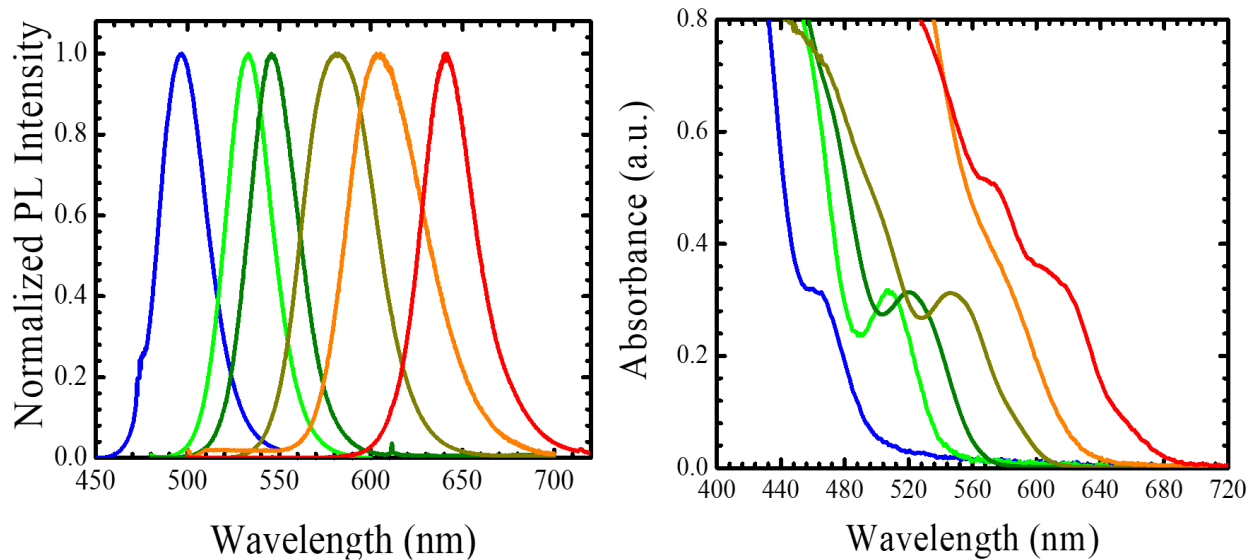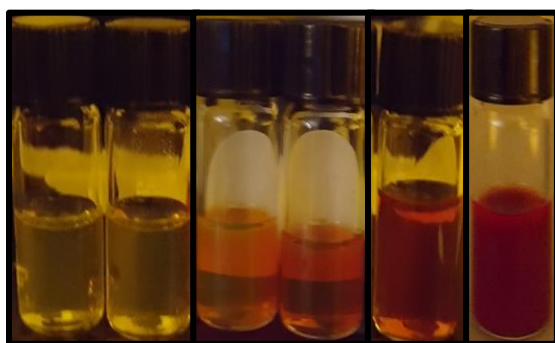
Figure 3.1. Optical properties of alloyed quantum dots synthesized by changing the ligand concentration are evaluated using (a) photoluminescence and (b) absorbance spectra. Reprinted with permission from Vasan *et. al.* [50]. Optical properties of alloyed quantum dots synthesized by changing the precursor concentration are evaluated using (c) photoluminescence and (d) absorbance spectra. Quantum dot dispersions under (e) white light and (f) UV light.

Table 3.1. The starting precursor ratios and properties of the different alloyed quantum dots used in this project are tabulated

Emission color	Starting precursor ratio Cd:Zn:Se:S (mmol)	PL peak (nm)	PL FWHM (nm)	Band Gap (eV)	Size (nm)
Blue	0.1:4:0.1:3	495	29	2.69	3.96
Cyan	0.1:4:0.2:3	530	29	2.44	4.62
Green	0.4:4:0.4:3	555	30	2.38	4.84
Yellow	0.4:4:1:2.3	580	40	2.27	5.30
Orange	0.4:4:0.4:4	606	45	2.13	6.18
Red	0.4:4:0.85:1	640	34	1.93	7.50

3.1.1.2. Lifetime measurements

The CdSe/ZnS alloyed core/shell quantum dots' lifetimes are measured to understand the quality and to estimate the fluorescent quantum yield. The quantum yield of the quantum dots are critical for fabricating an efficient QLED. The carrier lifetime measurements are also used to study the charge transport between the HTLs and the quantum dots. The lifetimes of the quantum dots are measured in solution and as a thin film on glass substrates. The decay curves are then fitted using deconvolution fitting with four exponential functions, which is the minimum number needed as determined from the residuals, consistent with previous studies [78, 79]. The average lifetime is then calculated using the equation 3.1.

$$\tau_{avg} = \sum_{i=1}^{4} \frac{a_i \tau_i^2}{a_i \tau_i} \qquad (3.1)$$

where, a_i and τ_i are the amplitude and characteristic decay times of the ith exponential component, respectively. The laser was focused onto several positions on each sample and the average value and standard deviation from each τ_{avg} from each point are calculated to obtain the

$\tau_{QD\text{-}avg}$ of that quantum dot. Figure 3.2 (a) to (f) show the decay curves of six different quantum dots in solution and as a thin film on glass substrates. The decay curves are recorded for a constant 300 s and normalized to 1 for fitting and comparison. It can be noted that the lifetime of the respective quantum dots in solution is much longer than that of the film on both bare glass. This can be attributed to the self-quenching effect of close packed films, which is absent when the quantum dots are dispersed in solution [53]. These curves are fitted using four exponentials functions and the amplitude and decay time parameters are extracted. An example fit performed using deconvolution fitting with the instrument response function is shown in figure 3.3. It is
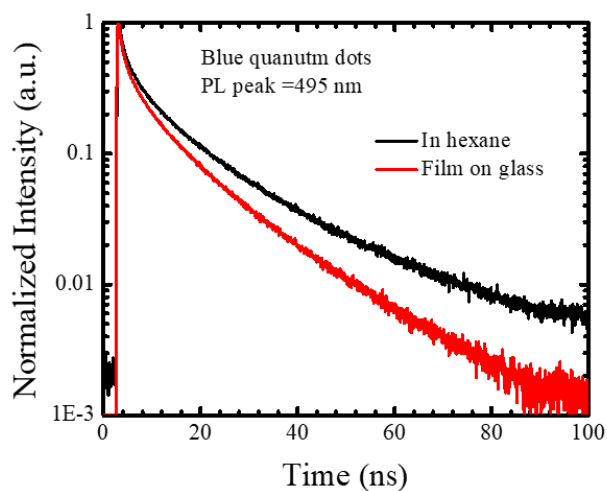
(a)
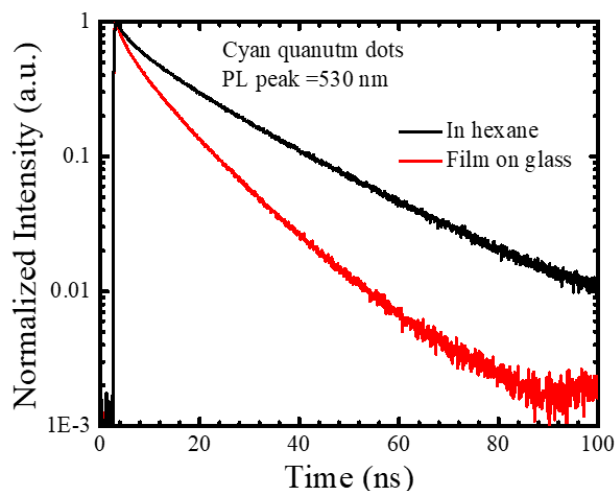
(b)
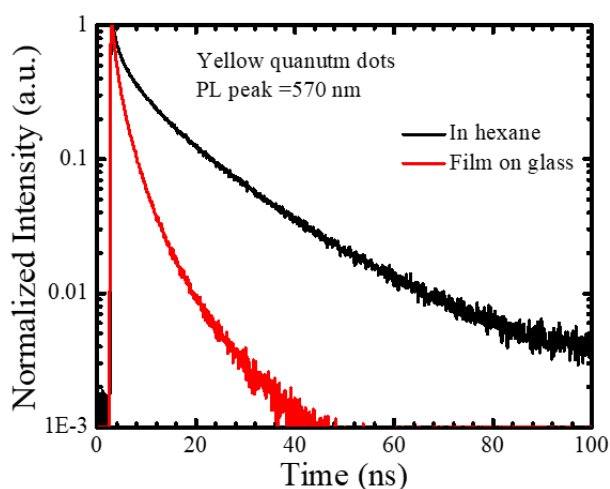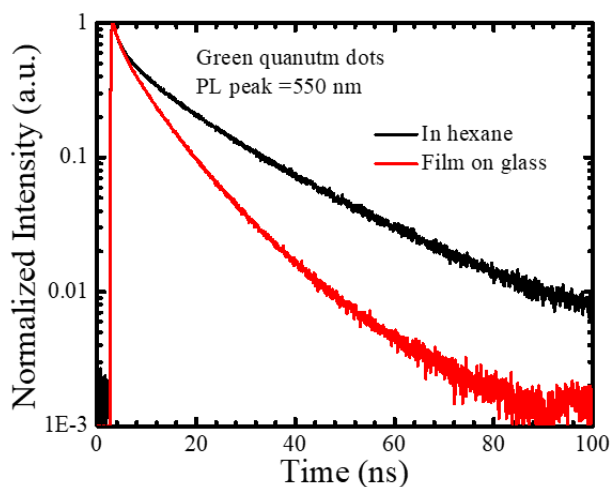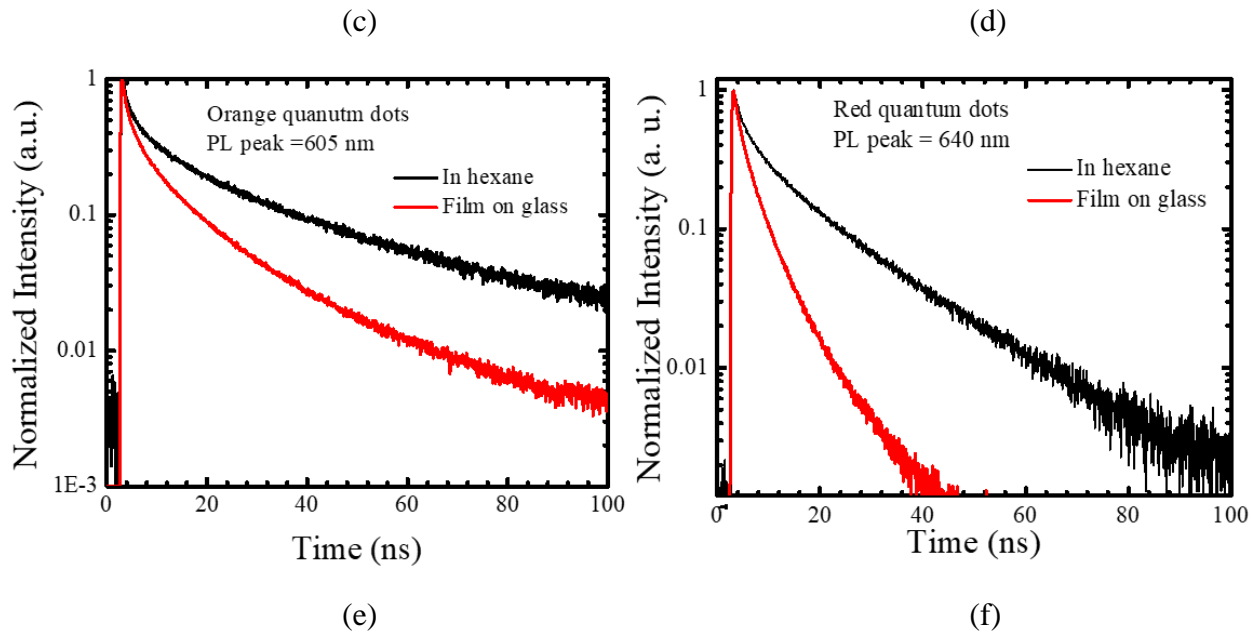
Figure 3.2. Lifetime decay curves of alloyed quantum dots that are measured in solution and as a spin coated film on glass.

clear from the figure 3.3 that the fitting is good with very low residuals. So, the average lifetime

of carriers calculated using this fit is accurate and the values are tabulated in table 3.2.
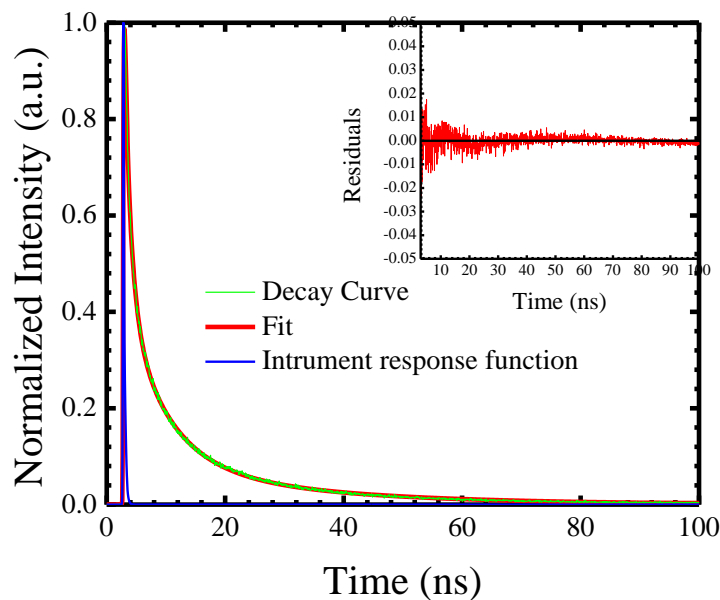
Figure 3.3. Sample decay curve fit using reconvolution fitting method plotted with original decay curve and instrument response function. The residuals of the fitting are plotted in the inset.

Table 3.2. Average lifetime of the different colored quantum dots that are calculated using equation 3.1 are tabulated.

Sample	Average lifetime, $\tau_{QD\text{-}avg}$ (ns)	
	Dispersed in hexane	Spin coated film
Blue	17.01	8.69
Cyan	20.82	10.05
Green	18.78	8.90
Yellow	13.10	3.42
Orange	31.67	15.35
Red	11.35	4.30

3.1.2. Nickel oxide thin film

3.1.2.1. Structural properties

The structural properties of the nickel oxide thin film are evaluated by measuring the XRD and Raman measurements. The growth conditions such as annealing temperature, annealing profile, and annealing atmosphere of the nickel oxide thin films are optimized using XRD measurements. To optimize the growth temperature, nickel hydroxide precursor solution is spin coated at 3000 rpm for 30 s on five different glass samples. These nickel hydroxide samples are then annealed at different temperatures and their XRD patterns are recorded. Amorphous nickel oxy hydride, nickel hydroxide and other intermediaries formed during the annealing process will not show prominent diffraction peaks associated with nickel oxide thin film. This is possible when nickel hydroxide samples are annealed at too high or too low temperatures. The quick gonio scans of the films annealed at 450 °C, 500 °C, 550 °C and 600 °C for a constant time

50

of 20 min show characteristic peaks of nickel oxide at 37° and 43.2°. This is shown in figure 3.4

(a). As seen in the figure the nickel hydroxide films annealed at 500 °C and 550 °C exhibit

relatively strong peaks corresponding to nickel oxide, while at 450 °C and 600 °C the peaks show

reduced intensities. So, the optimal annealing time and temperature is 20 min and 500 °C,

respectively. Next, the annealing atmosphere is controlled to deduce the effect of oxygen during

the annealing process. This is critical as the stoichiometry of the final nickel oxide film is

strongly dependent on the oxygen concentration. So, two nickel oxide samples are prepared at

the optimized conditions under ambient air in a box furnace and under vacuum in a tube furnace.

The XRD patterns of the two samples are shown in figure 3.4 (b). It is clear that the nickel oxide

sample annealed under ambient air shows much better crystallinity than the sample annealed

under vacuum. This is evident from the stronger characteristic nickel oxide diffraction peaks at

37° and 43.2°. The sample that is annealed at 500 °C for 20 min in the ambient atmosphere is

polycrystalline with a grain size ranging around 8-9 nm. The grain size is calculated using the

Scherrer's as shown in equation 3.2.

$$d = \frac{K\lambda}{\beta\theta} \tag{3.2}$$

where, d is the grain size or crystallite size, K is the dimensionless quantity equal to unity, λ is

the wavelength of the incident X-ray, which is equal to 1.54 Å (Cu kα line), β is the FWHM of a

diffraction plane, and θ is the Bragg angle. The annealing process is further optimized to

increase the grain size and thereby reduce the scattering due to these grain boundaries. To

achieve this five nickel hydroxide samples are annealed at different annealing profiles to increase

the grain size. First four samples are annealed inside a box furnace and the last sample is

annealed on a hot plate. The annealing profiles are as follows,

Sample 1: 0 - 400 °C @10 °C per min, 400 – 500 °C @33.3 °C per min, soak for 20mins @500 °C, ramp down naturally.

Sample 2: 0 - 400 °C @10 °C per min, 400 – 500 °C @25 °C per min, soak for 20mins @500 °C, ramp down naturally.

Sample 3: 0 - 400 °C @25 °C per min, 400 – 500 °C @25 °C per min, soak for 20mins @500 °C, ramp down naturally.

Sample 4: 0 - 400 °C @25 °C per min, 400 – 500 °C @33.3 °C per min, soak for 20mins @500 °C, ramp down naturally.

Sample 5: 0 - 500 °C on a hot plate, ramp up and ramp down naturally.

The XRD patterns of these samples are shown in figure 3.4 (c). The gran size of the samples that are calculated using Scherrer's equation are tabulated in table 3.3. The plane at 43.2° is used to calculate the d in nm. The FWHM is obtained by fitting the diffraction plane centered at 43.2° using a Voigt fit. It is clear from these experiments that the nickel hydroxide samples annealed in a box furnace with an initial ramp rate of 25 °C per min, a final ramp rate of 33.33 °C between 400-500 °C, annealing time (soak time) of 20 min in ambient air produced the required polycrystalline thin film of nickel oxide.

(a)

(b)

(c)
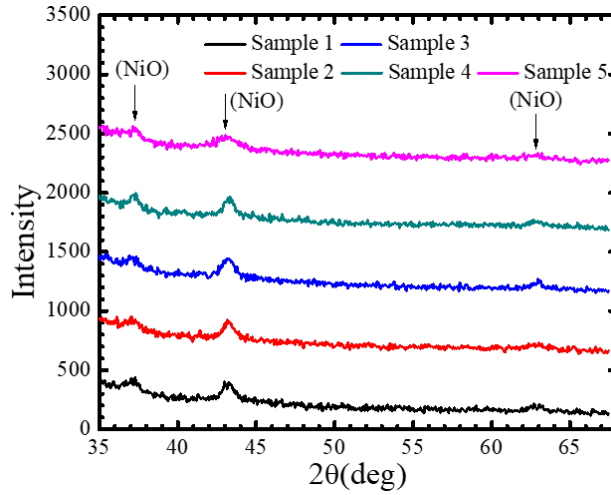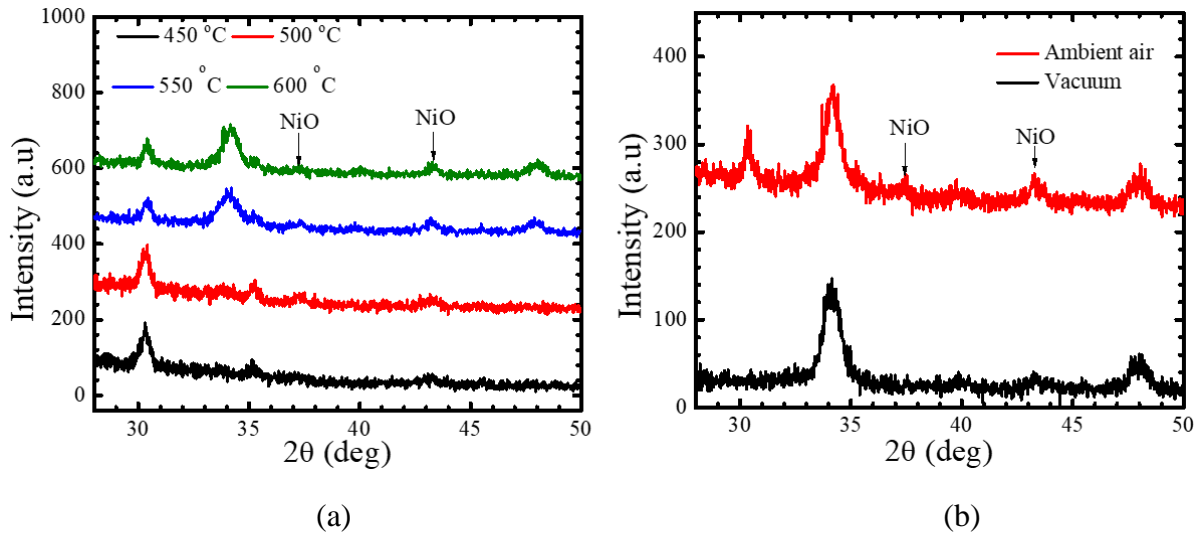
Figure 3.4. The annealing conditions of nickel oxide thin film are optimized using XRD measurements.

Table 3.3. The grain size of polycrystalline nickel oxide thin film formed using different annealing profiles calculated using Scherrer's equation

Sample	θ (deg)	β(deg)	d (nm)
1	21.6	0.72477	11.78439
2	21.61	0.668	12.78677
3	21.59	0.7708	11.0799
4	21.62	0.62893	13.58204
5	21.50	1.2281	6.9498

The sotichiometry of the nickel oxide formed utilizing the above optimal processing conditions is further investigated using XRD measurements. A detailed grazing angle scan of the nickel oxide film is shown in figure 3.5. The diffraction peaks at 37.2º, 43.3º, and 63.9º correspond to (111), (200), and (220) planes of the non-stoichiometric nickel oxide [52, 62]. The positions of the diffraction peaks for stoichiometric nickel oxide (JCPDS card no: 01-089-7130) are also referenced by vertical lines in figure 3.5. When compared to the crystalline nickel oxide pattern referenced in the figure, the patterns are broad indicative of smaller grain size and high defect densities. The position and relative intensity of the XRD pattern of the measured nickel oxide film also strongly indicate that the film is non-stoichiometric with Ni vacancies. The position of the peak corresponding to diffracting planes (111), (200), and (220) are shifted to higher 2θ. The peak for (200) plane is shifted by 0.4º from 42.9º for the stoichiometric nickel oxide to 43.35º for the non-stoichiometric nickel oxide. Similarly, (111) and (220) are shifted by 0.21º and 0.45º, respectively. Vacancies can also reduce the intensities of the diffracting planes. The highest intensity peak at 43.35º is taken as the reference and relative intensities of the other peaks are calculated. The (220) plane peak is 34.1% of the reference intensity, which is lower compared to stoichiometric nickel oxide. Both the peak shift and intensity reduction are due to the presence of defect in the form of Ni vacancies and O interstitials [80].
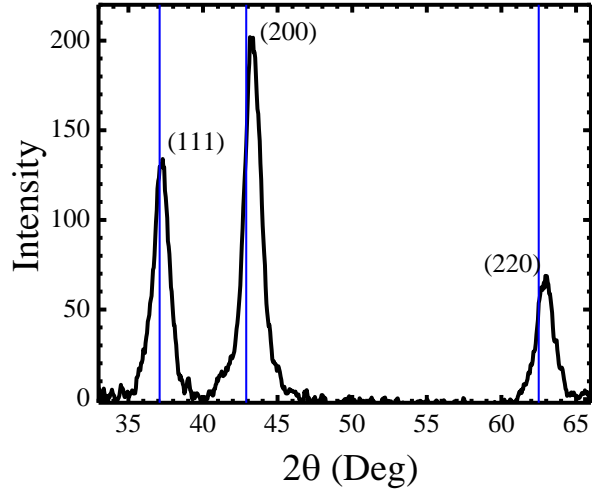
Figure 3.5. The crystallinity of solution processed non-stoichiometric nickel oxide HTL is determined from the XRD measurement. The diffracting planes (111), (200), and (222) of non-stoichiometric nickel oxide are indexed and compared to the stoichiometric nickel oxide (JCPDS card no: 01-089-7130).

The structural properties of non-stoichiometric nickel oxide are further evaluated using Raman spectroscopy. The Raman spectrum, recorded in the range of 300-1500 cm^{-1}, is shown in figure 3.6. The Raman mode at 560 cm^{-1} is a LO mode while the mode at 1100 cm^{-1} is a 2LO mode. The characteristic LO mode for stoichiometric nickel oxide appears at 510 cm^{-1} and this mode shifts to higher wavenumber of 560 cm^{-1} for non-stoichiometric nickel oxide due to Ni vacancies induced by excess O_2 [66].
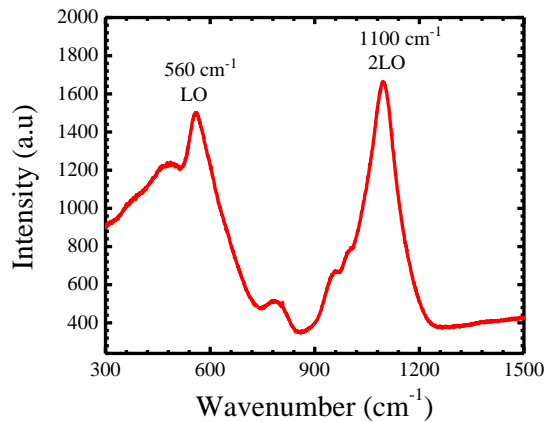
Figure 3.6. Raman spectrum of non-stoichiometric nickel oxide grown by annealing sol-gel film of Ni(OH)$_2$. Reprinted with permission from Vasan *et. al.* [50].

The composition of the nickel oxide film prepared by sol-gel method is determined by XPS measurements. It is important to know the composition of the nickel oxide as the stoichiometry can be determined and quantified, which is not possible using XRD. The XPS survey of the film, shown in figure 3.7, indicates the presence of Ni, O and C. The peaks of interest in this survey are the Ni2p$_{3/2}$ and O1s. Detailed analysis of these bands would give more information about the elemental composition and the chemical states of the Ni and O atoms.
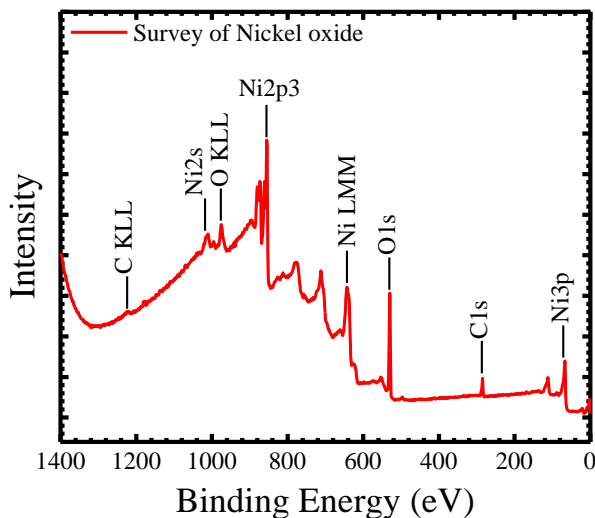
Figure 3.7. XPS survey of the nickel oxide thin film is indicating presence of Ni, O and C atoms.

The detailed XPS spectrum for the Ni2p3/2 state is shown in figure 3.8(a). The original spectrum is fitted with three Gaussian peaks. The peak centered at 853.57 eV binding energy corresponds to the Ni^{2+} oxidation state of Ni from stoichiometric nickel (II) oxide. The higher binding energy peak centered at 855.3 eV corresponds to the Ni^{3+} oxidation state, which is a result of non-stoichiometric nickel (III) oxide or nickel oxyhydride formed due to nickel vacancy and oxygen interstitial defects [62, 63, 80]. Finally, the peak at 861 eV is due to the shake-up process. Some of the ionized atoms formed during the excitation process end up at a higher energy than the ground state. The kinetic energy of the photoelectron emitted from these species

is decreased and appears as shake-up process at higher binding energy when compared to the main peak. Figure 3.8(b) shows the XPS spectrum O1s state. The peaks at 529.1 eV and 530.98 eV correspond to nickel (II) oxide and nickel (III) oxide or nickel oxyhydride, respectively [62, 63, 80]. The stoichiometry of the material is determined by comparing the integral area of the fitted peaks. The atomic ratio of Ni to O in the film is 1:1.70 indicating a Ni deficient film. Stoichiometric nickel oxide, which exhibits a rock salt structure has a 1:1 atomic ratio. Also, the ratio of Ni^{2+} to Ni^{3+} in the film is 1:2.45. The presence of more Ni^{3+} indicates that the film is non-stoichiometric as the formation of Ni^{3+} oxidation state is due to Ni vacancy.

(a)   (b)
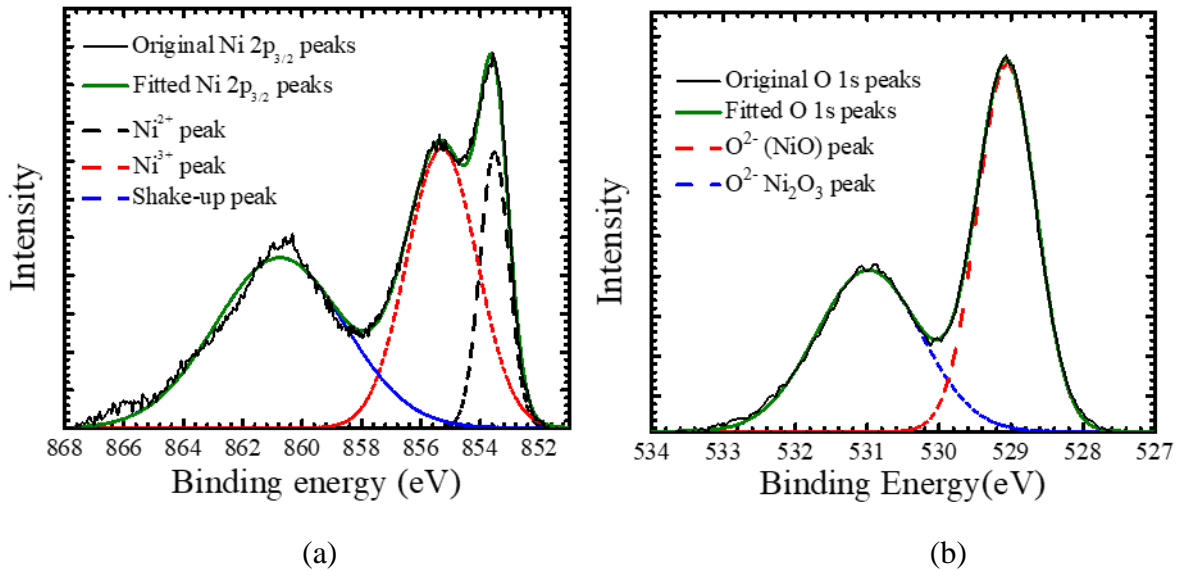
Figure 3.8. The composition of the nickel oxide HTL is measured from the integral area of (a) Ni peaks of Ni2p3/2 and (b) O peaks of O1s curves from the XPS spectrum of nickel oxide.

From the structural and compositional properties investigated using XRD, Raman and XPS spectroscopies it is clear that the nickel oxide film used in this project non-stoichiomrtic with defects. The film is further characterized by investigating the optical and electrical properties.

3.1.2.2. Morphological properties

The nickel oxide thin film is polycrystalline with grain size ~13.6 nm. The QLED is fabricated by layer by layer deposition and hence the interficial properties between adjacent layers play a significant role in device operation. It is critical that the layers are uniform with very low roughness to reduce interficial defects and traps. The surface morphology of the nickel oxide film grown by the optimized process is evaluated using AFM. The 2D ans 3D AFM images of the sample on glass with a scan area of 1x1 μm^2 are shown in figure 3.9 (a). The RMS and mean roughness are calculated by processin gthe AFM results using the Nanoscope AFM imag eanalysis software. The average roughness is 1.24 nm and the RMS roughness is 1.7nm as seen in th results shown in figure. These values are comparable to the roughness of organic HTLs commonly used with hybrid QLEDs [53]. The thickness of the HTL for QLED applications should be less than 100 nm as the mobility and conductivity of these materials are lower compared to other semiconductors. The thickness of the nickel oxide used in this project is optimized by spin coating the precursor sol-gel at different spin speeds. A 60 – 70nm film is obtained when the precursor is spin coated at 5000 rpm for 30 s. This is measured using a cross sectional SEM image as shown in figure 3.9(b).
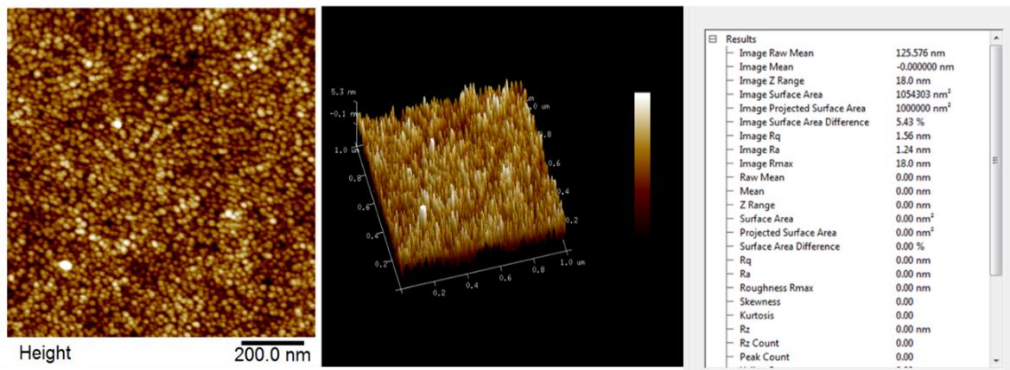
(a)
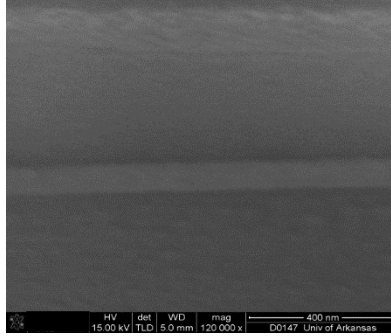
(b)

Figure 3.9. (a) 2D AFM images of the nickel oxide film are used to determine the surface quality of the film. The RMS roughness is ~1 nm indicating a very smooth film. (b) Thickness of the nickel oxide thin film is measured using a cross-sectional SEM image

3.1.2.3. Optical properties

The optical properties of the nickel oxide thin film are investigated by measring the absorbance and photoluminescence spectra. For absorbance measurement, glass is used as the baseline. The glass absorbance is measured between 200 – 800nm with an interval of 1nm. A nickel oxide thin film is grown on the glass using the optimized procedure and the absorbance of nickel oxide and glass are measrued. The spectrometer program automatically subtracts the glass baseline absorbance and the final spetrum is purely of nikcel oxide thin film. The baseline and absorbance of nickel oxide thin film are shown in figure 3.10 (a). The broad visible abrobance between 470 and 660 nm with a peak centered at 552 nm is from the defect levels within the band gap of nickel oxide. Band gap of nickel oxide is usually reported between 3.2 to 3.7 eV [62, 63, 69]. For the non-stoichiometic nickel oxide used in this project the band gap is found to be as 3.22 eV. This is calculated from the band edge absrobance peak of the absorbance spectrum centered at 385 nm. This peak can be clearly seen in figure.   The photoluminescence spectrum of the nickel oxide thin film is shown in figure 3.10 (b). The wide spectrum is due to emission from the defect levels within the nickel oxide band gap. The band edge of the nickel oxide is not excited as the spectrometer laser is limited in energy to 2.61 eV, while the band gap

59

of nickel oxide as calculated from the absorbance spectrum is 3.22 eV. It can be noted that the spectrum consists of two prominent peaks at 570 nm and 790 nm that are convoluted together. It is due to emission from two different bands located within the band gap.

(a)   (b)
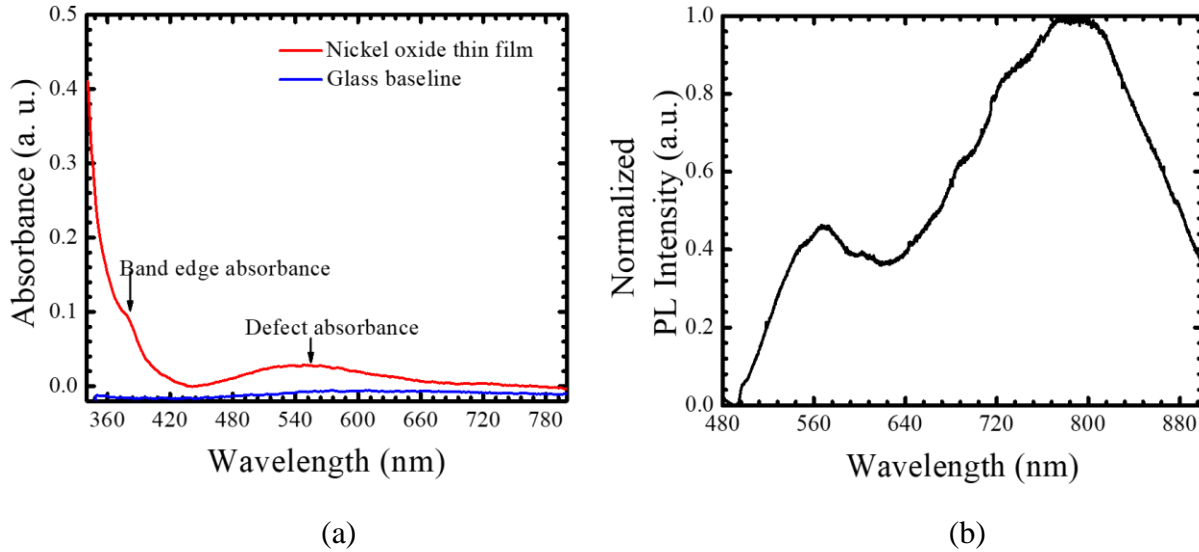
Figure 3.10. (a) The band gap of the nickel oxide thin film is extracted from the excitonic peak located at 385 nm of the absorbance spectrum. (b) The defect related photoluminescence spectrum of the nickel oxide thin film extends from 445 nm to 900 nm. Reprinted with permission from Vasan *et. al.* [50].

Since, the defects facilitate the transport of carriers across the QLED, it is important to characterize the defects by measuring the carrier lifetime using time resolved photoluminescence. The excitation is achieved by a 485 nm laser and so the band edge is not excited. Any carrier lifetime measured in this case is for the defect levels of nickel oxide thin film and not the band edge. Initially the nickel oxide samples were prepared on glass substrates and lifetime decay curve was measured. The decay curve is fitted with four exponential functions and this is shown in figure 3.11 (a). The fit is very good with very low residuals. The average lifetime is calculated as 1.31 ns. The short lifetime is understandable as the defect states are usually shorlived. In order to check the validity of this value, the same experiemnt was repeated on quartz substrate and this is shown in figure 3.11 (b). In this case the decay curve is

60

fitted with three exponential functions and the carrier lifetime is calculated as 1.97 ns. Within experiemntal errors this value is in good agrrement with the nickel oxide film on glass.

(a)   (b)
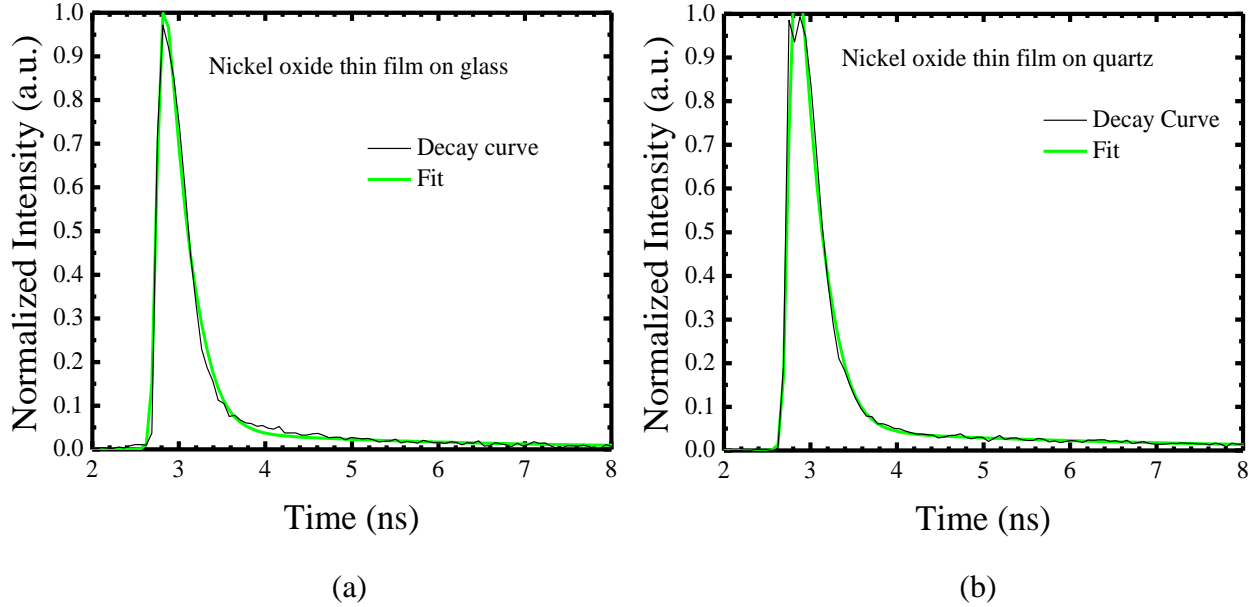
Figure 3.11. Average lifetime of nickel oxide defect states is calculated by fitting the decay curves measured on (a) glass and (b) quartz.

3.1.2.4. Electrical Properties

The non-stoichiometric nickel oxide grown using similar techniques is a p-type semiconductor. In order to determine this, a hot probe experiment is used to know the type of nickel oxide grown in this project. A schematic of the hot probe experiment is shown in figure 3.12. The probes of a voltmeter are made to contact the sample surface and the positive probe is heated using a soldering iron. The increased temperature generates majority carriers near the positive probe, which in this case are the holes. The excess holes start to diffuse towards the cold probe leaving behind negative charges at the hot probe. This separation of charges creates a voltage, which is read using the voltmeter. The voltage in this case has a negative value.
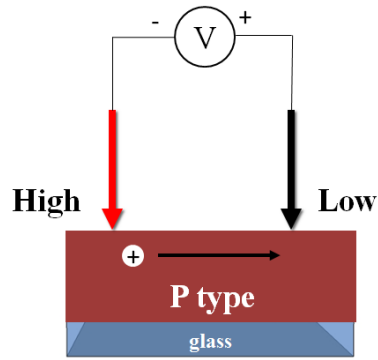
Figure 3.12. Schematic of the hot probe experiment to deduce the conduction type of nickel oxide thin film.

The mobility and band positions are extracted from the current-voltage characteristics an FTO/NiO/Al Schottky diode. From the hot probe experiment it is clear that the non-stoichiometric nickel oxide is a p-type semiconductor with holes as the majority carrier. The hole mobility is extracted from the current-voltage characteristics of the Schottky diode at room temperature. The current-voltage characteristic of the diode in log-log plot is shown in figure 3.13.
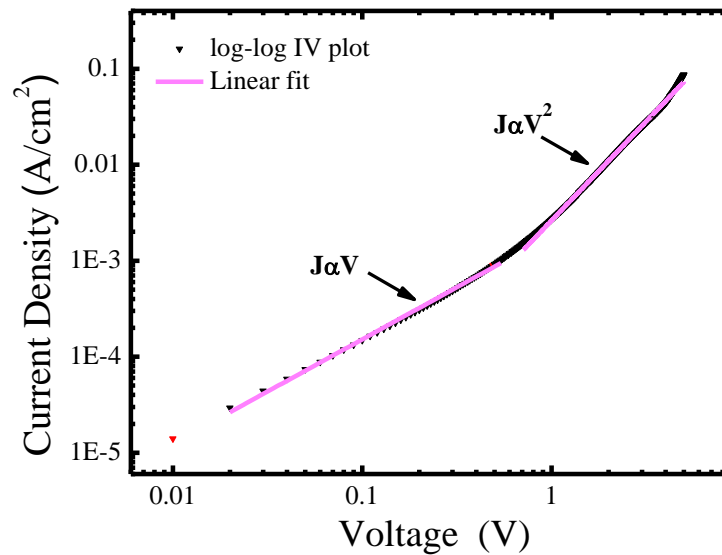
Figure 3.13. The log-log plot of the current-voltage characteristics of the nickel oxide Schottky diode is fitted with linear function to understand the conduction mechanism. Slope of 1 indicates an Ohmic conduction and a slope of 2 indicates a space charge limited conduction.

The plot is fitted with two linear fits with slopes ~1 and ~2. This is critical as the slopes give insights into the type of current conduction within the diode. Initially at low electric field, the current conduction is limited by the intrinsic carrier density and thermally generated carriers. For this diode the region between 0.1 V and 0.5 V yields a slope of ~1. This conduction regime is the Ohmic region where $J\alpha V^1$. As the voltage is increased further the diode enters the high field regime, where the current density follows the square law ($J\alpha V^2$). This conduction regime is called the space charge limited conduction [81, 82]. In this regime, the current conduction is dominated by the holes that are injected from the electrode. The current in this case is limited only the mobility of holes and not dependent on the hole density. Hence, mobility is calculated by fitting the current-voltage characteristics of the diode using the Mott-Gurney law given by equation 3.3 that describes the current in this regime [81, 82].

$$J_{SCLC} = \frac{9}{8} \, \varepsilon_0 \varepsilon_r \mu_h \frac{V^2}{d^3} \tag{3.3}$$

where, J_{SCLC} is the space charge limited current density, ε_0 is the permittivity of free space, ε_r is the dielectric constant of nickel oxide, μ_h is the hole mobility, V is the forward voltage and d is the thickness of the active layer. The current-voltage characteristics of the diode with the space charge limited current model fit are shown in figure 3.14. The fit is good with very low chi-square value. For fitting, the dielectric constant of nickel oxide is taken as 5.7 and the thickness of active layer as 300 nm. From this curve fitting the hole mobility is found to be, $\mu_h = 2.45 \times 10^{-4} \, cm^2V^{-1}s^{-1}$ with an error of $\pm 9.2 \times 10^{-7} \, cm^2V^{-1}s^{-1}$. This method is applicable when the conduction is unipolar and with an assumption that the mobility, dielectric constant are the same throughout the material.
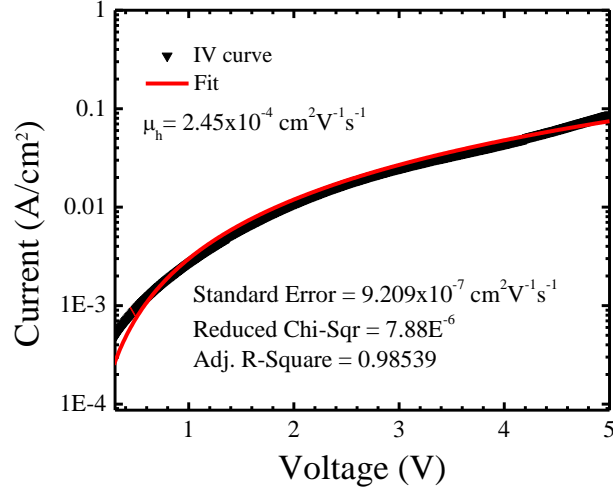
Figure 3.14. Space charge limited current model is fitted to current-voltage characteristics of a FTO/NiO/Al device to extract the hole mobility of the nickel oxide thin film. Reprinted with permission from Vasan *et. al.* [52].

The valence band and conduction band positions are calculated from the Schottky barrier height. The Schottky barrier height ϕ_B is calculated using two different methods for consistency. Cheung and Cheung came up with a method to calculate the barrier height and ideality factor which is the one of the methods used in this project [83]. According to this method the diode current is given by equation 3.4.

$$I = I_0 e^{\frac{q(V-IR_S)}{nkT}} \tag{3.4}$$

where, I is the forward current, I_0 is the saturation current, V is the forward voltage, T the temperature, k the Boltzmann constant, n the ideality factor and R_s is the series resistance of the device. The ideality factor is calculated using a plot of I vs dV/d(ln I) as shown in the equation 3.5.

$$\frac{dV}{d(\ln I)} = \frac{nkT}{q} + IR_s \tag{3.5}$$

The linear plot of dV/d(ln I) as a function of I is shown in figure 3.15. From the intercept of this plot, the ideality factor at room temperature is calculated as 13.6. The high ideality factor

indicates the non-ideal diode characteristics associated with bulk defects in the semiconductor

and interface states between Al and nickel oxide [84, 85]. To calculate the barrier height,

equation 3.6 and 3.7 are used.

$$H(I) = V - \frac{nkT}{q}\ln\left(\frac{I}{AA^*T^2}\right) \tag{3.6}$$

H(I) is a parameter calculated from the current-voltage characteristics and the plot of I vs H(I)

yields a linear plot as shown in figure 3.15. Also,

$$H(I) = n\phi_B + IR_s \tag{3.7}$$

Hence, from the intercept of the linear fit of I vs H(I) is equal to $n\phi_B$. Using n=13.6, the barrier

height is calculated as 0.40 eV.
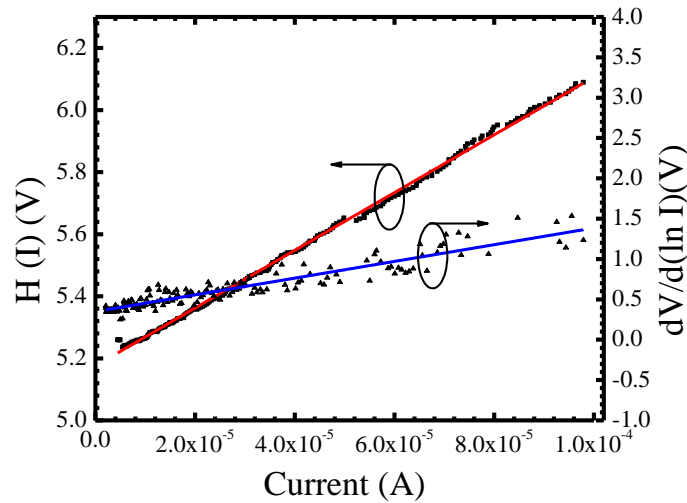
Figure 3.15. Cheung's method [83] is employed to extract the barrier height and ideality factor
of the Al/NiO Schottky diode.

In the second method, the current-voltage characteristic of the diode is measured at

different temperatures [86]. To extract the Schottky barrier height using this method, the diode

current-voltage characteristics are measured at 25°C, 50°C, 75°C, and 100°C. The packaged

diode is placed on a hot plate and the measurement is performed at these temperatures. The

current-voltage characteristics of the diode at different temperatures are shown in figure 3.16(a).

As seen in figure 3.16(a) the current is increasing with increasing temperature. For V>>4kT/q, the diode current can be expressed as equations 3.8.

$$J = A^*T^2 \exp\left(-\frac{q(\phi_B - V/n)}{kT}\right) \tag{3.8}$$

$$\ln(J/T^2) = \ln(A^*) - \frac{q(\phi_B - V/n)}{kT} \tag{3.9}$$

A plot of q/kT vs ln (J/T^2) is linearly fitted and the slope is extracted. Using the slope value, the barrier height is calculated using equation 3.10.

$$\text{Slope} = -(\phi_B - V/n) \tag{3.10}$$

This is repeated for two different voltages 4 and 5 V for consistency and are shown in figure 3.16(b). The barrier height is calculated as 0.38 eV for 4V and 0.42 eV for 5V. Using these two methods, the barrier height is calculated to be between 0.38 – 0.42 eV. For further calculations the average of this range, 0.40 eV is used as the barrier height.
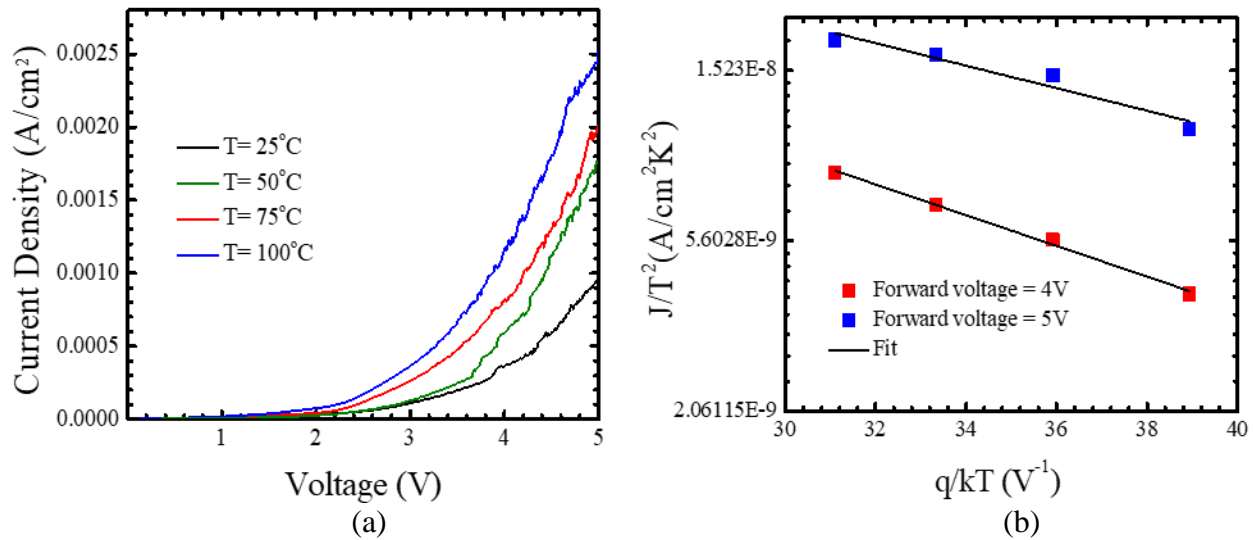
Figure 3.16. (a) The current-voltage characteristics of the diode is measured at 25, 50, 75, and 100 °C. (b) A plot of q/kT vs ln (J/T^2) at 4V and 5V are fitted linearly to calculate the barrier height using equation 3.10.

A schematic of the energy band diagram of Al/NiO Schottky diode is shown in figure 3.17. The band gap of the nickel oxide found using the absorbance spectrum is 3.22 eV and the work function of Al is 4.30 eV and finally the barrier height as calculated above is 0.40 eV.
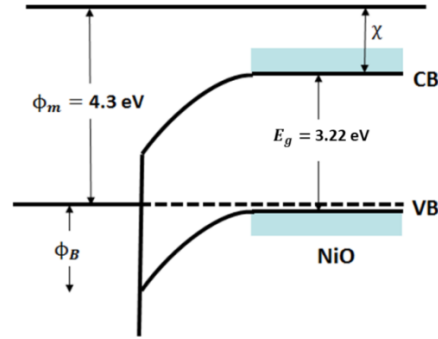
Figure 3.17. The energy band diagram of the nickel oxide Schottky diode is used to extract the CBM and VBM values of nickel oxide thin film.

Using these values, the electron affinity, χ, is calculated using equation

$$\Phi_b = E_g + \chi - \Phi_m$$

$$0.40 = 3.22 + \chi - 4.28$$

$$\chi = 1.46 \text{ eV}$$

The valence band position is then calculated as ~4.70 eV. The bandgap, electron affinity and the valence band maximum of nickel oxide obtained from the diode characteristics are lower than the reported results.

3.1.3. Nickel oxide nanoparticles

3.1.3.1. Structural and compositional properties

The structural and compositional properties of the nickel oxide nanoparticles are characterized by XRD, Raman and XPS measurements. The grazing angle XRD scan of the nickel oxide nanoparticle powder is shown in figure 3.17 (a). The diffracting planes (111), (200), (220), (311), and (222) located at 37.2°, 43.27°, 62.8°, 75.3°, and 79.3° respectively, are

characteristic of nickel oxide rock salt structure. The reference indices for bunsenite structure from JCPDS card no: 01-075-0197 are also marked in figure 3.18(a). The crystallite size, as calculated from Scherrer's equation, is 5 – 6 nm indicating that the formed nickel oxide is nanocrystalline. Nickel oxide thin films and nanoparticles reported so far are non-stoichiometric with nickel vacancies [62, 63, 80, 87]. Presence of these defects are identified by the shift in the diffraction peaks, specifically the (200) and (220) planes, when compared to stoichiometric nickel oxide or bunsenite [63]. The nickel oxide nanoparticles reported here are near-stoichiometric with fewer defects as the diffraction planes exactly align with the bunsenite reference indices. This can also be seen in the Raman spectrum of the nickel oxide nanoparticles shown in figure 3.18(b). The LO phonon mode at 510 cm^{-1} is characteristic of near-stoichiometric nickel oxide. This mode is shifted to 560 cm^{-1}, when the nickel oxide is formed in an oxygen rich environment leading to the formation of nickel vacancies, which makes the final nickel oxide non-stoichiometric [66].

(a)   (b)
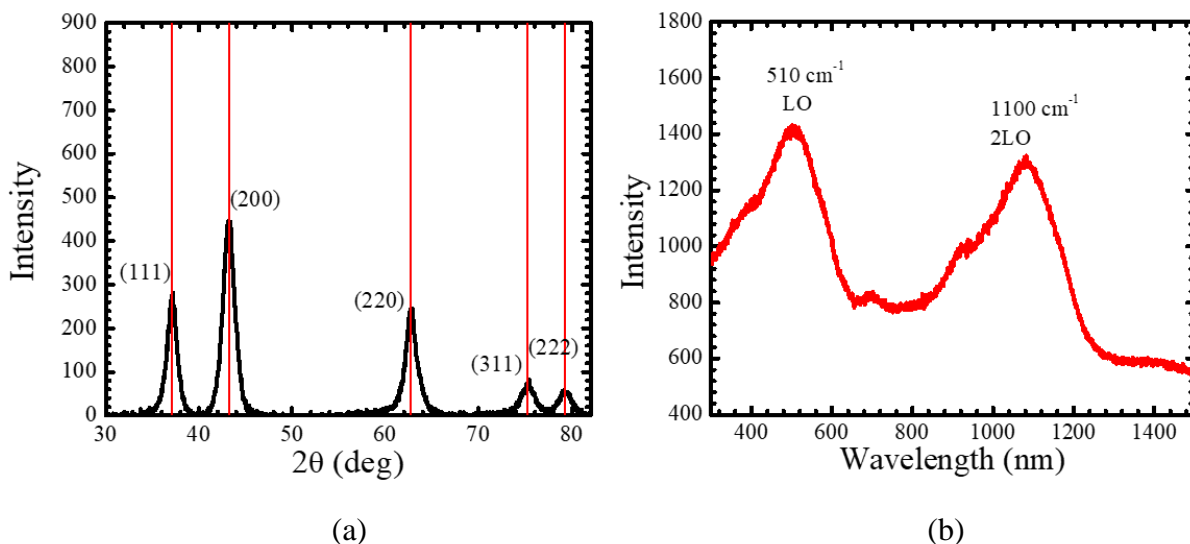
Figure 3.18. The (a) XRD and (b) Raman spectroscopy are used to structurally characterize the nickel oxide nanoparticles. Reprinted with permission from Vasan *et. al.* [70].

The composition of the nickel oxide nanoparticles is determined by XPS measurements. A survey of the material indicates the presence of nickel, oxygen and carbon. The carbon is from the nickel acetate, which is the precursor. The detailed XPS spectrum for the Ni2p3/2 state is shown in figure 3.19(a). The original spectrum is fitted with three Gaussian peaks. The peak centered at 854.2 eV binding energy corresponds to the Ni^{2+} oxidation state of Ni from stoichiometric nickel (II) oxide. The higher binding energy peak at 856.0 eV corresponds to the Ni^{3+} oxidation state, which is a result of non-stoichiometric nickel (III) oxide or nickel oxyhydride formed due to nickel vacancies [62, 63]. Finally, the peak at 861 eV is due to the shake up process [62]. Figure 3.19(b) shows the XPS spectrum O1s state. The peaks at 529.1 eV and 530.98 eV correspond to nickel (II) oxide and nickel (III) oxide or nickel oxyhydride respectively [62, 63]. The composition ratio of Ni^{2+} to Ni^{3+} is 1:1.7 as calculated from the integral area of the fitted peaks. The amount of Ni^{3+} formed due to nickel vacancies is much lower compared to nickel oxide thin film. Moreover, the atomic ratio of Ni:O in the nickel oxide nanoparticles is 1:1.18 indicating a near-stoichiometric nickel oxide.

(a)

(b)
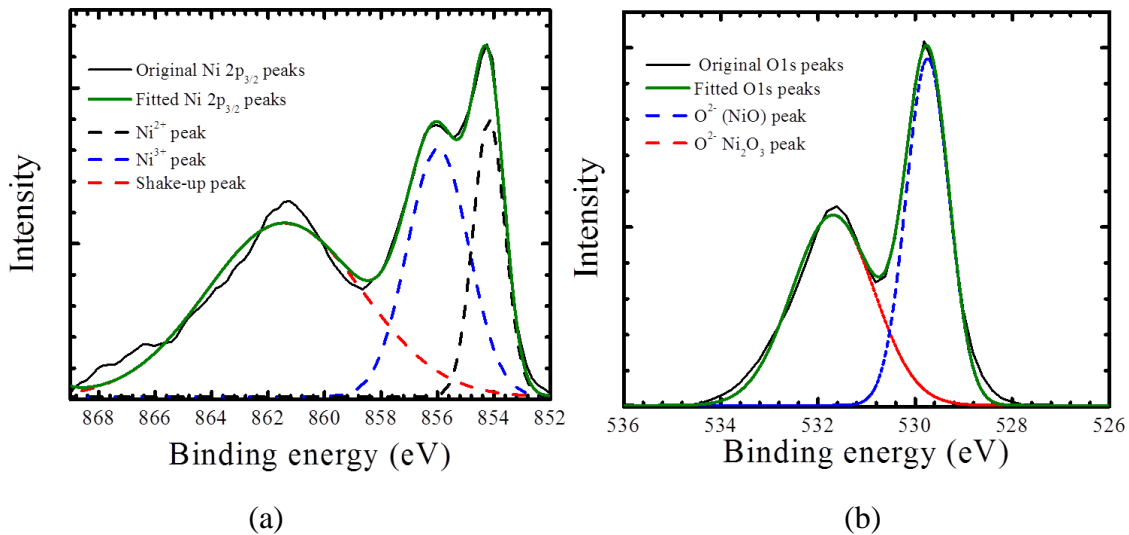
Figure 3.19. The composition of the nickel oxide HTL is measured from the (a) Ni peaks of Ni2p3/2 and (b) O peaks of O1s curves from the XPS. Reprinted with permission from Vasan *et. al.* [50].

From the structural and compositional properties investigated using XRD, Raman and XPS spectroscopies it is clear that the nickel oxide film used in this project non-stoichiomrtic with defects. The film is further characterized by investigating the optical properties.

3.1.3.2. Optical properties

The optical properties of nickel oxide nanoparticles and the quantum dots are investigated by measuring the absorbance. The absorbance of nickel oxide nanoparticles is shown in figure 3.20. The band gap of the synthesized near-stoichiometric nickel oxide nanoparticles as calculated from the excitonic peak at 280 nm is 4.42 eV. This band gap value is much higher than the band gap of non-stoichiometric nickel oxide thin film, which is around 3.22 eV. The photoluminescence measurements revealed no emission in the visible region as was seen with the nickel oxide thin film.
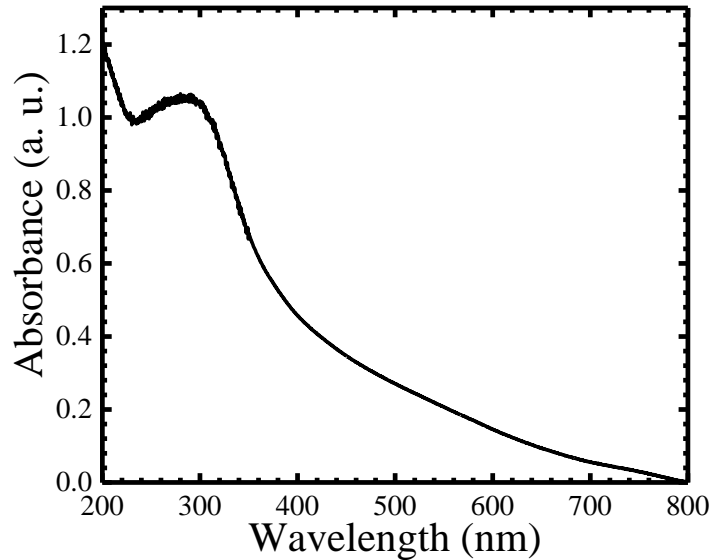
Figure 3.20. The band gap of the nickel oxide nanoparticles is calculated from the excitonic peak of the absorbance spectrum. Reprinted with permission from Vasan *et. al.* [70].

3.1.4. Zinc oxide nanoparticle

Properties of zinc oxide nanoparticles, used as the ETL in this project, is evaluated by structural, optical and electrical characterization techniques like XRD, Raman, absorbance, and photoluminescence and electron mobility measurement. Zinc oxide nanoparticles are not characterized as thoroughly as the nickel oxide HTL because it has been studied and reported extensively in literature [42-52]. Important properties critical to device operation such as crystallinity, bandgap and electron mobility are measured in this project.

3.1.4.1. Structural properties

Structural properties of zinc oxide nanoparticles are studied by measuring the XRD pattern and Raman spectroscopy. Figure 3.21 (a) shows the XRD pattern of zinc oxide nanoparticles dispersed in 1-butanol is drop cast from solution on glass substrates. The peaks at 38.16^o and 44.56^o are correspond to the (101) and (102) planes of crystalline zinc oxide [88]. The size of the nanoparticles as calculated using Scherrer's equation is ~20 nm. The quality of

(a)   (b)
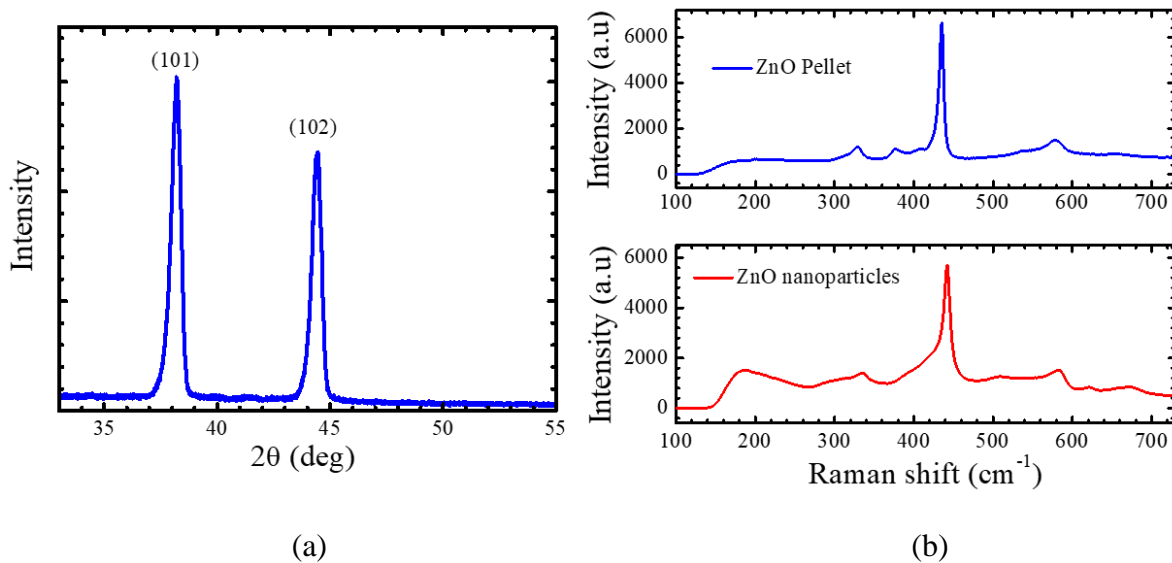
Figure 3.21. Structural properties of zinc oxide nanoparticles are investigated by measuring (a) XRD and (b) Raman spectroscopy. Reprinted with permission from Vasan *et. al.* [50].

the zinc oxide nanoparticles is also evaluated using Raman spectroscopy. Raman spectrum of

zinc oxide nanoparticles compared with the spectrum of commercially available zinc oxide

pellets (Kurt. J Lesker) are shown in figure 3.21(b). The peaks at 334 cm^{-1}, 441 cm^{-1}, and 582

cm^{-1} are characteristic of zinc oxide.

3.1.4.2. Optical properties

Optical properties of zinc oxide nanoparticles are studied using absorbance and

photoluminescence spectroscopies. The bandgap zinc oxide is calculated from the excitonic

peak shown in figure. The peak is at 334 nm, which corresponds to 3.71 eV. The normalized

photoluminescence spectrum of the zinc oxide nanoparticle is shown in figure 3.22. The small

peak at 355 nm corresponds to the excitation laser and the peak at 365 nm corresponds to the

band edge emission of zinc oxide nanoparticles. The FWHM of the spectrum is 32 nm

indicating that the nanoparticle sizes are uniformly distributed.
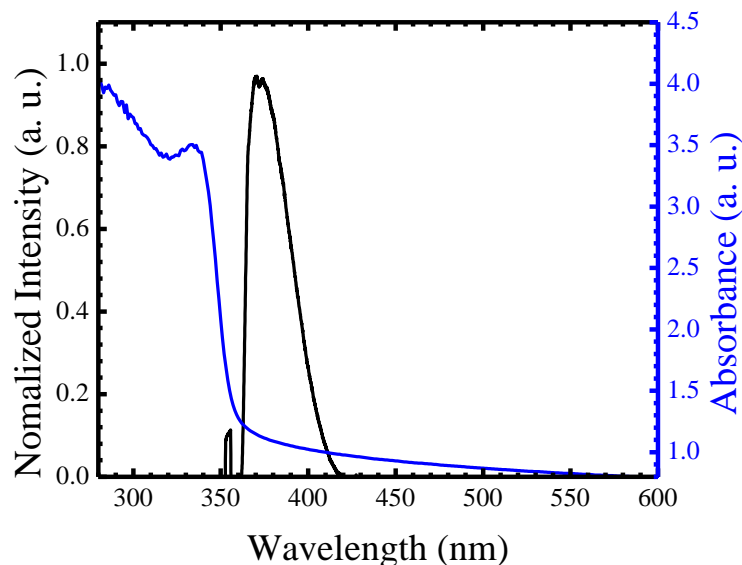
Figure 3.22. The absorbance and photoluminescence spectra of the zinc oxide ETL that was
synthesized by hydrolysis of Zinc precursor using ammonium hydroxide. Reprinted with
permission from Vasan *et. al.* [50].

3.1.4.3. Electrical properties

Zinc oxide nanoparticles are intrinsically n-type due to inherent defects. Mobility is one of the electrical parameters that changes with the synthesis procedure and hence it should be measured. In this project, the mobility is measured by fabricating a thin film transistor with the nanoparticles in the channel. The gate-source voltage, V_{GS} is swept from 0-20 V with constant drain-source voltage, V_{DS} and corresponding drain-source current, I_{DS} is measured. The V_{GS} vs I_{DS} for different V_{DS} are plotted in figures 3.23(a). As seen in figure 3.23(a), the threshold voltage is ~4V and with increasing V_{DS}, the drain current increases. For $V_{DS} > (V_{GS}-V_T)$ the device enters saturation regime in which the drain current is no longer a function of V_{DS}. In the saturation region, the mobility of the channel material is calculated from the slope of the transfer characteristics, V_{GS} vs $(I_{DS})^{1/2}$. From the slope of V_{GS} vs $(I_{DS})^{1/2}$ shown in figure 3.23(b), the electron mobility is calculated as 1.24×10^{-2} cm^{2}V^{-1}s^{-1}.

(a)   (b)
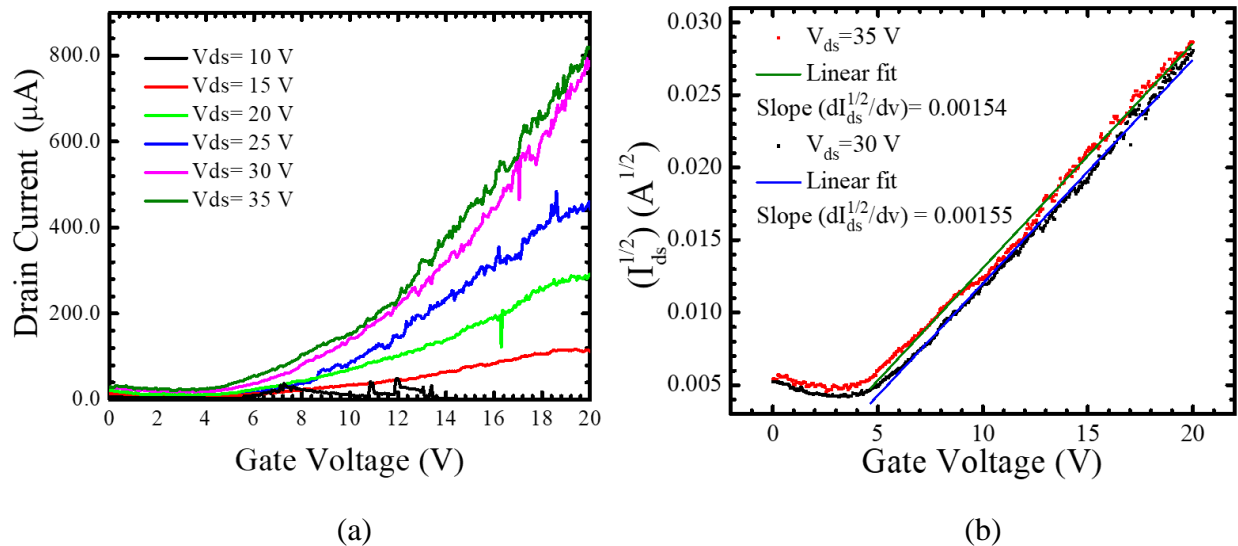
Figure 3.23. (a) The gate-source voltage of the thin film transistor is swept, and corresponding drain current is measured for different drain-source voltages. (b) A plot of V_{GS} vs $(I_{DS})^{1/2}$ in the saturation region of the thin film transistor yields a linear curve. This is linearly fitted to extract the electron mobility of zinc oxide nanoparticles. Reprinted with permission from Vasan *et. al.* [52].

3.2. Charge transport model

To make an efficient QLED, it is important to improve the charge transport efficiency into the quantum dot emissive layer. Zinc oxide nanoparticles commonly used for electron transport has a CBM aligned very well the CB of the quantum dots. It is widely accepted that the zinc oxide nanoparticles facilitate efficient electron transport by direct charge injection mechanism [42-52]. So, the transport efficiency is limited by the hole transport to the emissive layer. The nickel oxide thin film and nanoparticles in this project are designed such that they facilitate hole transport by resonant energy transfer and direct charge injection mechanism, respectively. In this section the charge transport between HTLs and quantum dot emissive layer is evaluated and modelled.

3.2.1. Resonant energy transfer in nickel oxide thin film-quantum dot bilayer

The charge transport between non-stoichiometric nickel oxide thin film and quanutm dot emissive layer is investigated on a nickel oxide-quanutm dot bilayer. Time resolved photoluminescence, photoluminescence, and absorbance measurements are used to study the carrier dynamics in the bilayer samples. For energy transfer to occur from nickel oxide HTL to quanutm dot layer, energitically resonant states are required and the layers need to be in close contact. The layers are in close proximity as the quanutm dots are spin coated directly onto the nickel oxide HTL. The bandgap of nickel oxide is 3.22 eV, which is well over the bandgaps of visible light emitting quanutm dots. So any form of resonant energy transfer between the band edge states are ruled out. As established from the structural, optical and electrical properties, the nickel oxide thin film is non-stoichiometric with nickel vacnacies. These vacnacies lead to the formation of defect states within the bandgap of nickel oxide. These defect states are involved in

74

radiative recombination with lifetimes of 1-2 ns leading to visible emission. Since, the defect

emission is in the visible region, some of these states are in resonance with the qunatum dot band

edge. This is quantified by measring the overlap integral of the quantum dot absorbance

spectrum with the emission spectrum of the nickel oxide defect states. As the quanutm dot size

increases conversely when the band gap decreases, the overlap of the quantum dot absorbance

spectrum with the nickel oxide defect emission increases. It is evident from the figure 3.23 that

the blue quanutm dots overlap the least while the red quanutm dots overlap the most with the

nickel oxide emission spectrum. Thus, if resonant energy transfer from the nickel oxide defects

is an important mechanism, it is expected that the efficiency to the red quantum dots will be

much higher than to the blue quantum dots. If there exists a resonant energy transfer from nickel

oxide donor to quantum dots acceptor, then the lifetime of quantum dot acceptor should be

longer in the bilayer samples when compared to stand alone quanutm dots.
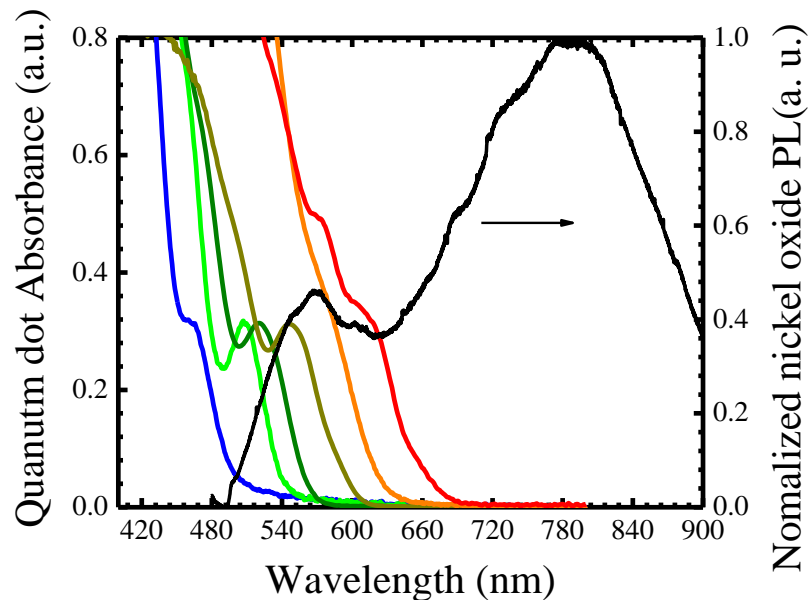
Figure 3.24. The defect related emission spectrum of the nickel oxide thin film extends from 445 nm to 900 nm. The absorbance spectra of different CdSe/ZnS quantum dots overlap with the defect related emission spectrum of nickel oxide HTL and the area of overlap increases as their size increases.

The fluorescence lifetimes of six different quantum dot sizes in the form of films are measured both on bare glass and nickel oxide films. The fluorescence decay curves of quantum dots on glass and on nickel oxide are plotted in figure 3.25(a) to (f). It is clear from these plots that the lifetime of quantum dots changes on nickel oxide HTL. The change shows a pattern where the lifetime quenches on blue quantum dots and elongates on cyan, green, yellow, orange and red quantum dots. Moreover, the elongation increases as the size of the quantum dots
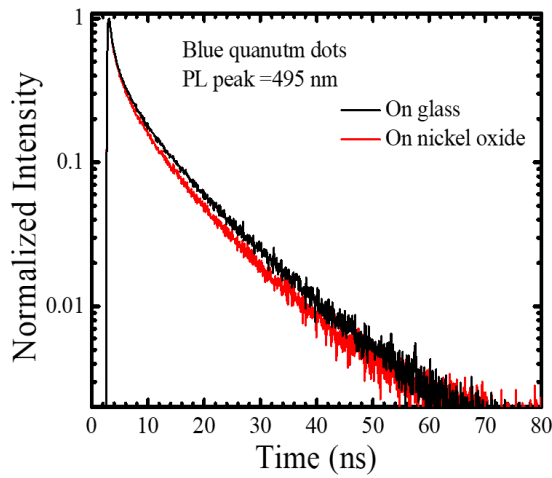
(a)
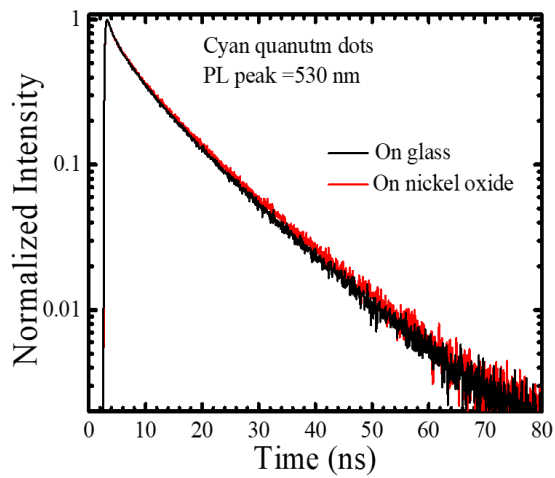
(b)
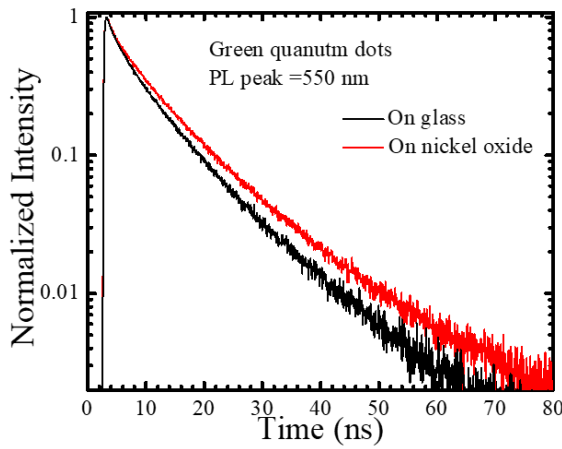
(c)
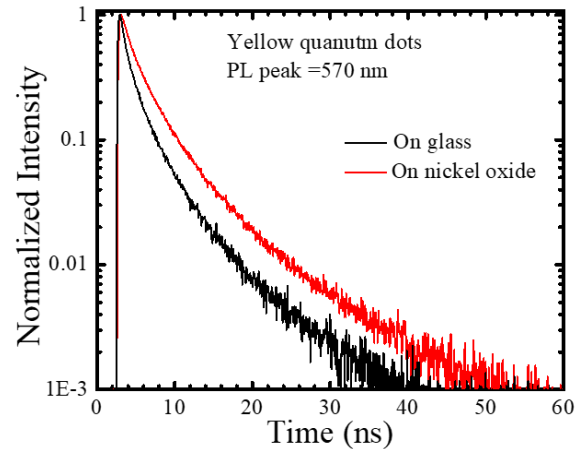
(d)
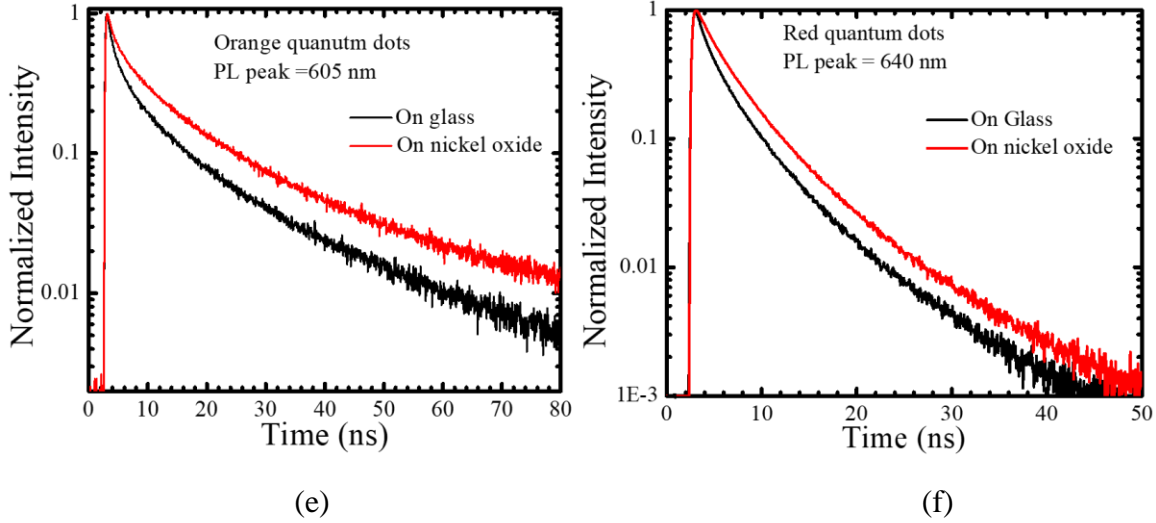
Figure 3.25. Lifetime decay curves of alloyed quantum dots that are measured as a spin coated film on glass and nickel oxide thin film.

increases. The lifetime decay curves are fitted with four exponentials, which is the minimum

number needed as determined from the residuals, consistent with previous studies. The average

lifetime is then calculated the equation 3.1. The laser was focused onto several positions on each

sample and the mean value and standard deviation from each τ_{avg} from each point are calculated

to obtain the $\tau_{sample-mean}$ of that sample. The mean and standard deviation of quantum dot

lifetimes measured at several positions on glass and on nickel oxide are shown in figure 3.26. It
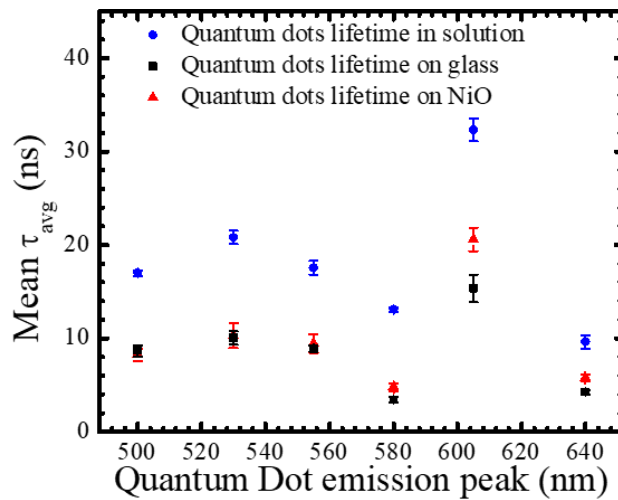
Figure 3.26. The mean and standard deivation of the average lifetimes of quantum dots measured at different spots in solution, on glass and on nickel oxide thin film.

can be noted that the lifetime of the respective quantum dots in solution is much higher than that of the film on both bare glass and on the nickel oxide film. It is known that quantum dot lifetime is quenched when formed in to a film due to self-quenching effects [53]. In order to explore this further the percentage of lifetime qurenching on glass and nickel oxide are calculated for all quanutm dots. Figure 3.27 shows the percentage lifetime quenching on bare glass and nickel oxide relative to those in solution as a function of quanutm dot size. It can be noted that the lifetime of quanutm dots quenches by approximately 52% on bare glass regardless of the size of the quanutm dot. On the other hand, the lifetime quenching of quanutm dots on nickel oxide shows strong size dependence. The percent quenching decreases as the size of the quanutm dots increases. While the lifetime of blue-emitting quantum dots on nickel oxide quench by ~52%, similar to that on bare glass, the lifetime of red-emitting quantum dots quench by only ~36% on nickel oxide. This shows that there is a strong interaction between the nickel oxide and the quantum dots and that this interaction is dependent on the bandgap of the quanutm dot. To
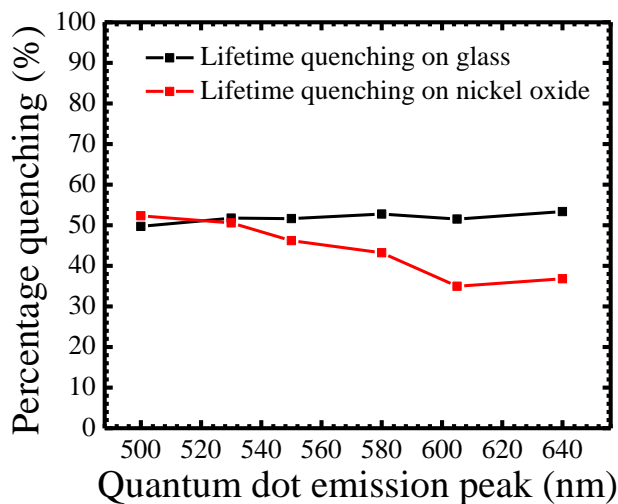
Figure 3.27. The percentage quenching of quantum dot lifetime on nickel oxide and glass are plotted as a function of emission wavelength. In this the lifetime of quantum dots in hexane is considered as the control sample or reference.

quantify this, the difference between the average quanutm dot lifetime on nickel oxide ($\tau_{NiO\text{-}avg}$) and on bare glass substrates ($\tau_{glass\text{-}avg}$) is plotted as a function of quantum dot emission wavelength. The quantum dot lifetime difference, $\Delta\tau$, is given by, $\Delta\tau = \tau_{NiO\text{-}avg} - \tau_{glass\text{-}avg}$. It can be seen from figure 3.28(a), that the lifetime of quanutm dots on nickel oxide is elongated. The elongation of quantum dot lifetime on nickel oxide can be atrributed to energy transfer from the defect states of nickel oxide into the quantum dot film. A similar effect is reported by Franzl *et al.* in CdTe films, which was attributed to a feeding effect from the smaller to larger quantum dots [89]. The photoluminescence intensities of the quantum dot film in the bilayer and the quantum dot film on glass are also measured for different quantum dot sizes. This is shown in figure 3.28(b). It is clear that the photoluminescence intensity of quantum dots in the bilayer is higher than that on glass. While, the photoluminescence intensity is increased by more than 50% for the orange and red quantum dots, the increase in photoluminescence intensity for blue quantum dots is <1%, further supporting that a size-dependent energy transfer from the nickel oxide to the quantum dots results in higher photoluminescence intensity.

(a)   (b)
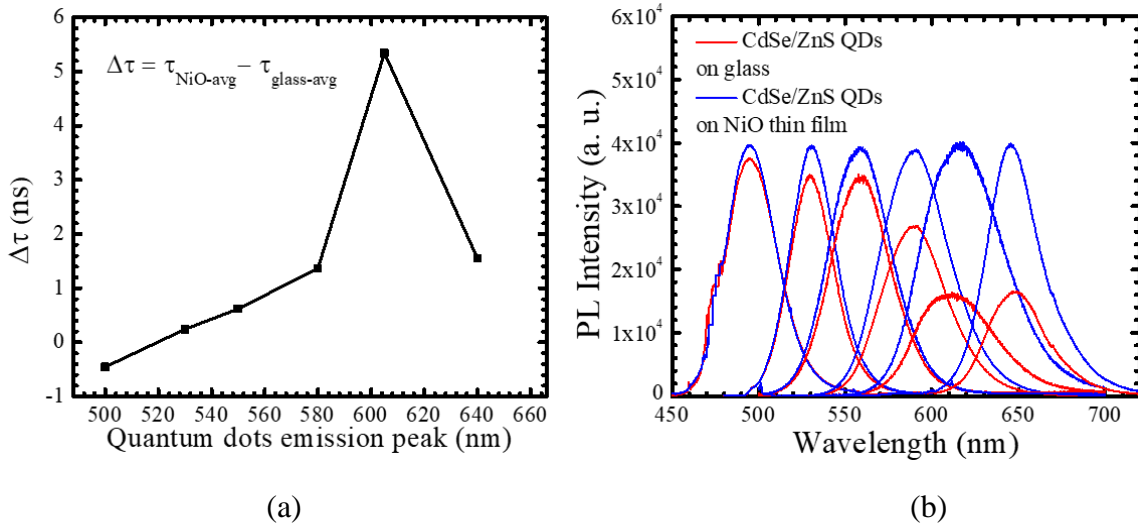
Figure 3.28. (a) The difference in average lifetime of quantum dots on nickel oxide and glass are plotted as a function of quantum dot emission. (b) As a result of increased lifetime, the quantum dots exhibit an increased photoluminescence intensity on nickel oxide.

Even though the above results indicate the existence of energy transfer from nickel oxide HTL to quanutm dots, it is ncessary to quantify the energy transfer time. It can be noted that the elongation of quanutm dot lifetimes on nickel oxide is due to the delayed photoluminescence after energy transfer. More detailed analysis of the energy transfer dynamics is performed by subtracting the photoluminescence decay curve of the quantum dot film on glass from that of the bilayer as a function of size. The data are normalized by aligning the data point at which the rise begins so that the subtraction did not result in a negative intensity. The subtraction removes the decay due to the direct excitation of the quantum dot by the laser, thus extracting the time-dependent intensity rise due to the energy transfer from the nickel oxide to the quantum dot, and is shown in figure 3.29. The points are the data and the solid lines are exponential fits with the color signifying the emission color (cyan, green, yellow, orange, and red). Both the maximum
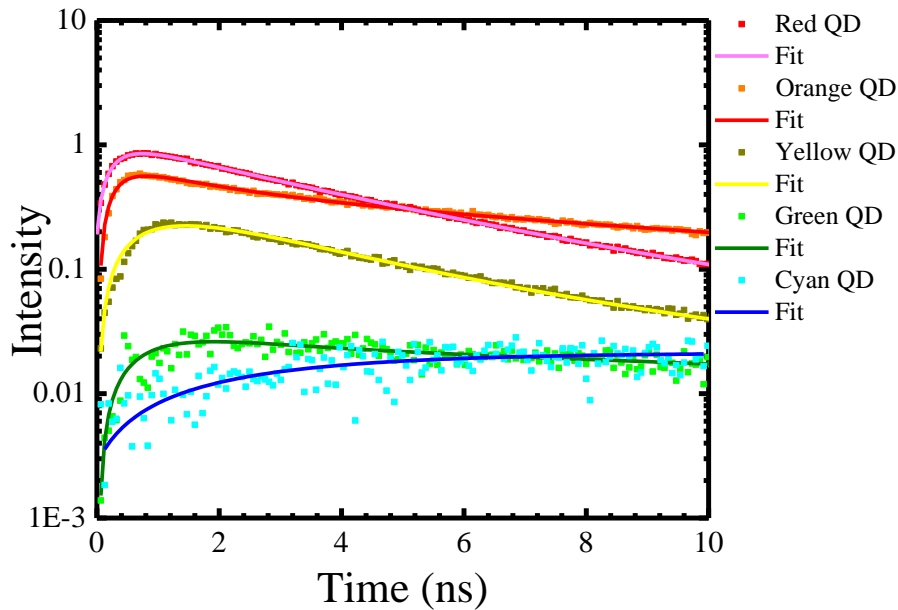
Figure 3.29. Energy transfer curve is obtained by subtracting the photoluminescence decay of quantum dot film on glass from the bilayer sample. The pure energy transfer curve is fitted with an exponential function and the energy transfer time is extracted. The scatter points are the actual energy transfer curve and solid lines are the exponential fits.

intensity and the transfer rate increased as a function of size, and thus spectral overlap integral. There is a negligible energy transfer for the blue quantum dots, the cyan quantum dots have a rise time of approximately 2.9 ns, the green quantum dots have 0.93 ns, the yellow quantum dots have a 0.75 ns rise time, the orange quantum dots have a 0.26 ns rise time, and the red quantum dots have a 0.28 ns rise time. With comparable energy transfer time, the tranfer rate to orange and red quantum dots are comparable $\sim 3.6 \times 10^9 \, s^{-1}$. Previous studies on multilayer quantum dot films have shown similar or faster energy transfer times [90-92].

Previous transport models involving all-inorganic bilayers have been based on the relative energy alignment of the nickel oxide HTL and the valence band of the quantum dot. In this project, an alternate transport model is proposed based on the structural and spectroscopic properties of the nickel oxide layer and the quantum dot size. The nickel oxide film is designed in this project to be highly non-stoichiometric in order to provide enough defect states that are in resonance with the quantum dot band gap. The defect states within the band gap of the nickel oxide are in resonance with the band gap of the larger quantum dots, but not so for smaller quantum dots. Figure 3.28(a) shows that there is an overall increase in the lifetime with quantum dot size following energy transfer from nickel oxide relative to direct excitation of the quantum dots alone (i.e. without energy transfer from nickel oxide), as expected from the increased energy transfer efficiency. However, the increase in quantum dot lifetime (up to 5.5 ns for the orange quantum dots) is more than an order of magnitude longer than the energy transfer time. This suggests that quantum dot states that are populated from energy transfer from nickel oxide to the quantum dot are longer lived, on average, than those populated via direct excitation of the quantum dot. Figure 3.10(a) shows that there are two broad emission bands from nickel oxide, one centered around 570nm and the other centered around 790 nm. There are likely a number of

81

trap states in the shell and/or at the core/shell interface that are slightly below the band edge

states and could play a role in the energy transfer and decay dynamics. Direct excitation of the

quantum dots is accomplished by a 485 nm laser, which excites the quantum dots above the band

gap energy – especially the orange and red quantum dots. Due to the absolute energies of the

nickel oxide and quantum dot valence band edges, there is a negligible possibility of direct hole

injection, and thus energy transfer from nickel oxide defect states to quantum dots dominates.

The fact that the broad 570 nm band from the defect nickel oxide states is so close to the band

gap for the orange quantum dots could suggest that some of the trap states in the quantum dots

are directly populated through the energy transfer process, especially from the red edge of the

570 nm band. Trap states generally show longer lifetimes than band edge states [73] and is one

possible explanation of why the fluorescence lifetime of the quantum dot/ nickel oxide bilayer

structures show up to 5.5 ns longer fluorescence decay lifetimes than the quantum dot

monolayers, even though the energy transfer time is sub-ns

A photoluminescence intensity decay is commonly encountered in bilayers where the

valence band of the transport layer aligns with the valence band of the quantum dots that

facilitates efficient charge injection [70]. For example, Wang *et al* reported a decreased

photoluminescence intensity of perovskite material on a HTL and attributed it to the efficient

charge transport between the two layers by charge injection mechanism [87]. On the other hand,

an increase in the photoluminescence intensity is commonly associated with energy transfer

mechanism [93]. The increase in the steady-state photoluminescence intensity of the quantum

dots in the bilayer (figure 3.28(b)) and that observed by removing the direct quantum dot

excitation contribution in the time-resolved photoluminescence intensity (figure 3.29) are thus in

agreement with this proposed energy transfer mechanism.

3.2.2. Charge injection

The charge transport between the near-stoichiometric nickel oxide nanoparticle HTL and the quantum dots is investigated by time-resolved photoluminescence measurements. The lifetime of blue, cyan and orange quantum dots are measured in hexane and in solution mixed with equal amount of nickel oxide nanoparticles. The average lifetimes of blue, cyan and orange quantum dots in hexane are 17.01 ns, 20.82 ns and 31.67 ns, respectively. These are obtained by fitting the results shown in figure 3.30 with three exponential decay functions and average lifetimes are calculated using equation 3.1. It can be noted that the lifetimes of quantum dots when mixed with nickel oxide nanoparticles are quenched significantly and that the quenching is dependent on the size of the quantum dot. The lifetime of blue quantum dots quench the highest, followed by cyan and orange quantum dots. Normally, quantum dot lifetime quenching is encountered in quantum dot films due to self-quenching effects. In this case, the quantum dots are still well dispersed in hexane and the lifetime quenching can be attributed to efficient hole transport from the quantum dots into the nickel oxide nanoparticles.

(a)

(b)
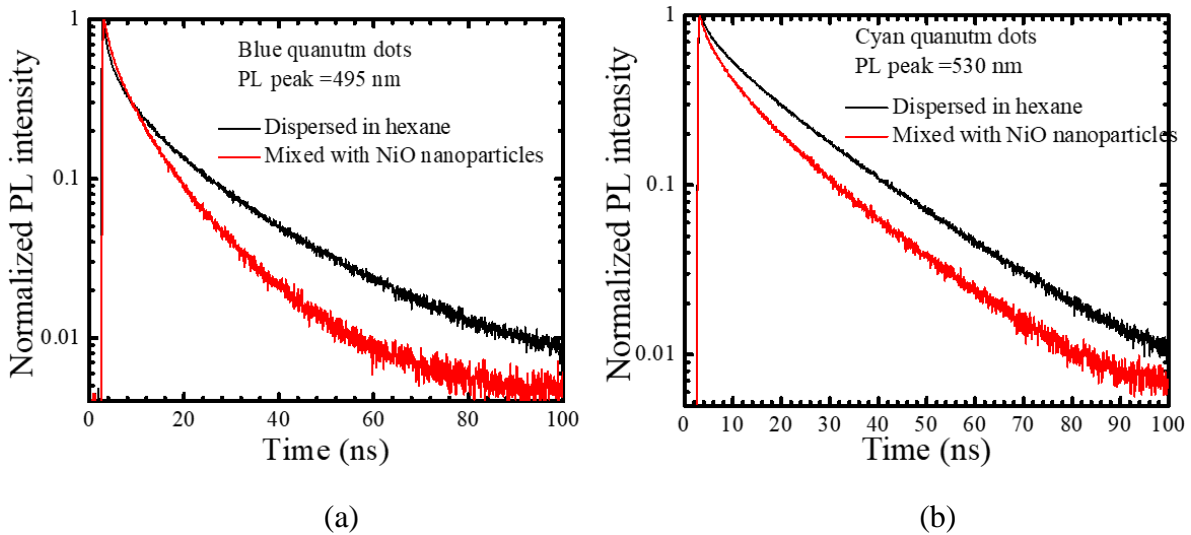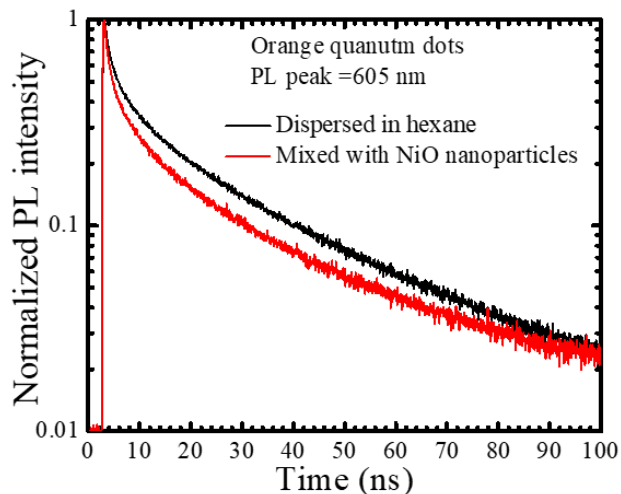
(c)

Figure 3.30. The lifetime of (a) blue, (b) cyan and (c) orange CdSe/ZnS quantum dots shortened when mixed with the nickel oxide nanoparticles, which indicates an efficient charge transport between the two materials. Reprinted with permission from Vasan *et. al.* [70].

The study shows that the quantum dots exhibit a strong interaction with the nickel oxide nanoparticle powder. The nickel oxide nanoparticles reported here are near-stoichiometric with a wide band gap of ~4.4 eV and a deep valence band maximum at -6.22 eV. The valence band value is calculated from the reported electron affinity value for nickel oxide. It can be seen that the lifetime of quantum dots is quenched significantly when mixed with the nickel oxide nanoparticles. Also, lifetime quenching increases with an increase in the band gap of the quantum dots. In other words, quenching is dependent on the relative valence band alignment of the quantum dots with nickel oxide nanoparticles. The valence band of blue quantum dots aligns well with the nickel oxide nanoparticles, leading to 41% quenching in lifetime. The cyan and orange quantum dots exhibit lower quenching because of the high barrier to holes in these quantum dots. This is schematically represented in figure 3.31. In contrast, Zheng *et.al* reported lifetime quenching decrease with an increase in the bandgap of the quantum dot [12]. The opposite trend reported here could be due to the deeper valence band maximum of the nickel oxide nanoparticles, at -6.22 eV, as compared to -5.04 eV reported by Zheng *et. al* [94]. In a

84

QLED device the barrier to holes injected into the blue quantum dots is much lower when the

nickel oxide nanoparticles are used as HTL. It is clear from figure 3.31 that for other smaller

band gap quantum dots, the barrier to hole injections into the quantum dots is even lower or non-

existent. So far, the reported inorganic HTLs for QLED devices provide a very high barrier to

quantum dots, thus reducing the efficiency.   On the other hand, nickel oxide nanoparticles with a

deeper valence band maximum are a potential HTL that can inject holes into the quantum dots of

different sizes more efficiently.
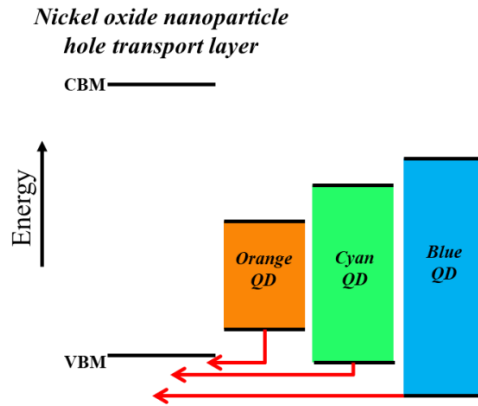
Figure 3.31. Schematic of the charge transport between blue, cyan, and orange quantum dots
and the nickel oxide nanoparticle HTL. Reprinted with permission from Vasan *et. al.* [70].

3.3. QLED device results

3.3.1. All-inorganic QLED with nickel oxide thin film HTL

3.3.1.1. Green emitting QLED

The performance of QLED is evaluated by measuring the current-voltage characteristics

and light output characteristics. The band alignment of different device layers is shown in figure

3.32. The valence and conduction band positions of zinc oxide and quantum dot emissive layers

are taken from literature [52]. The work function of FTO anode is reported to be 4.6-4.8 eV and

that of Al cathode is 4.28 eV [95, 96]. Hence, there is a ~ 0.2 eV barrier for electron injection at the Al-ZnO interface and negligible barrier for hole injection at the FTO-nickel oxide interface. The barrier to charge injection at the nickel oxide-quantum dot interface is ~1.90 eV, while there is no barrier at the ZnO–quantum dot interface.
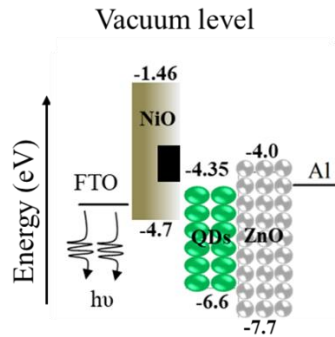
Figure 3.32. The valence and conduction band values (in eV) of the different device layers formed by spin coating are shown for the green QLED. Reprinted with permission from Vasan *et. al.* [52].

The device is forward biased in step of 1V staring from 0V. The device turns on at 5V and the emission intensity increased with increase in bias voltage. The device operating at different bias voltages are shown in figure 3.33. The electroluminescence spectrum is recorded at each bias voltage after 5V till 11V at which the emission starts to saturate. The normalized photoluminescence spectrum of quantum dots on glass and electroluminescence spectrum of the device at 10V are plotted in figure 3.34(a). As seen, the photoluminescence peak is at 553 nm and the electroluminescence peak is at 555 nm. The FWHM of the electroluminescence spectrum is 42 nm indicating a saturated, pure green color emission. The electroluminescence spectra at different bias voltages are plotted in figure 3.34(b). The intensity at 5.0V is very low compared to higher voltage intensities and so it is shown in the inset of figure. The output intensity increases as the forward voltage is increased and saturates after 10V.
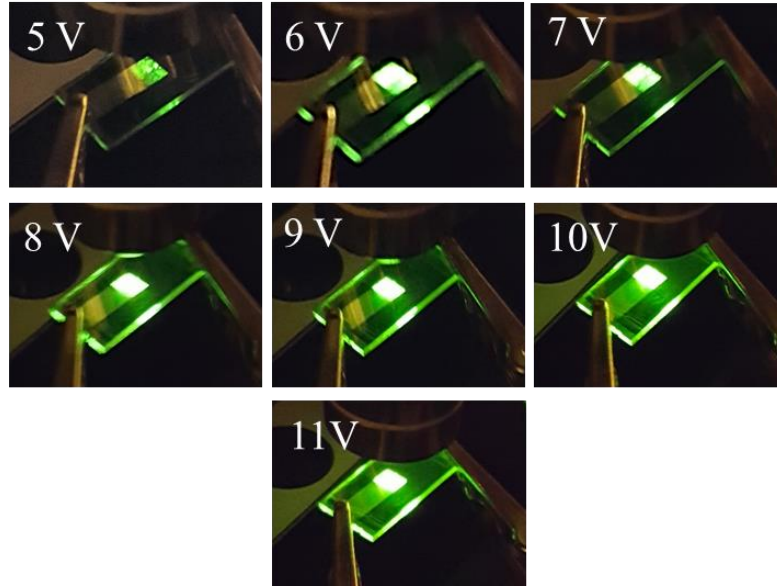
Figure 3.33. Electroluminescence of the green QLED operating at different bias voltages are shown.

(a)   (b)

Figure 3.34. The photoluminescence spectrum of the green quantum dots is compared to that of the green QLED electroluminescence spectrum(b) Highly saturated, pure color electroluminescence of the device at different bias voltages. Reprinted with permission from Vasan *et. al.* [52].

The IV characteristics of the device are shown in figure 3.35. In order to understand the working of the device, the IV curve is plotted in log-log scale in which the plot exhibits different slopes depending on the type of current conduction mechanism. The IV curve exhibits three distinct slopes, corresponding to Ohmic, trap limited and space charge limited conduction

regions [36, 81]. In region I from 0.0 to 4.65V, the slope is 1.2 and hence JαV$^{1.2}$, which is very

close to an Ohmic behavior. Ohmic current is due to the mobile carriers in the device more

specifically electrons in conduction band or holes in the valence band and is directly proportional

to the applied voltage. The current density increases with a much steeper slope of 4.0 in region

II between 4.65 and 6.25V, which corresponds to trap limited conduction. In this region, the

injected carriers are trapped at the traps on the emissive layer and the interface traps in the CTLs.

At 4.65V the slope changes and this is considered as the onset of charge injection into the

quantum dots [36]. But the turn-on voltage is considered as 5V at which the emission is high

enough to be detected. Finally, the slope of region III between 6.25 and 11V is 2.0, which is the

space charge limited conduction. In this region, the traps are completely filled, and the current is

limited by the space charge created in the device. Trap filled space charge limited current is

usually expressed using Mott-Gurney law given by equation 3.3. Here the current density and

forward voltage have a quadratic relationship and the conduction is dependent on the mobility.
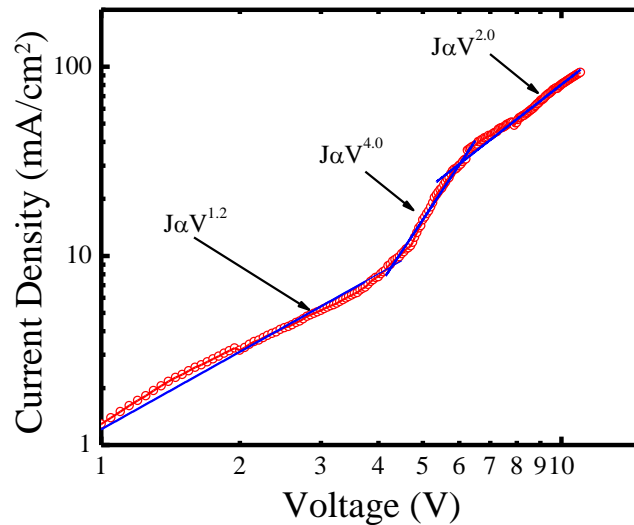
Figure 3.35. The three current conduction regions of the device correspond to the different slopes in the current-voltage characteristics. Reprinted with permission from Vasan *et. al.* [52].

The light output characteristics of the device are shown in figure 3.36, which are

calculated assuming a Lambertian emission [97, 98]. In figure 3.36(a), the luminance of the

device is plotted as a function of bias voltage. The voltage at which the device luminance

reaches 1000 cd/m^2 is 5.4 V and corresponding current density is 21 mA/cm^2. Another 20

mA/cm^2 increase in current density increased the luminance to 10,000 cd/m^2 at 6.9 V. The

current and external quantum efficiencies of the device, plotted as a function of current density,

are shown in figure 3.36(b). The current efficiency increases initially, reaches a maximum at

10V, and starts to decrease after. The maximum current efficiency of 144 cd/A is obtained at 80

mA/cm2 current density. The EQE shows a similar profile as previously reported for hybrid

QLED and perovskite based solution processed LEDs [9, 19]. The EQE reaches a maximum of

11.4% at 80 mA/cm^2 and decreases with further increase in the current density. The luminous

efficiency of the device reaches a peak of 45.3 lm/W and starts to decrease with further increase

in current density. The efficiency roll-off or droop after reaching a peak is due to charging of

quantum dots. At high current densities the quantum dots are charged due to influx of carriers.

These charged quantum dots are rendered non-emissive faster than the radiative recombination

rate as a result of Auger recombination, which leads to efficiency roll-off [36, 53, 99]. Auger

recombination rate is on the order of few ps, while the average radiative lifetime of green

quantum dots is ~19 ns.

(a)   (b)

Figure 3.36. (a) Luminance of the device is plotted as a function of the bias voltage. The luminance increases with voltage and saturates at 10V. (b) The current efficiency and EQE are plotted as a function of current density. Reprinted with permission from Vasan *et. al.* [52].

3.3.1.2. Yellow emitting QLED

Yellow emitting QLEDs are fabricated using the 570 nm emitting CdSe/ZnS quantum dots. The band alignment of different device layers is shown in figure 3.37. The band positions of the CTLs and the work functions of electrodes are the same as shown in figure 3.32. The band positions of the yellow emitting quantum dots are different than the green quantum dots. The barrier to charge injection at the nickel oxide-quantum dot interface is ~1.83 eV, while there is no barrier at the ZnO–quantum dot interface.

Figure 3.37. The valence and conduction band values (in eV) of the different device layers formed by spin coating are shown for the yellow QLED.

90

The device is forward biased in step of 1V staring from 0V. The device turns on at 5V

and the emission intensity increased with increase in bias voltage. The device operating at 10V

bias voltage is shown in figure 3.38(a). The normalized photoluminescence spectrum of

quantum dots on glass and electroluminescence spectrum of the device at 10V are plotted in

figure 3.38(b). As seen, the photoluminescence peak is at 570 nm and the electroluminescence

peak is at 588 nm. The FWHM of the electroluminescence spectrum is 38 nm indicating a

saturated, sodium yellow color emission. The electroluminescence spectra at different bias

voltages are plotted in figure 3.38(c). The intensity at 5.0V is very low compared to higher

voltage intensities and so it is shown in the inset of figure. The output intensity increases as the

forward voltage is increased and saturates after 8V.
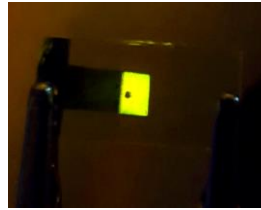
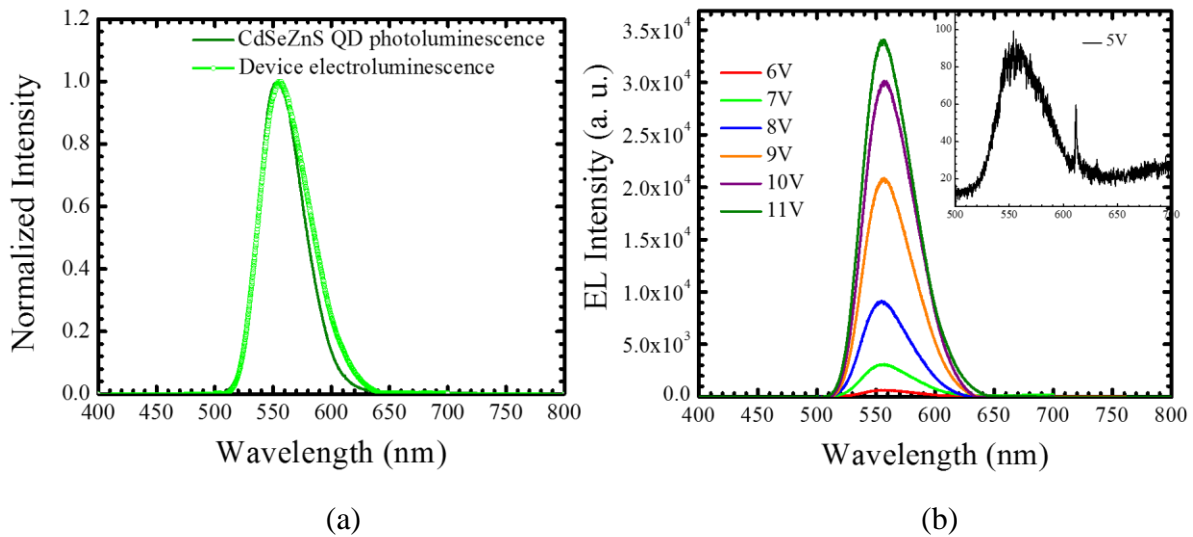

(a)
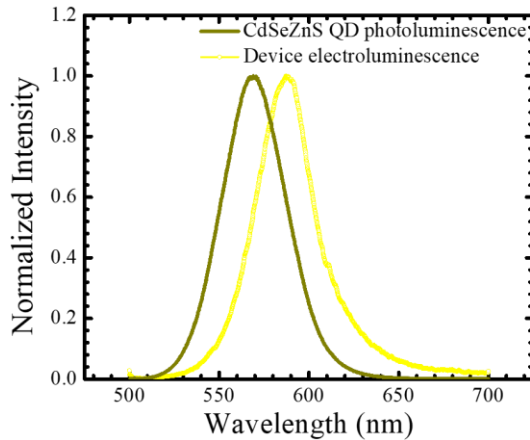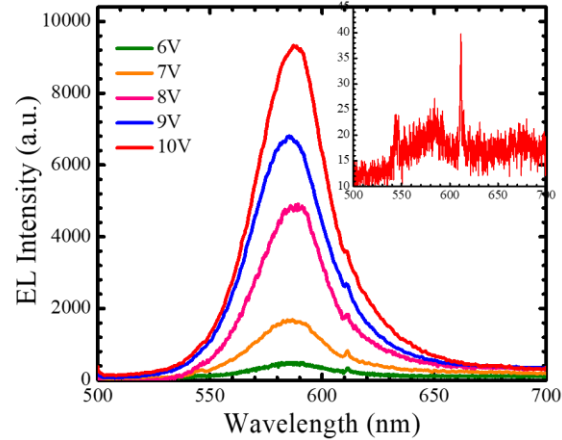
(b) (c)

Figure 3.38 (a) Yellow QLED operating at 10V. (b) The photoluminescence spectrum of the
yellow quantum dots is compared to that of the yellow QLED electroluminescence spectrum. (c)
Highly saturated, pure color electroluminescence of the device at different bias voltages.

The current-voltage characteristic of the device is shown in figure 3.39. Conduction

mechanism of the device is understood by plotting the current-voltage characteristics in log-log

scale. The current-voltage curve exhibits three distinct slopes, corresponding to Ohmic, trap

limited and space charge limited conduction regions [36, 81]. Similar to the green QLED, the

device initially operates in the Ohmic region. The slope changes to 5.4 ($J\alpha V^{5.4}$) at 4.5 V, which

corresponds to the onset of charge injection. The emission is high enough to be detected only at

5V. In the third region the current increases more gradually with a flatter slope of 3.5. This

again is considered as trap limited conduction. Finally, the relationship between J and V

becomes quadratic at 8.0 V with the onset of space charge limited conduction. In this region, the

traps are completely filled, and the current is limited by the space charge created in the device. It

can be seen that the yellow QLED device operates in the trap limited region between 4.5V and

8.0V. This range is lower for the green emitting QLED. It is reported that QLED emit

efficiently in the trap limited region as the quantum dots are considered as the traps [37].

Figure 3.39. Current-voltage characteristic of the yellow QLED with different current
conduction regions is shown.

The light output characteristics of the device are shown in figure 3.40. In figure 3.40(a), the luminance of the device is plotted as a function of bias voltage. The luminance increases with voltage and reaches 10,000 cd/m^2 at 7.7 V. The voltage at which the device luminance reaches 1000 cd/m^2 is 5.6 V and corresponding current density is 211 mA/cm^2 and at 711 mA/cm^2 it reaches 10,000 cd/A. The current and external quantum efficiencies of the device, plotted as a function of current density, are shown in figure 3.40(b). The current efficiency increases initially, reaches a maximum at 8V, and saturates. The maximum current efficiency of 1.6 cd/A is obtained at 1533.3 mA/cm^2 current density. The EQE increases to 1.4% at 900 mA/cm^2 and increases to just over 1.5% at 1533.33 mA/cm^2. Similar to current and quantum efficiencies, the luminous efficiency reaches 0.54 lm/W and decreases. As compared to the green QLED, all performance parameters are much lower. This is mainly due to the carrier lifetime difference between the quantum dots. The average lifetime of yellow quantum dots in a packed film is 3.42 ns while that of green quantum dots is 9.0 ns, which indicates that the quantum yield of yellow quantum dots is much lower than that of the green quantum dots. The EQE of the QLED is directly proportional to the quantum yield of the quantum dots according to equation. Hence, to generate the same amount of brightness, the yellow QLED requires higher current densities. As the current density increases, the number of phonons generated due to non-radiative recombination increases, which are released into the lattice in the form of thermal energy. As the temperature of the quantum dots increases it degrades and leads to further decrease in luminance.

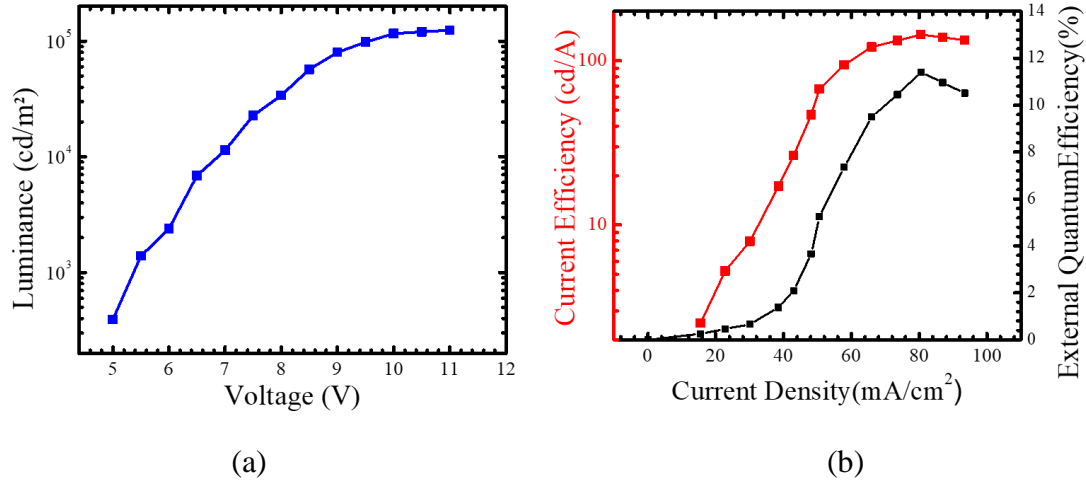(a)   (b)

Figure 3.40. (a) Luminance of the yellow QLED is plotted as a function of the bias voltage. The luminance increases with voltage and saturates at 8V. (b) The current efficiency and EQE of the device are plotted as a function of current density.

3.3.1.3. Red emitting QLED

Red emitting QLEDs are fabricated using the red (640 nm) emitting CdSe/ZnS quantum dots. The band alignment of different device layers is shown in figure 3.41. The band positions of the CTLs and the work functions of electrodes are the same as shown in figure 3.32. The band positions of the red emitting quantum dots are different than the other quantum dots. The barrier to charge injection at the nickel oxide-quantum dot interface in this case is ~1.73 eV, while there is no barrier at the ZnO–quantum dot interface.
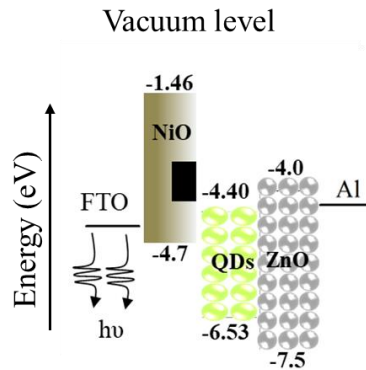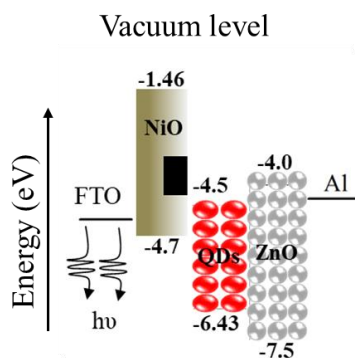

Figure 3.41. The valence and conduction band values (in eV) of the different device layers formed by spin coating are shown for the red QLED.

94

The device is forward biased in step of 1V staring from 0V. The device turns on at 4V and the emission intensity increased with increase in bias voltage. The device operating at 4V and 10V bias voltages are shown in figure 3.42(a). The normalized photoluminescence spectrum of quantum dots on glass and electroluminescence spectrum of the device at 10V are plotted in figure 3.42(b). As seen, the photoluminescence peak is at 640 nm and the electroluminescence peak is at 645 nm. The FWHM of the electroluminescence spectrum is 32 nm indicating a saturated, pure red color emission. The electroluminescence spectra at different bias voltages are plotted in figure 3.42(c). The intensity at 4.0V is very low compared to higher voltage intensities and so it is shown in the inset of figure 3.42(c).

(a)

(b)

(c)
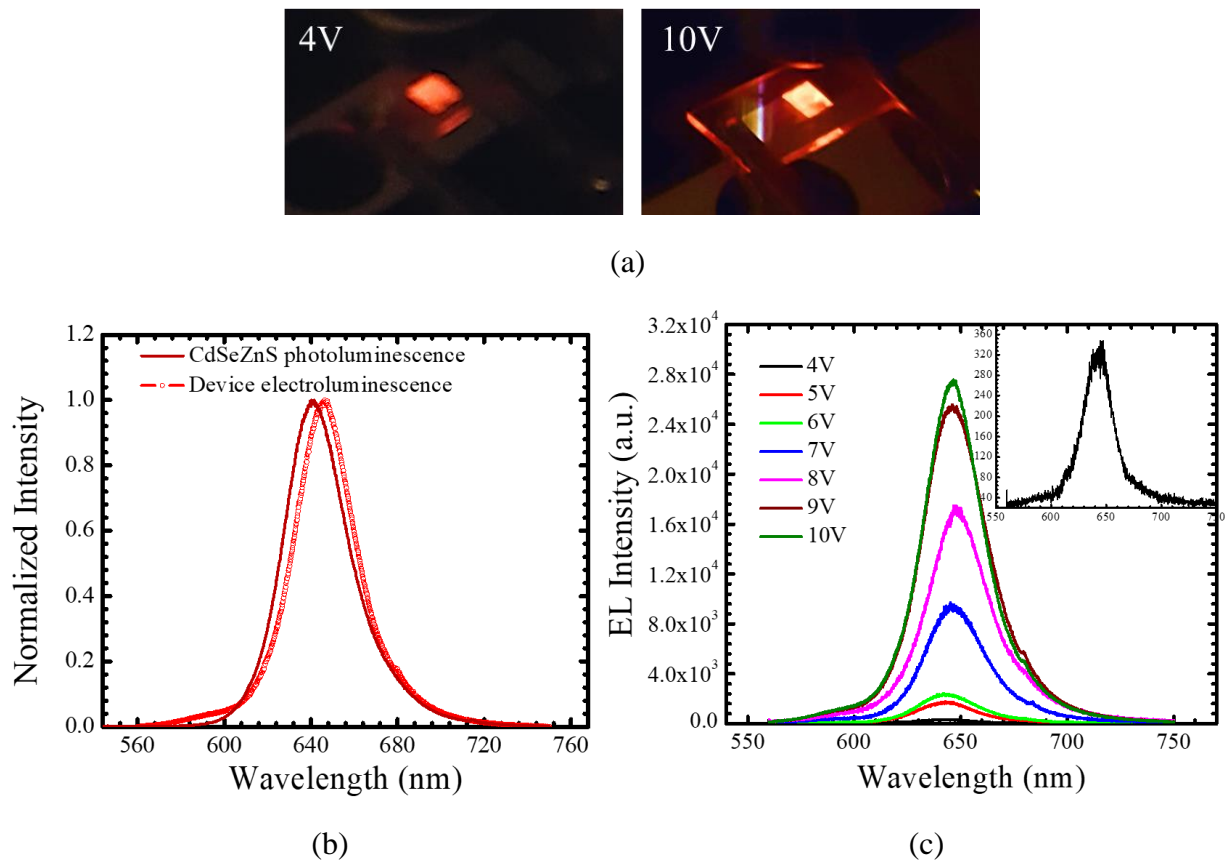
Figure 3.42. (a) Red QLED operating at 4V and 10V. (b) The photoluminescence spectrum of the red quantum dots is compared to that of the red QLED electroluminescence spectrum. (c) Highly saturated, pure red color electroluminescence of the device at different bias voltages.

The current-voltage characteristic of the device is shown in figure 3.43. It is plotted in log-log scale and different linear regions are fitted. The initial Ohmic region ends at 0.45V and the slope changes to 2.2 at 0.45V. The conduction mechanism follows space charge limited conduction between 0.45V and 3.95V. At 3.95V the slope changes to 4.9 and enters the trap limited region, which also indicates the onset of charge injection into the quantum dots. The charge injection continues till 9.0V and the device emits efficiently as described before. The device saturates and the conduction is limited by the space charge as indicated by the quadratic current-voltage relationship.
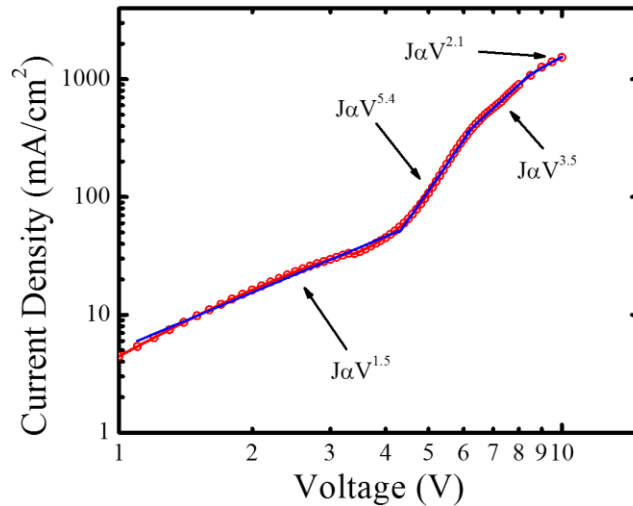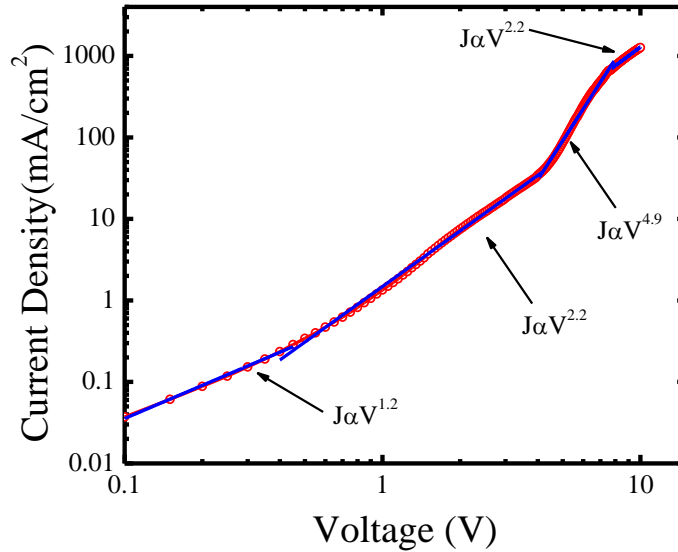

Figure 3.43. Current-voltage characteristic of the red QLED with different current conduction regions is shown.

The light output characteristics of the device are shown in figure 3.44. In figure 3.44(a), the luminance of the device is plotted as a function of bias voltage. The luminance increases with voltage and reaches 10,000 cd/m^2 at 7.7 V. The optimized luminance of a commercial LCD for normal indoor viewing is ~1000 cd/m^2. The voltage at which the device luminance reaches 1000 cd/m^2 is 5.0 V and corresponding current density is 86 mA/cm^2 and at 858 mA/cm^2 it reaches 10,000 cd/m^2. The luminance reaches a maximum of 12,900 cd/m^2 at 9.0V and

saturates. The current and external quantum efficiencies of the device, plotted as a function of current density, are shown in figure 3.44(b). Maximum current efficiency of 4.30 cd/A and EQE of 6.04% is obtained at 1011 mA/cm^2 and corresponding forward voltage is 9.0V. Both current and quantum efficiencies start to decrease after reaching the maximum value. This is usually attributed to the luminance saturation at high current densities caused by quantum dot charging. As compared to the green QLED, all performance parameters are much lower. Similar to yellow QLED, this is due to the shorter average lifetime of the red quantum dots, which is 4.30 ns. Hence, the performance of red QLED is comparable to that of the yellow QLED. Compared to yellow QLED, the red emitting device performs better with a maximum EQE of 6.04%.
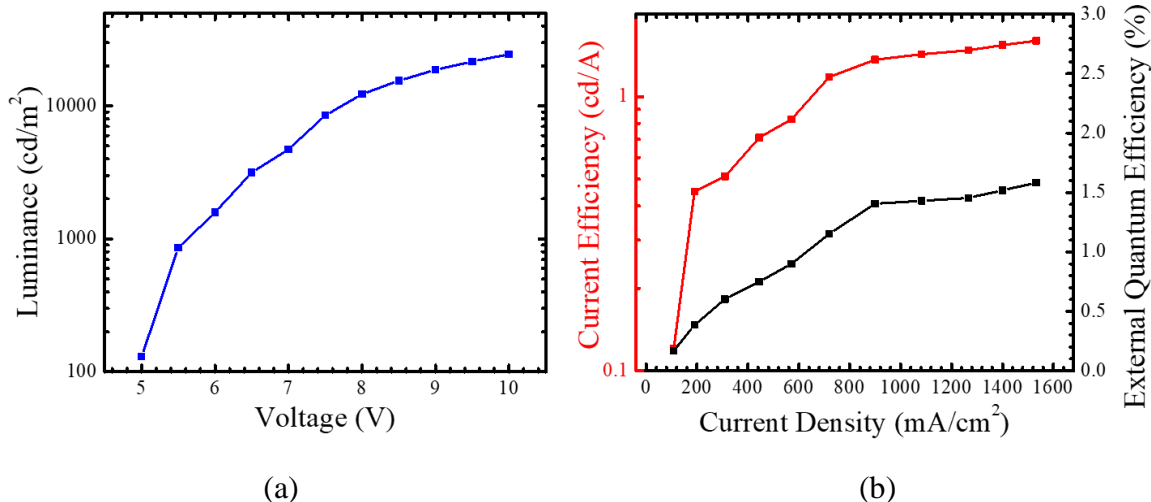

(a)   (b)
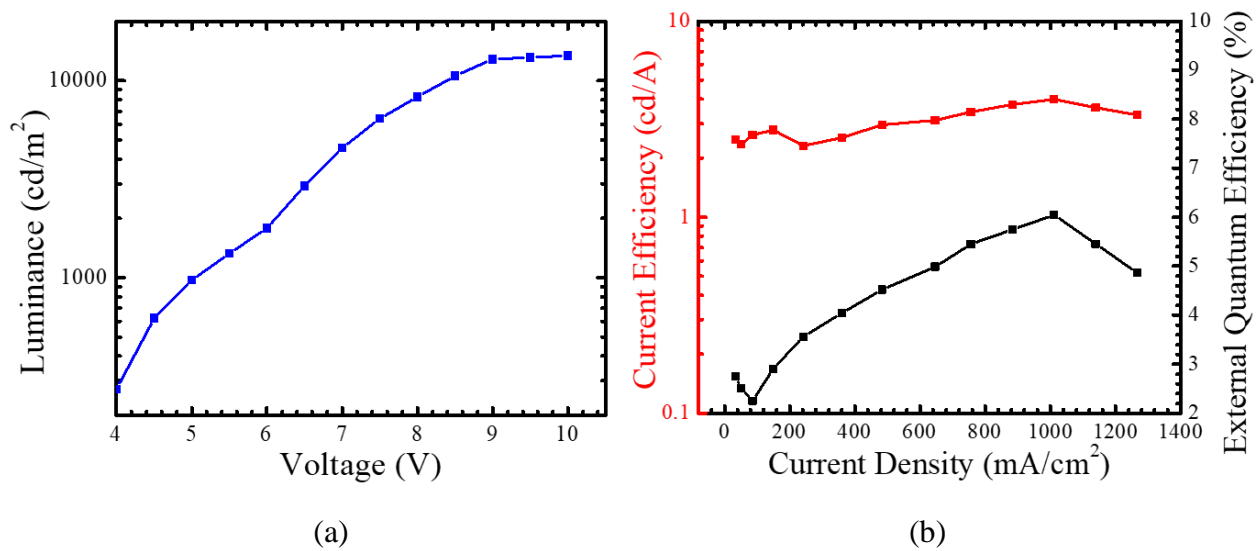
Figure 3.44. (a) Luminance of the red QLED is plotted as a function of the bias voltage. The luminance increases with voltage and saturates at 9V. (b) The current efficiency and EQE of the device are plotted as a function of current density.

The Commission internationale de l'éclairage (CIE) color coordinates of the devices are plotted on the CIE chromaticity graph shown in figure 3.45. Form the coordinates it is clear that the colors correspond to pure green, sodium yellow and pure red. When the devices are biased, electrons injected from the cathode reaches the quantum dot through the zinc oxide ETL while the holes accumulate at the nickel oxide-quantum dot interface due to energy barrier. The

electrons that reach the quantum dots gain more energy due to the applied electric field and jump into the defect states of the nickel oxide HTL. These electrons and the accumulated holes in the valence band of nickel oxide form excitons, which transfer their energy to the adjacent quantum dot via resonant energy transfer creating excitons in the quantum dots. These recombine and emit the photon with energy equivalent to the band gap of quantum dot. The energy transfer from the nickel oxide HTL to the quantum dots depends on the band gap of quantum dots as discussed in section 3.2.1. The parameters of the different QLEDs are shown in table 3.4. It can be seen that the turn-on voltage of green QLED is the highest followed by the yellow QLED and red QLED with the lowest turn-on voltage. Also, it is evident that the extended operation range of red QLED between 3.95 and 8.0V in the trap limited region is the highest among the three devices. These factors are indications that the energy transfer is highest for the red QLED and one would expect the red device to perform the best. But, it is clear that the green QLED out performs the other two devices. This is mainly attributed to the higher quantum yield of green quantum dots compared to the other two quantum dots. Even if charges are efficiently transported to the quantum dots, the recombination within the emissive layer will not result in light output in a low quantum yield material. So, the performance of green QLED cannot be compared to the other devices to understand the effect of energy transfer mechanism in a device. The yellow and red quantum dots with comparable average carrier lifetimes will have comparable quantum yields and hence the performance is mainly limited by the hole transport efficiency at the nickel oxide-quantum dot interface. Electron transport at the ZnO-quantum dot is dominated by direct charge injection as the energy barrier is non-existent.
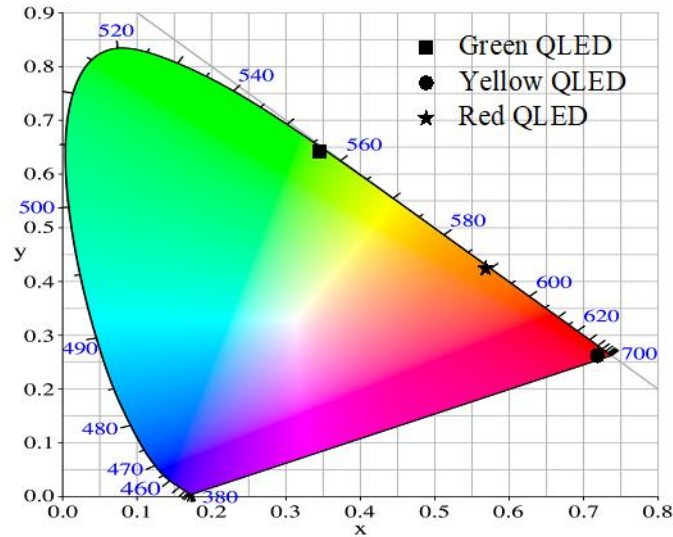
Figure 3.45. The CIE coordinates of the QLED emission plotted on a Chromaticity graph.

If the hole transport mechanism in these devices is predominantly through energy transfer, then it depends on the energy transfer rate between nickel oxide and the quantum dots. As seen from the charge transport model discussed in section 3.2.1, it is clear that the energy transfer rate with yellow quantum dots is 1.3×10^9 s^{-1} and that of red quantum dots is 3.6×10^9 s^{-1}. It is expected that the red QLED should perform better than the yellow QLED. The peak EQE of red device is ~6.0% and that of yellow device is 1.6%. Even the current efficiency of red device is better than that of yellow QLED. The optimized luminance of a commercial LCD for normal indoor viewing is ~1000 cd/m^2. It is evident form the luminance plots that the red QLED reached 1000 cd/m^2 at 86 mA/cm^2 while the yellow reached at a higher current density of 211 mA/cm^2. Even though these results support the existence of energy transfer between nickel oxide and the quantum dots, direct charge injection cannot be ruled out at high electric fields. The relative contribution of these two mechanisms to charge transport in these devices is not clear. If the two mechanisms exist simultaneously then other experiments are required to evaluate these qualitatively and then obtain the contributions quantitatively.

Table 3.4. The performance parameters of the different all-inorganic QLEDs are tabled.

QLED color	Peak wavelength (nm)	FWHM (nm)	Turn on voltage (V)	Peak luminance (cd/m²)	EQE (%)		Current efficiency (cd/A)	
					Peak	@10000 cd/m²	Peak	@10000 cd/m²
Green	555	42	4.65	124573	11.4	1.70	144	21.9
Yellow	588	38	4.50	24553	1.60	1.14	1.60	1.15
Red	646	32	3.95	13412	6.04	5.60	4.30	3.71

3.3.2. Hybrid QLED with PEDOT:PSS/nickel oxide nanoparticles HTL

3.3.2.1. Red emitting hybrid QLED

The band alignment of different device layers is shown in figure 3.46(a). The valence and conduction band positions of zinc oxide and quantum dot emissive layers are taken from literature [52]. The work function of FTO anode is reported to be 4.6-4.8 eV and that of Al cathode is 4.28 eV. Hence, there is a ~ 0.2 eV barrier for electron injection at the Al-ZnO interface. The PEDOT:PSS (poly(3,4-ethylenedioxythiophene) polystyrene sulfonate) is ntroduced between the anode and the nickel oxide nanoparticle layer. This layer acts as a hole injection layer (HIL), which reduces the hole barrier between anode and nickel oxide nanoparticles from 1.5 eV to 1.0 eV. The valence band of nickel oxide nanoparticles is much deeper than that of the nickel oxide thin film. This enables a very low barrier to injection of holes at the nickel oxide nanoparticles-quantum dot interface. The barrier to hole injection is around ~0.23 eV. The device operating at 9 V is shown in figure 3.46(b).
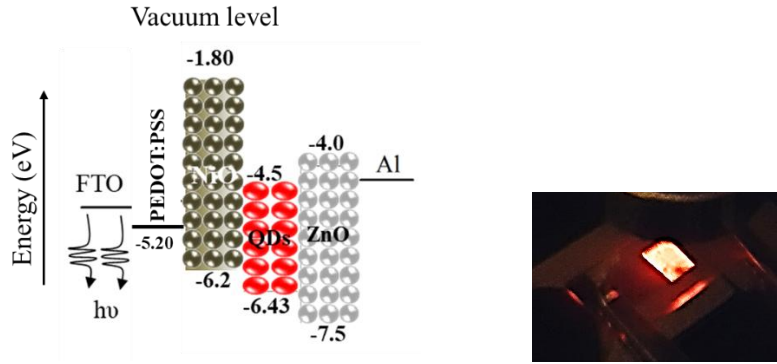
Figure 3.46. (a) The valence and conduction band values (in eV) of the different device layers formed by spin coating are shown for the red hybrid QLED. (b) Hybrid red QLED operating at 9V.

The device is forward biased it turns on at 3V and the emission intensity increased with increase in bias voltage. The normalized photoluminescence spectrum of quantum dots on glass and electroluminescence spectrum of the device at 9V are plotted in figure 3.47(a). As seen, the photoluminescence peak is at 640 nm and the electroluminescence peak is at 649 nm. The FWHM of the electroluminescence spectrum is 33 nm indicating a saturated, pure red color emission. The electroluminescence spectra at different bias voltages are plotted in figure 3.47(b). The current-voltage characteristics of the device are shown in figure 3.47(c). It is plotted in log-log scale and different linear regions are fitted. The turn-on voltage of the device is 3V as seen from the slope change.

(a)

(b)

101
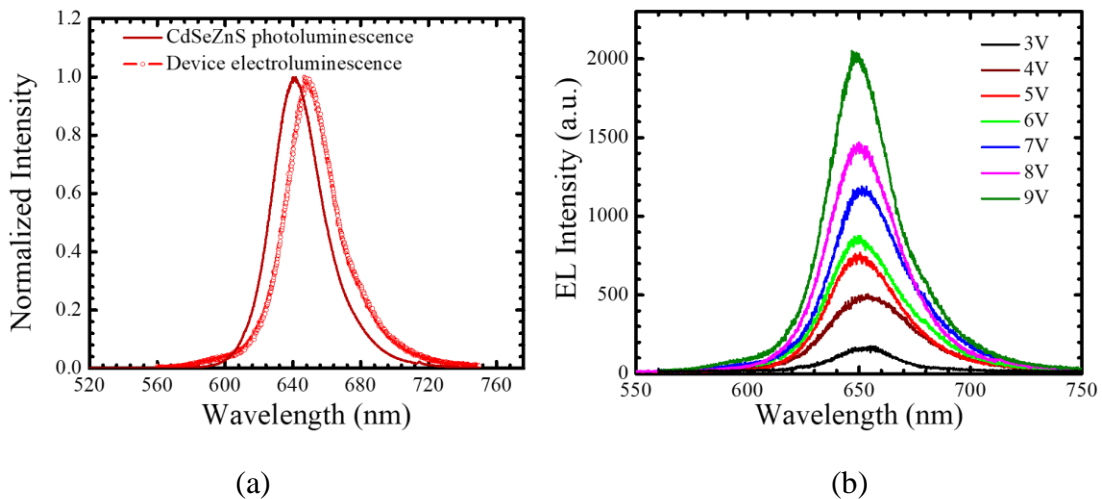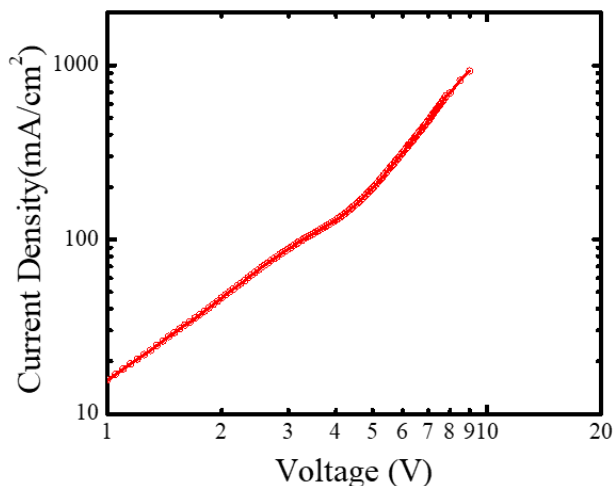
(c)

Figure 3.47. (a) The photoluminescence spectrum of the red quantum dots is compared to that of the hybrid red QLED electroluminescence spectrum. (b) Electroluminescence of the hybrid device at different bias voltages. (c) Current-voltage characteristic of red emitting hybrid QLED.

The light output characteristics of the device are shown in figure. In figure 3.48(a), the luminance of the device is plotted as a function of bias voltage. The luminance increases with voltage and reaches a maximum of ~1800 cd/m^2 at 9V. The voltage at which the device luminance reaches 1000 cd/m^2 is 6.76 V and corresponding current density is 436 mA/cm^2. The current and external quantum efficiencies of the device, plotted as a function of current density, are shown in figure 3.48(b). Maximum current efficiency of 4.14 cd/A and EQE of 2.36% is obtained at 129 mA/cm^2 and corresponding forward voltage is 4.0V. Both current and quantum efficiencies start to decrease after reaching the maximum value at 4.0V. Performance of these devices is much lower than that of the all-inorganic devices with nickel oxide thin film. This is due to the voids formed during the spin coating process. The nickel oxide nanoparticle powder is not completely dispersed in the solvent as the quantum dots or ZnO nanoparticles. Hence, forming a uniform, smooth film is difficult with the nickel oxide nanoparticles.

102

The working of this device is very close to that of commonly reported hybrid devices with polymer or organic HIL/HTL. The charge transport in these devices is dominated by direct charge injection process and there is no evidence of energy transfer. Direct hole injection form HTL to quantum dots is possible as the nickel oxide nanoparticle HTL has a very deep valence band at -6.2 eV close to the valence band of quantum dots. This also enables a much lower turn-on voltage compared to the devices with nickel oxide thin film. The deep valence band is a disadvantage as the barrier to hole injection from anode is increased. In order to reduce this barrier, additional hole injection layer is inserted between the anode and the HTL. With a polymer material the device is susceptible to damage from oxygen and moisture in the atmosphere.

(a)   (b)
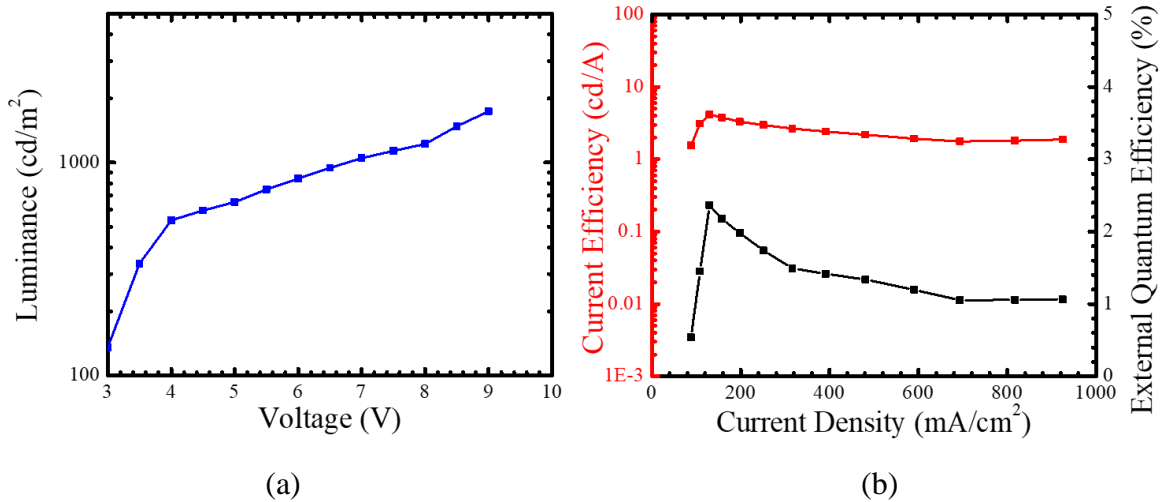
Figure 3.48. (a) Luminance of the hybrid red QLED is plotted as a function of the bias voltage. (b) The current efficiency and EQE of the hybrid device are plotted as a function of current density.

4. CONCLUSION AND FUTURE WORK

4.1. Conclusion

In conclusion, efficient QLEDs with nickel oxide thin film and nickel oxide nanoparticles are fabricated and characterized. The all-inorganic QLED with nickel oxide thin film HTL is shown to operate by energy transfer mechanism between the HTL and quantum dots. The nickel oxide thin film defect emission was engineered through non-stoichiometry of the film and assigned based on structural, elemental and electrical properties of the nickel oxide film. It is shown that the energy transfer is dependent on the spectral overlap of the quantum dot absorbance with the nickel oxide thin film defect emission spectrum. It is evident form the transfer time that energy transfer efficiency is maximum for the red quantum dots and reduces with quantum dot size. This is due to the non-availability of resonant states between the nickel oxide thin film HTL and smaller quantum dots. The performance of QLEDs with yellow and red quantum dots clearly supports this charge transport model as the red QLED performed much better than that of the yellow QLED. Even though the energy transfer efficiency is lower for the green quantum dots, the green QLED with a maximum EQE of 11.4% performed the best amongst the three types of QLEDs. This is mainly due to the high quantum yield of the green quantum dots compared to the other quantum dots. It is clear from the transfer model that the devices using red quantum dots with comparable quantum yield with blue quantum dots should perform much better. The hybrid QLED with PEDOT:PSS/nickel oxide nanoparticle HIL/HTL turns on at lower voltage than the all-inorganic QLEDs, but the performance is much lower. Also, with a deep valence band of the nickel oxide nanoparticles the QLED predominantly operates under charge injection mechanism.

4.2. Future work

It is anticipated that this resonant energy transfer property can be further exploited to fabricate robust and efficient all-inorganic white LEDs with RGB quantum dots by further engineering the trap states within the nickel oxide thin film bandgap to allow for spectral overlap with RGB quantum dots. Further work is needed to determine exactly which quantum states are populated by the energy transfer, and if this can be further controlled to improve the efficiency of such devices. Moreover, new experiments are required to quantify the relative contributions of energy transfer and direct charge injection mechanisms to the overall charge transport within the QLED.

References

[1] L. Halonen, E. Tetri and P. Bhusal, *Guidebook on Energy Efficient Electric Lighting for Buildings*. Aalto: Aalto University School of Science and Technology, 2010.

[2] D. Feldwinn, "The past, present and future of lighting", University of California, Santa Barbara, 2017.

[3] R. Baldwin, "50 Years of LED Technology", *WIRED*, 2018. [Online]. Available: https://www.wired.com/2012/10/the-history-of-led/. [Accessed: 28- Feb- 2018].

[4] "What is (IR)LED ?A light-emitting diode (LED) | DVR Unlimited", *Blog.dvrunlimited.com*, 2018. [Online]. Available: https://blog.dvrunlimited.com/archives/2499. [Accessed: 28- Feb- 2018].

[5] S. Dimitrijev, *Principles of semiconductor devices*, 2nd ed. New York: Oxford University Press, 2012.

[6] D. Neamen, *An introduction to semiconductor devices*. Boston, Mass. [u.a.]: McGraw-Hill Higher Education, 2008.

[7] "Fermi level and Fermi function", *Hyperphysics.phy-astr.gsu.edu*, 2018. [Online]. Available: http://hyperphysics.phy-astr.gsu.edu/hbase/Solids/Fermi.html. [Accessed: 28- Feb- 2018].

[8] N. Holonyak and S. Bevacqua, "COHERENT (VISIBLE) LIGHT EMISSION FROM Ga(As1−xPx) JUNCTIONS", *Applied Physics Letters*, vol. 1, no. 4, pp. 82-83, 1962.

[9] D. Ban, H. Luo, H. Liu, Z. Wasilewski, A. SpringThorpe, R. Glew and M. Buchanan, "Optimized GaAs∕AlGaAs light-emitting diodes and high efficiency wafer-fused optical up-conversion devices", *Journal of Applied Physics*, vol. 96, no. 9, pp. 5243-5248, 2004.

[10] S. Dutta Gupta and B. Jatothu, "Fundamentals and applications of light-emitting diodes (LEDs) in in vitro plant growth and morphogenesis", *Plant Biotechnology Reports*, vol. 7, no. 3, pp. 211-220, 2013.

[11] H. Jeong, R. Salas-Montiel, G. Lerondel and M. Jeong, "Indium gallium nitride-based ultraviolet, blue, and green light-emitting diodes functionalized with shallow periodic hole patterns", *Scientific Reports*, vol. 7, p. 45726, 2017.

[12] C. Skierbiszewski, P. Perlin, I. Grzegory, Z. Wasilewski, M. Siekacz, A. Feduniewicz, P. Wisniewski, J. Borysiuk, P. Prystawko, G. Kamler, T. Suski and S. Porowski, "High power blue–violet InGaN laser diodes grown on bulk GaN substrates by plasma-assisted molecular beam epitaxy", *Semiconductor Science and Technology*, vol. 20, no. 8, pp. 809-813, 2005.

[13] S. Koizumi, "Ultraviolet Emission from a Diamond pn Junction", *Science*, vol. 292, no. 5523, pp. 1899-1901, 2001.

[14] Y. Taniyasu, M. Kasu and T. Makimoto, "An aluminium nitride light-emitting diode with a wavelength of 210 nanometres", *Nature*, vol. 441, no. 7091, pp. 325-328, 2006.

[15] Y. Kubota, K. Watanabe, O. Tsuda and T. Taniguchi, "Deep Ultraviolet Light-Emitting Hexagonal Boron Nitride Synthesized at Atmospheric Pressure", *ChemInform*, vol. 38, no. 45, 2007.

[16] T. Dawson, "Development of efficient and durable sources of white light", *Coloration Technology*, vol. 126, no. 1, pp. 1-10, 2010.

[17] T. Bosschaert, "Except Integrated Sustainability", *Except Integrated Sustainability*, 2018. [Online]. Available: http://www.except.nl/en/articles/92-led-artificial-light-guide. [Accessed: 28- Feb- 2018].

[18] A. Zukauskas, M. Shur and R. Gaska, *Introduction to solid state lighting*. New York: John Wiley & Sons, 2002.

[19] D. A. Steigerwald *et al*., "Illumination with solid state lighting technology," in *IEEE Journal of Selected Topics in Quantum Electronics*, vol. 8, no. 2, pp. 310-320, Mar/Apr 2002.

[20] B. Geffroy, P. le Roy and C. Prat, "Organic light-emitting diode (OLED) technology: materials, devices and display technologies", *Polymer International*, vol. 55, no. 6, pp. 572-582, 2006.

[21] J. Tremblay, "The rise of OLED displays | July 11, 2016 Issue - Vol. 94 Issue 28 | Chemical & Engineering News", *Cen.acs.org*, 2018. [Online]. Available: https://cen.acs.org/articles/94/i28/rise-OLED-displays.html. [Accessed: 28- Feb- 2018].

[22] S. Ho, S. Liu, Y. Chen and F. So, "Review of recent progress in multilayer solution-processed organic light-emitting diodes", *Journal of Photonics for Energy*, vol. 5, no. 1, p. 057611, 2015.

[23] C. Sekine, Y. Tsubata, T. Yamada, M. Kitano and S. Doi, "Recent progress of high performance polymer OLED and OPV materials for organic printed electronics", *Science and Technology of Advanced Materials*, vol. 15, no. 3, p. 034203, 2014.

[24] R. Meerheim, S. Scholz, S. Olthof, G. Schwartz, S. Reineke, K. Walzer and K. Leo, "Influence of charge balance and exciton distribution on efficiency and lifetime of phosphorescent organic light-emitting devices", *Journal of Applied Physics*, vol. 104, no. 1, p. 014510, 2008.

[25] Department of Energy, "Solid-State Lighting Research and Development", 2010.

[26] J. Caruge, J. Halpert, V. Bulović and M. Bawendi, "NiO as an Inorganic Hole-Transporting Layer in Quantum-Dot Light-Emitting Devices", *Nano Letters*, vol. 6, no. 12, pp. 2991-2994, 2006.

[27] J. Steckel, P. Snee, S. Coe-Sullivan, J. Zimmer, J. Halpert, P. Anikeeva, L. Kim, V. Bulovic and M. Bawendi, "Color-Saturated Green-Emitting QD-LEDs", *Angewandte Chemie International Edition*, vol. 45, no. 35, pp. 5796-5799, 2006.

[28] L. Swafford, L. Weigand, M. Bowers, J. McBride, J. Rapaport, T. Watt, S. Dixit, L. Feldman and S. Rosenthal, "Homogeneously Alloyed CdSxSe1-xNanocrystals: Synthesis, Characterization, and Composition/Size-Dependent Band Gap", *Journal of the American Chemical Society*, vol. 128, no. 37, pp. 12299-12306, 2006.

[29] C. de Mello Donegá, *Nanoparticles*. Berlin, Heidelberg: Springer Berlin Heidelberg, 2014, pp. 13-51.

[30] V. Colvin, M. Schlamp and A. Alivisatos, "Light-emitting diodes made from cadmium selenide nanocrystals and a semiconducting polymer", *Nature*, vol. 370, no. 6488, pp. 354-357, 1994.

[31] B. Dabbousi, M. Bawendi, O. Onitsuka and M. Rubner, "Electroluminescence from CdSe quantum-dot/polymer composites", *Applied Physics Letters*, vol. 66, no. 11, pp. 1316-1318, 1995.

[32] H. Mattoussi, L. Radzilowski, B. Dabbousi, E. Thomas, M. Bawendi and M. Rubner, "Electroluminescence from heterostructures of poly(phenylene vinylene) and inorganic CdSe nanocrystals", *Journal of Applied Physics*, vol. 83, no. 12, pp. 7965-7974, 1998.

[33] S. Coe, W. Woo, M. Bawendi and V. Bulović, "Electroluminescence from single monolayers of nanocrystals in molecular organic devices", *Nature*, vol. 420, no. 6917, pp. 800-803, 2002.

[34] A. Rizzo, M. Mazzeo, M. Palumbo, G. Lerario, S. D'Amone, R. Cingolani and G. Gigli, "Hybrid Light-Emitting Diodes from Microcontact-Printing Double-Transfer of Colloidal Semiconductor CdSe/ZnS Quantum Dots onto Organic Layers", *Advanced Materials*, vol. 20, no. 10, pp. 1886-1891, 2008.

[35] J. Stouwdam and R. Janssen, "Red, green, and blue quantum dot LEDs with solution processable ZnO nanocrystal electron injection layers", *Journal of Materials Chemistry*, vol. 18, no. 16, p. 1889, 2008.

[36] B. Mashford, M. Stevenson, Z. Popovic, C. Hamilton, Z. Zhou, C. Breen, J. Steckel, V. Bulovic, M. Bawendi, S. Coe-Sullivan and P. Kazlas, "High-efficiency quantum-dot light-emitting devices with enhanced charge injection", *Nature Photonics*, vol. 7, no. 5, pp. 407-412, 2013.

[37] Y. Yang, Y. Zheng, W. Cao, A. Titov, J. Hyvonen, J. Manders, J. Xue, P. Holloway and L. Qian, "High-efficiency light-emitting devices based on quantum dots with tailored nanostructures", *Nature Photonics*, vol. 9, no. 4, pp. 259-266, 2015.

[38] K. Acharya, A. Titov, J. Hyvonen, C. Wang, J. Tokarz and P. Holloway, "High efficiency quantum dot light emitting diodes from positive aging", *Nanoscale*, vol. 9, no. 38, pp. 14451-14457, 2017.

[39]]P. Anikeeva, C. Madigan, J. Halpert, M. Bawendi and V. Bulović, "Electronic and excitonic processes in light-emitting devices based on organic materials and colloidal quantum dots", *Physical Review B*, vol. 78, no. 8, 2008.

[40] L. Qian, Y. Zheng, J. Xue and P. Holloway, "Stable and efficient quantum-dot light-emitting diodes based on solution-processed multilayer structures", *Nature Photonics*, vol. 5, no. 9, pp. 543-548, 2011.

[41] J. Kwak, W. Bae, D. Lee, I. Park, J. Lim, M. Park, H. Cho, H. Woo, D. Yoon, K. Char, S. Lee and C. Lee, "Bright and Efficient Full-Color Colloidal Quantum Dot Light-Emitting Diodes Using an Inverted Device Structure", *Nano Letters*, vol. 12, no. 5, pp. 2362-2366, 2012.

[42] V. Wood, M. Panzer, J. Halpert, J. Caruge, M. Bawendi and V. Bulović, "Selection of Metal Oxide Charge Transport Layers for Colloidal Quantum Dot LEDs", *ACS Nano*, vol. 3, no. 11, pp. 3581-3586, 2009.

[43] B. Mashford, T. Nguyen, G. Wilson and P. Mulvaney, "All-inorganic quantum-dot light-emitting devices formed via low-cost, wet-chemical processing", *J. Mater. Chem.*, vol. 20, no. 1, pp. 167-172, 2010.

[44] S. Bhaumik and A. Pal, "All-Inorganic Light-Emitting Diodes Based on Solution-Processed Nontoxic and Earth-Abundant Nanocrystals", *IEEE Journal of Quantum Electronics*, vol. 49, no. 3, pp. 325-330, 2013.

[45] H. Nguyen, N. Nguyen and S. Lee, "Application of solution-processed metal oxide layers as charge transport layers for CdSe/ZnS quantum-dot LEDs", *Nanotechnology*, vol. 24, no. 11, p. 115201, 2013.

[46] J. Caruge, J. Halpert, V. Bulović and M. Bawendi, "NiO as an Inorganic Hole-Transporting Layer in Quantum-Dot Light-Emitting Devices", *Nano Letters*, vol. 6, no. 12, pp. 2991-2994, 2006.

[47] X. Zhang, H. Dai, J. Zhao, C. Li, S. Wang and X. Sun, "Effects of the thickness of NiO hole transport layer on the performance of all-inorganic quantum dot light emitting diode", *Thin Solid Films*, vol. 567, pp. 72-76, 2014.

[48] J. Chen, Q. Huang, Q. Du, D. Zhao, F. Xu, J. Pan, W. Lei and A. Nathan, "Localized surface plasmon resonance enhanced quantum dot light-emitting diodes via quantum dot-capped gold nanoparticles", *RSC Adv.*, vol. 4, no. 101, pp. 57574-57579, 2014.

[49] S. Bhaumik and A. Pal, "Light-Emitting Diodes Based on Solution-Processed Nontoxic Quantum Dots: Oxides as Carrier-Transport Layers and Introducing Molybdenum Oxide Nanoparticles as a Hole-Inject Layer", *ACS Applied Materials & Interfaces*, vol. 6, no. 14, pp. 11348-11356, 2014.

[50] R. Vasan, H. Salman and M. O. Manasreh, "All inorganic quantum dot light emitting devices with solution processed metal oxide transport layers", *MRS Advances*, vol. 1, no. 04, pp. 305-310, 2016.

[51] W. Ji, S. Liu, H. Zhang, R. Wang, W. Xie and H. Zhang, "Ultrasonic Spray Processed, Highly Efficient All-Inorganic Quantum-Dot Light-Emitting Diodes", *ACS Photonics*, vol. 4, no. 5, pp. 1271-1278, 2017.

[52] R. Vasan, H. Salman and M. O. Manasreh, "Solution Processed High Efficiency Quantum Dot Light Emitting Diode with Inorganic Charge Transport Layers", *IEEE Electron Device Letters*, vol. 39, no. 4, pp. 536-539, 2018.

[53] Y. Shirasaki, G. Supran, M. Bawendi and V. Bulović, "Emergence of colloidal quantum-dot light-emitting technologies", *Nature Photonics*, vol. 7, no. 1, pp. 13-23, 2013.

[54] A. Efros, M. Rosen, M. Kuno, M. Nirmal, D. Norris and M. Bawendi, "Band-edge exciton in quantum dots of semiconductors with a degenerate valence band: Dark and bright exciton states", *Physical Review B*, vol. 54, no. 7, pp. 4843-4856, 1996.

[55] D. Talapin, I. Mekis, S. Goetzinger, A. Kornowski, O. Benson and H. Weller, "CdSe/CdS/ZnS and CdSe/ZnSe/ZnS Core/Shell/Shell Nanocrystals", *ChemInform*, vol. 36, no. 10, 2005.

[56] P. Reiss, J. Bleuse and A. Pron, "Highly Luminescent CdSe/ZnSe Core/Shell Nanocrystals of Low Size Dispersion", *Nano Letters*, vol. 2, no. 7, pp. 781-784, 2002.

[57] W. Bae, K. Char, H. Hur and S. Lee, "Single-Step Synthesis of Quantum Dots with Chemical Composition Gradients", *Chemistry of Materials*, vol. 20, no. 2, pp. 531-539, 2008.

[58] B. Kumar, R. Hue, W. Gladfelter and S. Campbell, "Comparing direct charge injection and Forster energy transfer into quantum dots in hybrid organic/inorganic quantum dot light emitting devices", *Journal of Applied Physics*, vol. 112, no. 3, p. 034501, 2012.

[59] B. Kumar, S. Campbell and P. Paul Ruden, "Modeling charge transport in quantum dot light emitting devices with NiO and ZnO transport layers and Si quantum dots", *Journal of Applied Physics*, vol. 114, no. 4, p. 044507, 2013.

[60] W. Bae, Y. Park, J. Lim, D. Lee, L. Padilha, H. McDaniel, I. Robel, C. Lee, J. Pietryga and V. Klimov, "Controlling the influence of Auger recombination on the performance of quantum-dot light-emitting diodes", *Nature Communications*, vol. 4, 2013.

[61] D. Bozyigit and V. Wood, "Challenges and solutions for high-efficiency quantum dot-based LEDs", *MRS Bulletin*, vol. 38, no. 09, pp. 731-736, 2013.

[62] J. Manders, S. Tsang, M. Hartel, T. Lai, S. Chen, C. Amb, J. Reynolds and F. So, "Solution-Processed Nickel Oxide Hole Transport Layers in High Efficiency Polymer Photovoltaic Cells", *Advanced Functional Materials*, vol. 23, no. 23, pp. 2993-3001, 2013.

[63] S. Liu, R. Liu, Y. Chen, S. Ho, J. Kim and F. So, "Nickel Oxide Hole Injection/Transport Layers for Efficient Solution-Processed Organic Light-Emitting Diodes", *Chemistry of Materials*, vol. 26, no. 15, pp. 4528-4534, 2014.

[64] J. Li, Y. Shao, X. Chen, H. Wang, Y. Li and Q. Zhang, "All-inorganic quantum-dot light-emitting-diodes with vertical nickel oxide nanosheets as hole transport layer", *Progress in Natural Science: Materials International*, vol. 26, no. 5, pp. 503-509, 2016.

[65] N. Widjonarko, E. Ratcliff, C. Perkins, A. Sigdel, A. Zakutayev, P. Ndione, D. Gillaspie, D. Ginley, D. Olson and J. Berry, "Sputtered nickel oxide thin film for efficient hole transport layer in polymer–fullerene bulk-heterojunction organic solar cell", *Thin Solid Films*, vol. 520, no. 10, pp. 3813-3818, 2012.

[66] R. Srnanek, I. Hotovy, V. Malcher, A. Vincze, D. McPhail and S. Littlewood, "A Raman study of NiOx films for gas sensors applications", *ASDAM 2000. Conference Proceedings. Third International Euro Conference on Advanced Semiconductor Devices and Microsystems (Cat. No.00EX386)*, pp. 303-306, 2000.

[67] W. Bae, J. Kwak, J. Park, K. Char, C. Lee and S. Lee, "Highly Efficient Green-Light-Emitting Diodes Based on CdSe@ZnS Quantum Dots with a Chemical-Composition Gradient", *Advanced Materials*, vol. 21, no. 17, pp. 1690-1694, 2009.

[68] J. Zhou, Y. Liu, J. Tang and W. Tang, "Surface ligands engineering of semiconductor quantum dots for chemosensory and biological applications", *Materials Today*, vol. 20, no. 7, pp. 360-376, 2017.

[69] S. Nalage, M. Chougule, S. Sen, P. Joshi and V. Patil, "Sol–gel synthesis of nickel oxide thin films and their characterization", *Thin Solid Films*, vol. 520, no. 15, pp. 4835-4840, 2012.

[70] R. Vasan, F. Gao, M. O. Manasreh and C. Heyes, "Investigation of charge transport between nickel oxide nanoparticles and CdSe/ZnS alloyed nanocrystals", *MRS Advances*, vol. 2, no. 51, pp. 2935-2941, 2017.

[71] T. Hirao, M. Furuta, T. Hiramatsu, T. Matsuda, C. Li, H. Furuta, H. Hokari, M. Yoshida, H. Ishii and M. Kakegawa, "Bottom-Gate Zinc Oxide Thin-Film Transistors (ZnO TFTs) for AM-LCDs", *IEEE Transactions on Electron Devices*, vol. 55, no. 11, pp. 3136-3142, 2008.

[72] X. Xu, Q. Cui, Y. Jin and X. Guo, "Low-voltage zinc oxide thin-film transistors with solution-processed channel and dielectric layers below 150 °C", *Applied Physics Letters*, vol. 101, no. 22, p. 222114, 2012.

[73] B. Omogo, F. Gao, P. Bajwa, M. Kaneko and C. Heyes, "Reducing Blinking in Small Core–Multishell Quantum Dots by Carefully Balancing Confinement Potential and Induced Lattice Strain: The "Goldilocks" Effect", *ACS Nano*, vol. 10, no. 4, pp. 4072-4082, 2016.

[74] F. Gao, A. Kreidermacher, I. Fritsch and C. Heyes, "3D Imaging of Flow Patterns in an Internally-Pumped Microfluidic Device: Redox Magnetohydrodynamics and Electrochemically-Generated Density Gradients", *Analytical Chemistry*, vol. 85, no. 9, pp. 4414-4422, 2013.

[75] H. Kuzmany, *Solid-state spectroscopy*, 2nd ed. Heidelberg: Springer, 2009, pp. 185-186.

[76] H. Kuzmany, *Solid-state spectroscopy*, 2nd ed. Heidelberg: Springer, 2009, pp. 314-316.

[77] D. Schroder, *Semiconductor material and device characterization*, 3rd ed. New York: John Wiley & Sons, 2006, pp. 545-547.

[78] N. Durisic, A. Godin, D. Walters, P. Grütter, P. Wiseman and C. Heyes, "Probing the "Dark" Fraction of Core–Shell Quantum Dots by Ensemble and Single Particle pH-Dependent Spectroscopy", *ACS Nano*, vol. 5, no. 11, pp. 9062-9073, 2011.

[79] F. Gao, P. Bajwa, A. Nguyen and C. Heyes, "Shell-Dependent Photoluminescence Studies Provide Mechanistic Insights into the Off–Grey–On Transitions of Blinking Quantum Dots", *ACS Nano*, vol. 11, no. 3, pp. 2905-2916, 2017.

[80] F. Jiang, W. Choy, X. Li, D. Zhang and J. Cheng, "Post-treatment-Free Solution-Processed Non-stoichiometric NiOx Nanoparticles for Efficient Hole-Transport Layers of Organic Optoelectronic Devices", *Advanced Materials*, vol. 27, no. 18, pp. 2930-2937, 2015.

[81] F. Chiu, "A Review on Conduction Mechanisms in Dielectric Films", *Advances in Materials Science and Engineering*, vol. 2014, pp. 1-18, 2014.

[82] V. Mihailetchi, J. Wildeman and P. Blom, "Space-Charge Limited Photocurrent", *Physical Review Letters*, vol. 94, no. 12, pp. 6602-6604, 2005.

[83] S. Cheung and N. Cheung, "Extraction of Schottky diode parameters from forward current-voltage characteristics", *Applied Physics Letters*, vol. 49, no. 2, pp. 85-87, 1986.

[84] M. Stamataki, C. Sargentis, D. Tsamakis, I. Fasaki and M. Kompitsas, "Hydrogen gas sensing application of Al/NiO Schottky diode", *2008 IEEE Sensors*, pp. 843-846, 2008.

[85] R. Gupta, K. Ghosh and P. Kahol, "Fabrication and electrical characterization of Au/p-Si/STO/Au contact", *Current Applied Physics*, vol. 9, no. 5, pp. 933-936, 2009.

[86] D. Schroder, *Semiconductor material and device characterization*, 3rd ed. New York: John Wiley & Sons, 2006, pp. 160-162.

[87] K. Wang, J. Jeng, P. Shen, Y. Chang, E. Diau, C. Tsai, T. Chao, H. Hsu, P. Lin, P. Chen, T. Guo and T. Wen, "p-type Mesoscopic Nickel Oxide/Organometallic Perovskite Heterojunction Solar Cells", *Scientific Reports*, vol. 4, no. 1, 2014.

[88] M. Arefi and S. Rezaei-Zarchi, "Synthesis of Zinc Oxide Nanoparticles and Their Effect on the Compressive Strength and Setting Time of Self-Compacted Concrete Paste as Cementitious Composites", *International Journal of Molecular Sciences*, vol. 13, no. 12, pp. 4340-4350, 2012.

[89] T. Franzl, T. Klar, S. Schietinger, A. Rogach and J. Feldmann, "Exciton Recycling in Graded Gap Nanocrystal Structures", *Nano Letters*, vol. 4, no. 9, pp. 1599-1603, 2004.

[90] C. Rowland, I. Fedin, H. Zhang, S. Gray, A. Govorov, D. Talapin and R. Schaller, "Picosecond energy transfer and multiexciton transfer outpaces Auger recombination in binary CdSe nanoplatelet solids", *Nature Materials*, vol. 14, no. 5, pp. 484-489, 2015.

[91] M. Achermann, M. Petruska, S. Crooker and V. Klimov, "Picosecond Energy Transfer in Quantum Dot Langmuir−Blodgett Nanoassemblies", *The Journal of Physical Chemistry B*, vol. 107, no. 50, pp. 13782-13787, 2003.

[92] T. Franzl, D. Koktysh, T. Klar, A. Rogach, J. Feldmann and N. Gaponik, "Fast energy transfer in layer-by-layer assembled CdTe nanocrystal bilayers", *Applied Physics Letters*, vol. 84, no. 15, pp. 2904-2906, 2004.

[93] P. Anikeeva, C. Madigan, S. Coe-Sullivan, J. Steckel, M. Bawendi and V. Bulović, "Photoluminescence of CdSe/ZnS core/shell quantum dots enhanced by energy transfer from a phosphorescent donor", *Chemical Physics Letters*, vol. 424, no. 1-3, pp. 120-125, 2006.

[94] K. Zheng, K. Žídek, M. Abdellah, W. Zhang, P. Chábera, N. Lenngren, A. Yartsev and T. Pullerits, "Ultrafast Charge Transfer from CdSe Quantum Dots to p-Type NiO: Hole Injection vs Hole Trapping", *The Journal of Physical Chemistry C*, vol. 118, no. 32, pp. 18462-18471, 2014.

[95] S. Yue, K. Liu, R. Xu, M. Li, M. Azam, K. Ren, J. Liu, Y. Sun, Z. Wang, D. Cao, X. Yan, S. Qu, Y. Lei and Z. Wang, "Efficacious engineering on charge extraction for realizing highly efficient perovskite solar cells", *Energy & Environmental Science*, vol. 10, no. 12, pp. 2570-2578, 2017.

[96] X. Chang, W. Li, L. Zhu, H. Liu, H. Geng, S. Xiang, J. Liu and H. Chen, "Carbon-Based CsPbBr3 Perovskite Solar Cells: All-Ambient Processes and High Thermal Stability", *ACS Applied Materials & Interfaces*, vol. 8, no. 49, pp. 33649-33655, 2016.

[97] S. Forrest, D. Bradley and M. Thompson, "Measuring the Efficiency of Organic Light-Emitting Devices", *Advanced Materials*, vol. 15, no. 13, pp. 1043-1048, 2003.

[98] Z. Tan, R. Moghaddam, M. Lai, P. Docampo, R. Higler, F. Deschler, M. Price, A. Sadhanala, L. Pazos, D. Credgington, F. Hanusch, T. Bein, H. Snaith and R. Friend, "Bright light-emitting diodes based on organometal halide perovskite", *Nature Nanotechnology*, vol. 9, no. 9, pp. 687-692, 2014.

[99] J. Pan, J. Chen, Q. Huang, L. Wang and W. Lei, "A highly efficient quantum dot light emitting diode via improving the carrier balance by modulating the hole transport", *RSC Advances*, vol. 7, no. 69, pp. 43366-43372, 2017.